The experimental realization of long-lived quantum memory

A Thesis
Presented to
The Academic Faculty

by

Ran Zhao

In Partial Fulfillment
of the Requirements for the Degree
Doctor of Philosophy

School of Physics
Georgia Institute of Technology
December 2010

The experimental realization of long-lived quantum memory

Approved by:

Professor Alex Kuzmich
School of Physics, Advisor

Professor Harold Kim
School of Physics

Professor T. A. Brian Kennedy
School of Physics

Professor Ken Brown
School of Chemistry and Biochemistry

Professor Phillip First
School of Physics

Date Approved: July, 15, 2010

To my parents

ACKNOWLEDGEMENTS

First, I would like to thank Prof. Alex Kuzmich for his encouragement, support, and advice during the five years of my Ph.D. career.

Next, I would like to thank Dr. Dzmitry Matsukevich and Dr. Thierry Chanelière for their instruction in AMO physics and experimental apparatus during my first year of graduate studies in the lab, and also for the continuous discussions about my research.

A special thank you goes to my colleague Yaroslav Dudin. We have endeavored together to extend the quantum memory lifetime. His efforts in the experiment were crucial to its success.

I would like to express my special appreciation to Dr. Stewart Jenkins, who is responsible for most of the theoretical analysis used in this thesis.

Also, I need to thank my colleague Corey Campbell. We joined the group the same year and spent so much time together learning in the lab the first two years. It would have been a difficult time without his help and inspiring ideas.

I would like to also thank all the past and present members of our research group: Alexander Radnaev, David Naylor, Anastasia Marchenkova, and Jacob Blumoff. It was a great time working with them.

I would like to thank our theoretical collaborators Prof. Brian Kennedy, Austin Collins, and Hsiang-Hua Jen for their insightful guidance and discussions.

Finally, I would like to thank my parents for their endless support and love.

TABLE OF CONTENTS

LIST OF TABLES

LIST OF FIGURES

SUMMARY

Quantum communication between two remote locations often involves remote parties sharing an entangled quantum state. At present, entanglement distribution is usually performed using photons transmitted through optical fibers. However, the absorption of light in the fiber limits the communication distances to less than 200 km, even for optimal photon telecom wavelengths. To increase this distance, the quantum repeater idea was proposed. In the quantum repeater architecture, one divides communication distance into segments of the order of the attenuation length of the photons and places quantum memory nodes at the intermediate locations. Since the photon loss between intermediate locations is low, it is possible then to establish entanglement between intermediate quantum memory nodes. Once entanglement between adjacent nodes is established, one can extend it over larger distances using entanglement swapping.

The long coherence time of a quantum memory is a crucial requirement for the quantum repeater protocol. It is obvious that the coherence time of a quantum memory should be much longer that the time it takes for light to travel between remote locations. For a communication distance l = 1000 km, the corresponding time is $t = l/c = 3.3$ ms. One can show that for a simple repeater protocol and realistic success probabilities of entanglement generation, the required coherence time should be on the order of many seconds, while for the more complicated protocols that involve multiplexing and several quantum memory cells per intermediate node, the required coherence time is on the order of milliseconds.

In this thesis, I describe a quantum memory based on an ensemble of rubidium

atoms confined in a one-dimensional optical lattice. The use of the magnetically-insensitive clock transition and suppression of atomic motion allows us to increase coherence time of the quantum memory by two-orders of magnitude compared to previous work. I also propose a method for determining the Zeeman content of atomic samples. In addition, I demonstrate the observation of quantum evolution under continuous measurement. The long quantum memory lifetime demonstrated in this work opens the way for scalable processing of quantum information and long distance quantum communication.

CHAPTER I

INTRODUCTION

In the last 15 years, quantum information science has become one of the most active fields of research for physicists, computer scientists, and engineers. Of course, the power of quantum mechanics to solve problems that seem intractable for classical methods was realized much earlier. In 1959 Richard Feyman [1, 2] invisioned new opportunities offered by quantum mechanics in physical system simulations and device engineering. However, for the next 10 or 20 years, this vision remained just an interesting academic exercise. It was another 10 or 20 years until realistic examples of such applications were proposed.

In 1994, Peter Shor came up with an algorithm that allows factoring of large numbers in polynomial time using a quantum system; in comparison, this is exponentially faster than the best known classical algorithm. Since many data encryption schemes presently (for example RSA algorithm [3, 4] widely used to encrypt the data transmitted over the internet by almost all web sites) rely on the fact that factorization of the large numbers is practically impossible for modern computers, quantum computers has attracted a great deal of attention over the past 15 years.

1.1 Quantum communication

If implemented, quantum computers will make modern classically encrypted communication insecure. Fortunately, quantum mechanics offers a solution to this problem. In 1984, Charles Bennett and Gilles Brassard proposed a communication protocol that relies on transmission of quantum states between remote parties [5]. The idea of quantum communication relies on the fact that due to the "no-cloning theorem" in

quantum mechanics [6], any measurement of a quantum state changes it. This change can be detected and any attempt to intercept the message by an adversary can be revealed.

Another approach to quantum communication, first proposed by Artur Ekert [7], relies on the sender and receiver sharing an entangled state. Quantum entanglement describes a phenomenon where the quantum states of two objects are always perfectly correlated with each other, even if they are spatially separated. Since the measurement of the quantum state will change the state and destroy these correlations, an entangled state shared by sender and receiver can be used as a resource for quantum communication. To explain the role of entanglement in quantum communication, we consider a simple case of quantum teleportation [8], where information needs to be transferred between two parties, Alice and Bob. Alice has been given a spin 1/2 particle in an arbitrary quantum state, $|\phi\rangle$, and she wants to send the state, $|\phi\rangle$, to Bob. It can be accomplished if Alice and Bob share a pair of qubits, A and B, in a maximally entangled state: $|\Psi_{\text{Bell}}\rangle_{A,B} = \frac{1}{\sqrt{2}}(|0\rangle_A|1\rangle_B - |1\rangle_A|0\rangle_B)$ and a classical communication channel.

To teleport her quantum state, Alice performs a joint-measurement of her original qubit and spin 1/2 particle, A, in a Bell basis:

$$|\Psi^{\pm}\rangle = \frac{1}{\sqrt{2}}(|0\rangle|1\rangle \pm |1\rangle|0\rangle)$$

$$|\Phi^{\pm}\rangle = \frac{1}{\sqrt{2}}(|0\rangle|0\rangle \pm |1\rangle|1\rangle)$$

The measurement result is sent to Bob through a classical channel. To reconstruct the qubit state, Bob is not required to actually learn the information about the qubit itself. He will be able to achieve the reconstruction by performing a single qubit rotation depending on the outcome of Alice's measurement.

Quantum teleportation was first implemented experimentally using entangled photons produced by parametric down conversion [9, 10, 11], where pairs of photons serve

as the information carriers. It has also been demonstrated with trapped ions using both phonons [12, 13] and photons [14] as carriers of quantum information.

1.2 Atomic ensembles

A quantum network requires both a carrier of quantum information and a media for the storage of quantum states. Since photons can propagate in free space or in an optical fiber, they are the natural choice for the transmission of quantum states. However, it is hard to store them for a long time. Atoms on the other hand, can be isolated from their environment and are an ideal choice for quantum memory. The interaction between a photon and single atom is usually weak. However, in atomic ensemble, the effective coupling strength of photons and many atoms is proportional to the square root of the number of atoms in the ensemble. Due to its strong coupling to light, atomic ensembles are promising candidates for quantum storage and matter-light qubit entanglement generation and distribution.

It is crucial that quantum states of light can be mapped into and out of atomic media. This mapping process can be realized by means of a technique known as electromagnetically induced transparency (EIT). EIT can make a resonant and opaque medium transparent by means of quantum interference. The medium is usually a collection of three level atoms. The application of a classical control field on one transition makes the medium transparent to the probe field on another transition. The envelope of a wave packet that propagates through an EIT medium can move with a group velocity much slower than the speed of light. The light field in the medium that supports EIT can be coherently mapped to an atomic spin wave, and retrieved later, preserving quantum properties of the initial field. Thus, it can be used to transfer quantum states of photon to atomic spin wave excitations.

The realization of coherent quantum state transfer from a matter qubit to a photonic qubit was achieved using cold rubidium at Georgia Tech in 2004 [15], followed

by the first light-matter qubit conversion and entanglement of remote atomic qubits in 2005 [16].

From there many advances involving atomic ensembles have been reported. The collapse and revival of dark state polaritons in EIT media under an applied magnetic field was observed [17]. Generation, storage, and retrieval of single light quanta transmitted between two remote atomic ensembles serving as quantum memory elements was demonstrated in 2005 [18]. A scheme to achieve long-distance quantum communication at the absorption minimum of optical fibers, employing atomic cascade transitions, was proposed and its critical elements experimentally verified [19]. A source of deterministic single photons was proposed and demonstrated by the application of a measurement-based feedback protocol to a heralded single-photon source consisting of an ensemble of cold rubidium atoms [20]. The entanglement between an atomic qubit based on a cold ^{85}Rb-^{87}Rb isotopic mixture and a frequency-encoded optical qubit was also demonstrated [21].

1.3 Quantum repeater with a multiplexed quantum memory

In the practical realization of quantum communication, the quantum state is usually carried by photons transmitted in optical fibers. In such a process, the decoherence of the photonic state due to the attenuation or noise in the optical fiber must be taken into account. Since the optical attenuation increases exponentially with distance, the number of trials needed to transport a photon from one site to another also increases exponentially. In this case, the communication rate and probability of success are limited by the distance. For example, the attenuation in an optical fiber at telecom wavelengths (1.3 - 1.5μm) is 0.2 to 0.3 dB/km and the photon loss at a distance of about 150 km is greater than 30 dB. This limits the maximum communication distance for the photon based quantum cryptography system.

The idea of a quantum repeater [22, 23] was proposed to overcome this difficulty. It is based on a solution somewhat similar to repeaters in classical communication. In the classical repeater one simply divides the distance between sender and receiver into several segments and amplifies the signals to restore it to its original shape at the intermediate points between segments. In quantum mechanics, however, it is impossible to "amplify" a quantum state due to the no-cloning theorem [6]. To distribute quantum information between two remote sites, A and B, with a separation which is much larger than the attenuation length of an optical fiber, one can still divide the transmitting channel into N segments and insert pairs of quantum memory nodes at the connecting points, $C_1, C_2, ...C_N$, between the segments.

The first step in the quantum repeater protocol is generating entanglement between adjacent quantum memory nodes. If the distance, L_0, between pairs of memories is comparable to the attenuation length of the photon in the fiber, the success probability of entanglement generation is relatively high and one can expect to establish entanglement after relatively few trials. After that, the entangled segments are connected by making joint-measurements on all intermediate pairs of quantum memory qubits except for $C_L, C_{2L}, ...C_{N-L}$ (a process known as entanglement swapping). Here, number of pairs L is limited by the entanglement fidelity. The quantum states of the intermediate qubits will be destroyed by the measurement and the entanglement will be established between the first and the last qubits. This process will leave us with a network of N/L entangled segments.

Losses and imperfections in transmission of quantum information will likely limit the entanglement fidelity of remote qubits. Moreover, if the remote qubits are not in the maximally entangled state, entanglement swapping will decrease the fidelity even further, so that after some number of steps, remote qubits are no longer entangled. To solve this problem, an entanglement purification protocol [24, 25, 26] can be implemented using M pairs of elements in every pair of quantum where every qubit

pair in remote nodes is connected in parallel. Here, M depends on the initial fidelity. The entanglement purification protocol starts with M pairs of partially entangled states and produces an almost maximally entangled pair of qubits using only local operations inside each remote node. To finally establish entanglements between two terminal sites, one needs to iterate the joint-measurements on intermediate qubits in the network and the entanglement purification steps until the target entanglement is established.

One can show [22] that the required number of elementary pairs for a quantum repeater protocol is:

$$R = N^{\log_L M+1} \tag{1}$$

The equation above shows that the number of involved elementary nodes in a quantum repeater architecture and the communication rate scales polynomially with distance [22].

Fig. 1(a) shows a 3-level quantum repeater. In this case, $N = 8, L = 2$. First, entanglement generation proceeds with probability P_0, creating 8 entanglement lengths of L_0. In the lowest panel, shaded memory sites indicate successfully entangled segments. The first level entanglement connection proceeds with probability P_1, producing four entangled segments of length $2L_0$. Nodes reset to their vacuum states by the connection are blank. The second and third levels proceed with probabilities P_2 and P_3. Each stage results in entanglement-length doubling, until the terminal nodes are entangled.

However, quantum communication success rates in the quantum repeater architecture are limited by finite quantum memory lifetime [27]. With a given short memory lifetime, one could improve the success rate of an entanglement connection by implementing a more flexible configuration of connections between pairs of elements. In particular, instead of a parallel scheme (Fig. 1(b)), one can use a multiplexed scheme, shown on Fig. 1(c). In the parallel scheme, quantum memory elements in

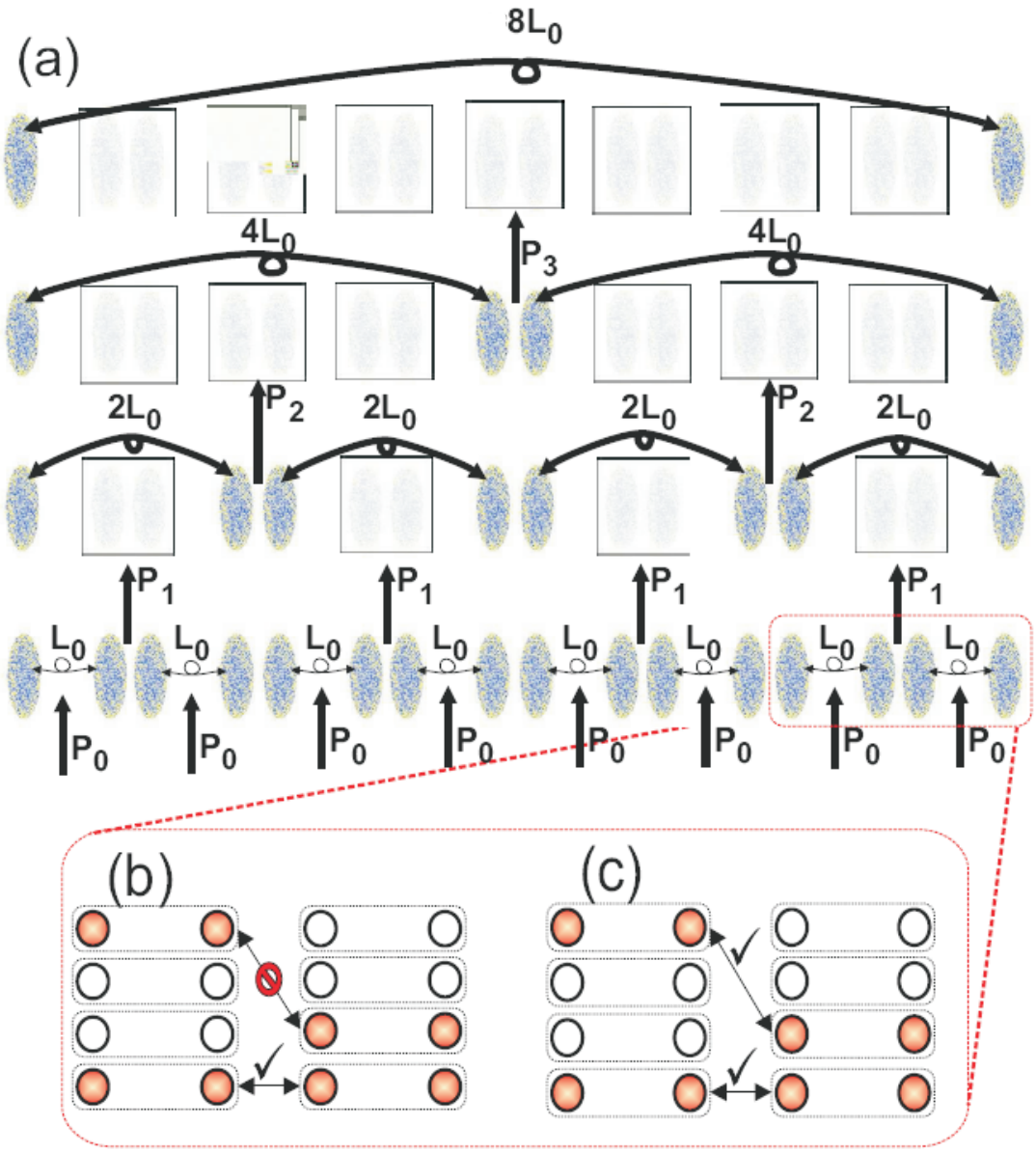

Figure 1: (a) Processes of a 3-level multiplexed quantum repeater. In addition to two terminal nodes, the network has seven internal nodes consisting of two quantum memory sites containing n independent memory elements. P_0 is the entanglement generation probability, and P_1, P_2, and P_3 are the entanglement connection probabilities in Level 1, 2, and 3 respectively. (b) and (c) show the topology of the n memory element sets. The parallel architecture shown in (b) connects entanglement only between memory elements with the same address. In contrast, multiplexing, shown in (c), uses a fast sequential scanning of all memory element addresses to connect any available memory elements.

one node can interact with only one element in the neighbouring nodes. In this case, the entanglement connection success rate scales linearly with the number of elements in each node. In the multiplexed scheme, one can dynamically configure the connections between nodes using the information about existing entanglement successes to determine which nodes should be connected. The multiplexed scheme has a clear advantage compared to the parallel scheme, especially when the memory life is short [27].

With the proposal of a modified quantum repeater based on dynamic allocation of quantum resources, the multiplexed quantum memory was demonstrated experimentally in 2009 [28]. A dozen independent quantum memory elements within a single cold sample was demonstrated, as well as the matter-light entanglement generation involving arbitrary pairs of these elements.

The combination of a quantum repeater architecture and multiplexed quantum memory offers a way towards long distance quantum communication. Nevertheless, it is crucial to increase the quantum memory lifetime to realize a quantum repeater.

Millisecond storage of coherent light has been reported in atomic gases [29, 30, 31], and coherence times in excess of 1 s have been achieved in a solid state [32]. However, these experiments did not demonstrate the light storage in the quantum regime, required for quantum repeater operation. The longest previously reported coherence time [20] for single photon storage in a cold rubidium ensemble (32 μs) was insufficient to carry out the quantum repeater protocol over distances where direct transmission fails. In this thesis I focus mainly on our efforts to achieve long-lived quantum memory coherence time using atomic ensembles confined in far-detuned optical lattices, with magnetically insensitive coherences as the basis of the memory.

1.4 DLCZ protocol

The DLCZ protocol [33] is one of the most prevailing schemes for entanglement generation. It was proposed by Duan, Lukin, Cirac and Zoller in 2001. The scheme employs atomic ensembles and single photon detection. In the DLCZ protocol, quantum states can be transferred between atoms and photons and stored in atoms for long periods of time.

The DLCZ protocol is based on atomic ensembles with a lambda-type level configuration. The protocol is started by preparing all atoms in the ground state. A weak write pulse illuminates the atomic sample and induces, with probability $\ll 1$, a Raman transition. The Raman scattered photon is collected in a certain mode, as the *signal* field. Detection of the *signal* photon results in preparing a single spin excitation in the ensemble. Later a relatively strong *read* pulse is used to convert the stored atomic excitation into an *idler* field.

Due to collective enhancement, the second photon will be emitted in the direction determined by the phase matching condition $\mathbf{k_i} = \mathbf{k_w} - \mathbf{k_s} + \mathbf{k_r}$. The process can create a two-photon entangled state which can be subsequently used for quantum communication.

1.5 Outline

The remainder of this thesis is organized as follows: In Chapter II, I first give an overview of the theory of dipole trap loading and describe the experimental setup and procedures for loading a far-detuned optical dipole trap. A calculation of the trap oscillation frequencies for our trap geometries is then shown. At the end of the chapter, I illustrate the imaging system for monitoring the loading efficiency of the dipole trap and show a measurement of the dipole trap lifetime and atomic temperature utilizing the imaging system.

In Chapter III, I describe a quantum memory based on the magnetically-insensitive

clock transition in atomic rubidium confined in a one dimensional optical lattice. Quantum memory lifetimes exceeding 6 milliseconds are observed. The importance of utilizing clock coherences is demonstrated by measurements of the coherence time in an unpolarized sample trapped in both a magneto-optical trap and a far-detuned optical trap. Also, the effect of atomic motion on the coherence time is demonstrated by the measurement of the coherence time in a single focused beam dipole trap. The decoherence mechanisms for the stored spin wave excitations are discussed. Finally, I present the measurements of the quantum statistics for the stored spin-wave excitations, and describe our realization of a high-quality deterministic single-photon source.

Long-lived quantum memories require precise control of atomic Zeeman populations of optically dense atomic samples. Chapter IV proposes a method to determine atomic Zeeman state population distributions of atomic spin-wave excitations. The method is implemented in a cold atomic gas confined in a one-dimensional optical lattice.

In Chapter V I present our the observations of the conditional dynamics of a quantum system under continuous measurement in a correlated atomic ensemble-signal field system undergoing a continuous photoelectric measurement of the signal field.

CHAPTER II

OPTICAL DIPOLE TRAP LOADING

There are three fundamental traps in neutral atom trapping – radiation pressure traps, magnetic traps and optical dipole traps. Radiation pressure traps use near resonance light and have typical trap depths of a few Kelvin. Magnetic traps use a state-dependent force on the magnetic dipole moment of an atom in an inhomogeneous magnetic field and have typical trap depths on the order of 100 mK. Optical dipole traps rely on the electric dipole interaction between atoms and a far-off-resonance light field; they have typical trap depths below one millikelvin. The light-induced collisions in a far-off-resonance dipole trap are infrequent and atoms can be preserved in the trap for seconds or even minutes under certain conditions. This allows to carry out a variety of investigations that require long-lived atomic coherences.

In 1986, Chu et al.[34] realized the first optical trap for neutral atoms. After this demonstration, enormous experimental efforts have been directed to study behaviors of atoms in far-off-resonance optical dipole traps in different regimes. Much colder and denser atomic samples became available for the efficient loading of shallow dipole traps. Also, many different geometries of dipole traps have been realized and studied.

2.1 Dipole trap loading theory

Consider an atom placed in a laser light field. The electric field **E** induces an atomic dipole moment **p** that oscillates at the laser light driving frequency ω. **E** and **p** can be expressed as

$$\mathbf{E}(\mathbf{r},t) = \hat{e}\tilde{E}(\mathbf{r})exp(-i\omega t) + c.c., \tag{2}$$

$$\mathbf{p}(\mathbf{r},t) = \hat{e}\tilde{p}(\mathbf{r})exp(-i\omega t) + c.c., \tag{3}$$

where $\hat{e}$ is the unit polarization vector. The relation between $\tilde{E}$ and $\tilde{p}$ is simply

$$\tilde{p} = \alpha \tilde{E}. \tag{4}$$

Here, α is the *complex polarizability*, which depends on the frequency of the external laser field. The average interaction potential of the dipole moment in the electric field is given by

$$U_{dip} = -\frac{1}{2}\langle \mathbf{pE} \rangle = -\frac{1}{2\epsilon_0 c} Re(\alpha) I. \tag{5}$$

The potential energy of the atom in the field is proportional to the laser intensity and to the real part of the polarizability. In the simplest case of a two level atom, the atomic polarizability is given by

$$\alpha = 6\pi\epsilon_0 c^3 \frac{\Gamma/\omega_0^2}{\omega_0^2 - \omega^2 - i(\omega^3/\omega_0^2)\Gamma}, \tag{6}$$

where ω_0 is the resonance frequency and Γ is the damping rate(corresponding to the spontaneous decay of the excited level). The latter is determined by the dipole matrix element between ground and excited state,

$$\Gamma = \frac{\omega_0^3}{3\pi\epsilon_0 \hbar c^3} |\langle e|\mu|g\rangle|^2. \tag{7}$$

In most experiments, the trapping laser frequency, ω, and atomic resonance frequency, ω_0, fulfill the condition $|\Delta| \ll \omega_0$, where the detuning $\Delta \equiv \omega - \omega_0$. This allows one to simplify the calculations for the dipole potential and scattering rate using the rotating-wave approximation. One obtains the following expressions:

$$U_{dip}(\mathbf{r}) = \frac{3\pi c^2}{2\omega_0^3} \frac{\Gamma}{\Delta} I(\mathbf{r}), \tag{8}$$

$$\Gamma_{sc}(\mathbf{r}) = \frac{3\pi c^2}{2\hbar\omega_0^3} (\frac{\Gamma}{\Delta})^2 I(\mathbf{r}). \tag{9}$$

The scattering rate Γ_{sc} and the dipole potential depth U_{dip} are related via:

$$\hbar\Gamma_{sc} = \frac{\Gamma}{\Delta} U_{dip}. \tag{10}$$

Since the dipole potential scales as I/Δ, the scattering rate scales as I/Δ^2. Therefore, optical dipole traps usually use large detunings and high intensities to keep the scattering rate for a given depth of the trapping potential.

Depending upon the trapping light detuning, we can distinguish between two different kinds of dipole traps – the blue-detuned and the red-detuned. A blue-detuned trap uses trapping light with frequency above atomic resonance ($\Delta > 0$) and the dipole interaction repels atoms out of the light field. In this case, the dipole potential minima correspond to the minima of the light intensity. A red detuned trap uses trapping light with frequency below atomic resonance ($\Delta < 0$) and the dipole interaction attracts atoms into the light field. In this case, the dipole potential minima correspond to the maxima of the light intensity. In the rest of this chapter I describe a red-detuned optical dipole trap.

2.2 Calculation of differential Stark shift in an optical dipole trap

The effect of far-detuned laser light on the atomic levels can be treated as a second order perturbation in the electric field, i.e. linear in terms of the field intensity. This result shows a simple relation between the optically induced shift (known as light shift or ac Stark shift) of the ground state and the potential energy of the two level atom confined in the optical dipole trap. Fig. 2 illustrates the light shift of a two-level atom. The energy shift of the excited state and ground state can be expressed as:

$$\Delta E = \pm \frac{|\langle e|\mu|g\rangle|^2}{\Delta}|E|^2 = \pm \frac{3\pi c^2}{2\omega_0^3}\frac{\Gamma}{\Delta}I \tag{11}$$

It has a simple relation to the trap potential; $U_{dip}(\Delta) = |\Delta E|$.

Most experiments in laser cooling and trapping are performed with alkali atoms because they have cycling transitions that lie in a convenient spectral range. Due to interactions between atomic electrons and the nucleus, the ground levels of alkali

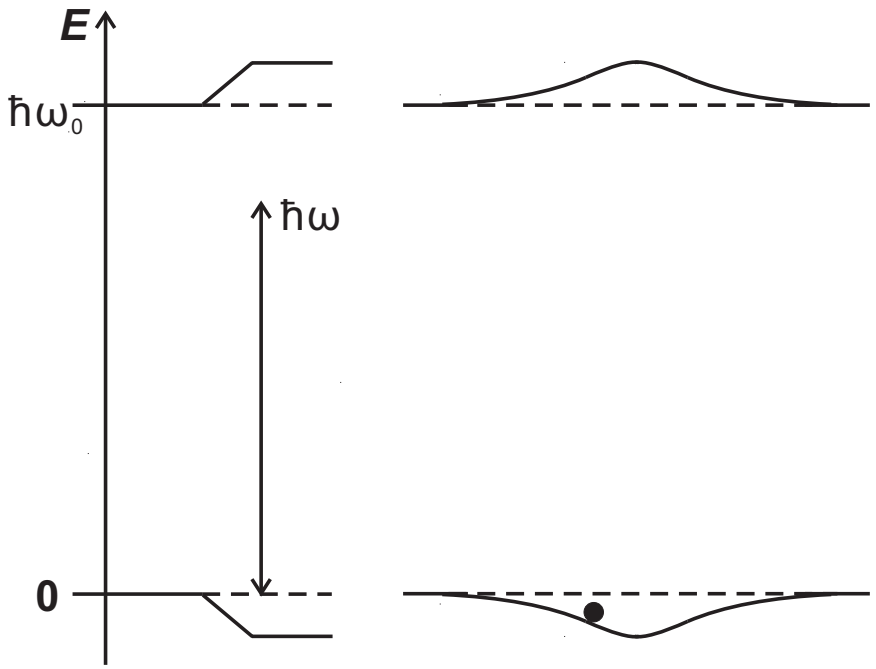

Figure 2: Stark shift for a two-level atom. Left side: red-detuned light shifts atomic ground state level down and excited state level up by same amounts. Right side: an atom trapped in a ground-state potential well produced by a Gaussian laser beam.

atoms have hyperfine structure, so that the energies of the ground $S_{1/2}$ levels corresponding to different values of total angular moment, $F = j \pm 1/2$, are separated by a few Ghz. Here, j is the total spin of the nucleus.

The detuning of the trapping laser light from the atomic transition in the upper ground level is smaller than for an atom in the lower ground level. As a result, the atom in the upper ground state experiences a slightly stronger light shift. This differential light shift, δ_0, can be approximated as,

$$\hbar\delta_0 = U_0(\Delta_{eff}) - U_0(\Delta_{eff} + \omega_{hfs}) \tag{12}$$

where Δ_{eff} is the effective detuning, taking into account weighted contributions of different atomic transitions, and ω_{hfs} is the ground state hyperfine splitting. Since $\omega_{hfs} \ll \Delta_{eff}$, the differential light shift can be approximated as

$$\hbar\delta_0 = \eta\, U_0, \tag{13}$$

which is proportional to the trap potential, and $\eta = \omega_{hfs}/\Delta_{eff}$.

2.3 1-D red-detuned optical dipole trap

To extend the lifetime of a quantum memory based on an atomic ensemble, we have built a one dimensional red-detuned optical lattice for Rb atoms. We use a 20 W single frequency linearly polarized Ytterbium fiber laser and an amplifier from IPG-photonics for our trapping light. The trapping light has a wavelength of 1064 nm and therefore is red-detuned from the resonance frequencies of D1 and D2 transitions of ^{87}Rb atoms, which are 780 nm and 795 nm, respectively. Fig. 3 shows the optical dipole trap setup. The output mode of the high power trapping laser has a diameter of 1.45 mm. Two optical isolators from Isowave are aligned right after the output of the high power fiber laser to prevent damage from back reflection of laser light. There is typically 30% loss of optical power through the two isolators.

A mechanical shutter from Uniblitz is used for switching the trapping light on and off. After the laser light passes through the open shutter, a polarizer splits the light field into two parts with orthorgonal linear polarizations, horizontal and vertical. The horizontal field then passes through a half-waveplate to rotate its polarization to match that of the other light field. Two trapping laser beams with the same phase and same polarization are then focused into the same spot in an evacuated glass cell where Rb atoms are collected and loaded in a Magneto-Optical trap (MOT). The atoms are loaded at the intersection of the two trapping beams.

The far-off-resonance optical dipole trap (FORT) loading procedure is illustrated by Fig. 4 and Fig. 5. First, atoms are loaded into a magneto-optical trap (MOT) and then the MOT parameters are adjusted to optimize sub-Doppler cooling. The magnetic fields for the MOT are switched off a few milliseconds before the MOT trapping and repumping fields are switched off. A delay time of tens of milliseconds allows untrapped atoms to fall away and leave only atoms trapped in the FORT for

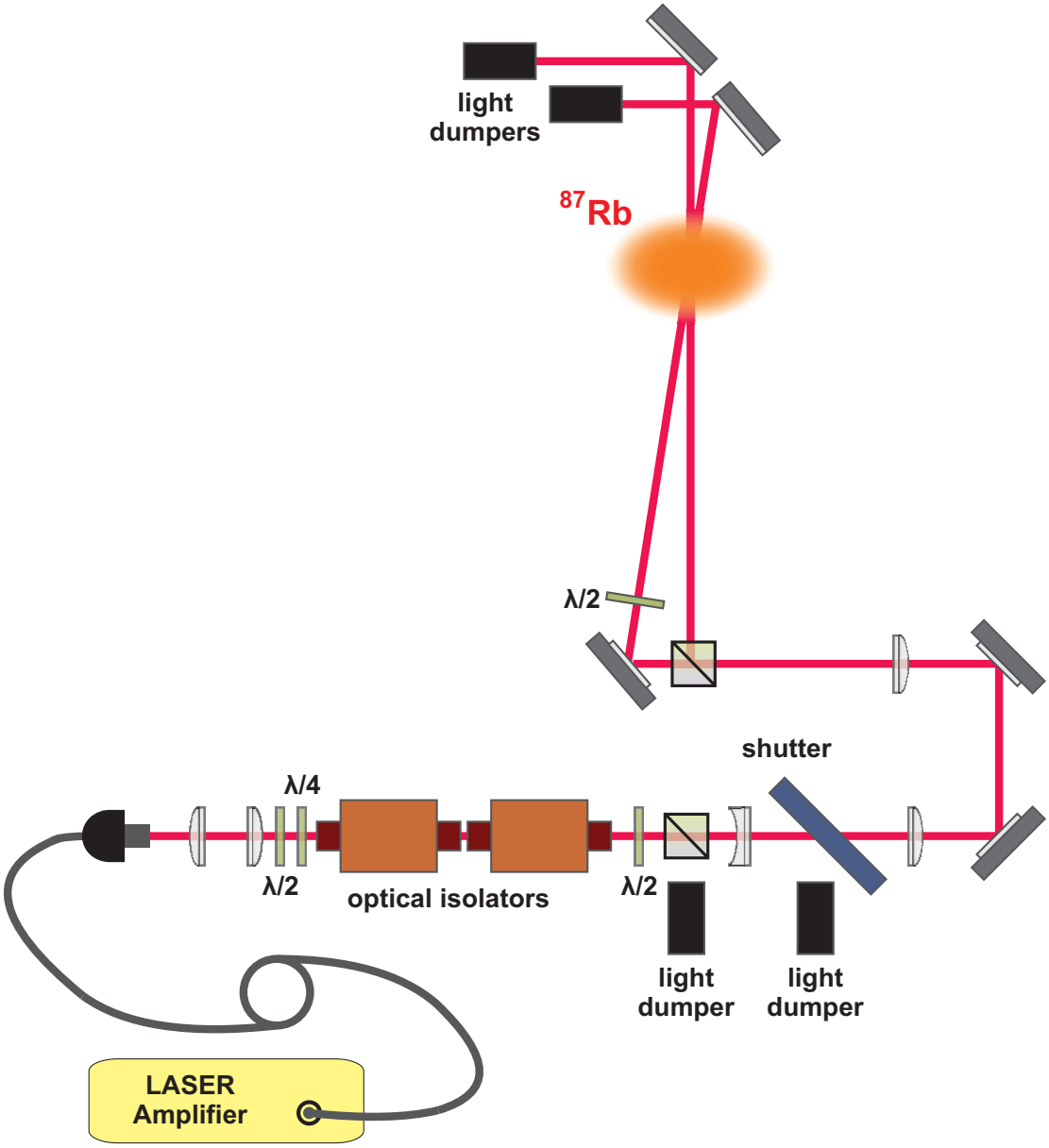

Figure 3: Essential elements of the optical dipole trap set-up.

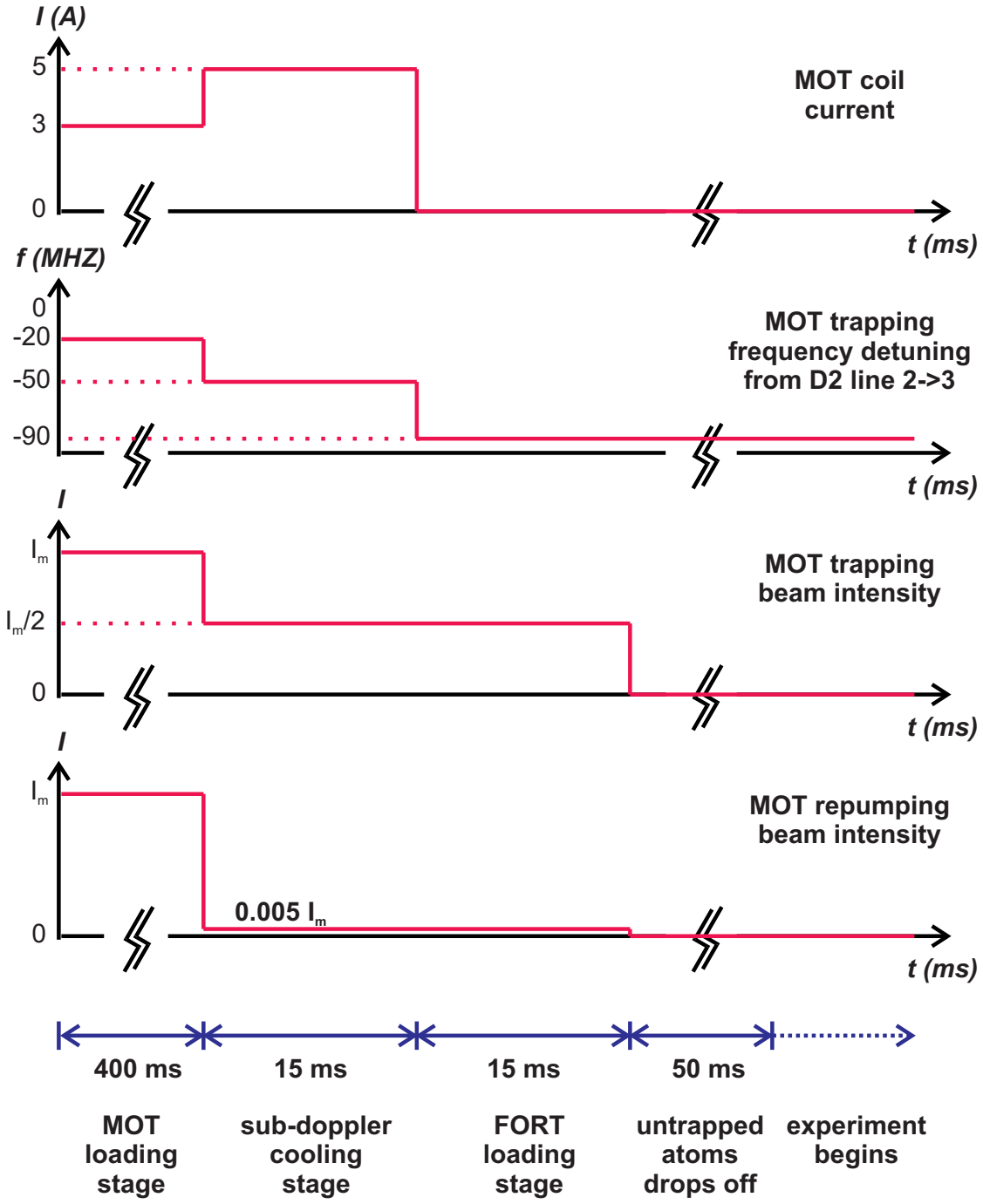

Figure 4: Dipole trap loading sequence (part 1).

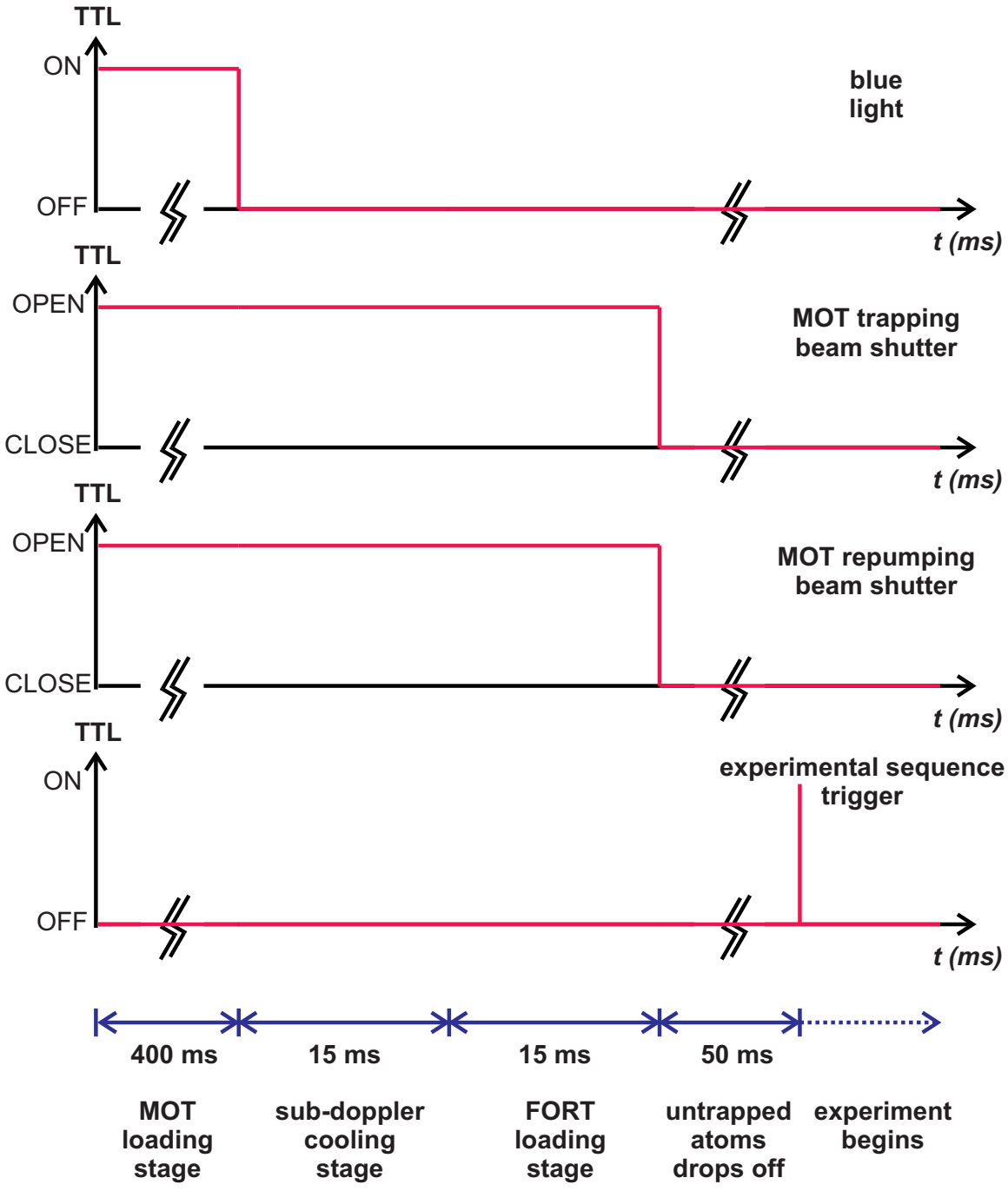

Figure 5: Dipole trap loading sequence (part 2).

experimental use. To increase the atomic pressure in the vacuum chamber, a blue LED light is swtiched on during the MOT loading stage to desorb rubidium atoms from the walls of the glass cell.

The MOT trapping light frequency detuning is controlled by two double-pass acousto-optic modulators (AOMs). Voltage-controlled oscillators (VCOs) change the RF frequencies driving the AOMs. The repumping light intensity is controlled by one single-pass AOM with RF power modulated by a voltage variable attenuator (VVA).

A PCI-6713 analog output board from National Instruments is used for fast control of all VCOs, VVAs, and switches during the FORT loading procedure. The PCI board has 8 analog channels with $\pm$10V output range, as well as 8 digital lines with 5V TTL signals. The maximum update rate of 0.74 million samples per second combined with the built-in counter allows us to precisely control the loading sequence with an update rate resolution of 10 μs. The upper and lower parts of the front panel of the LabVIEW program used to control the PCI-6713 board for FORT loading are shown in Fig. 6 and Fig. 7, respectively.

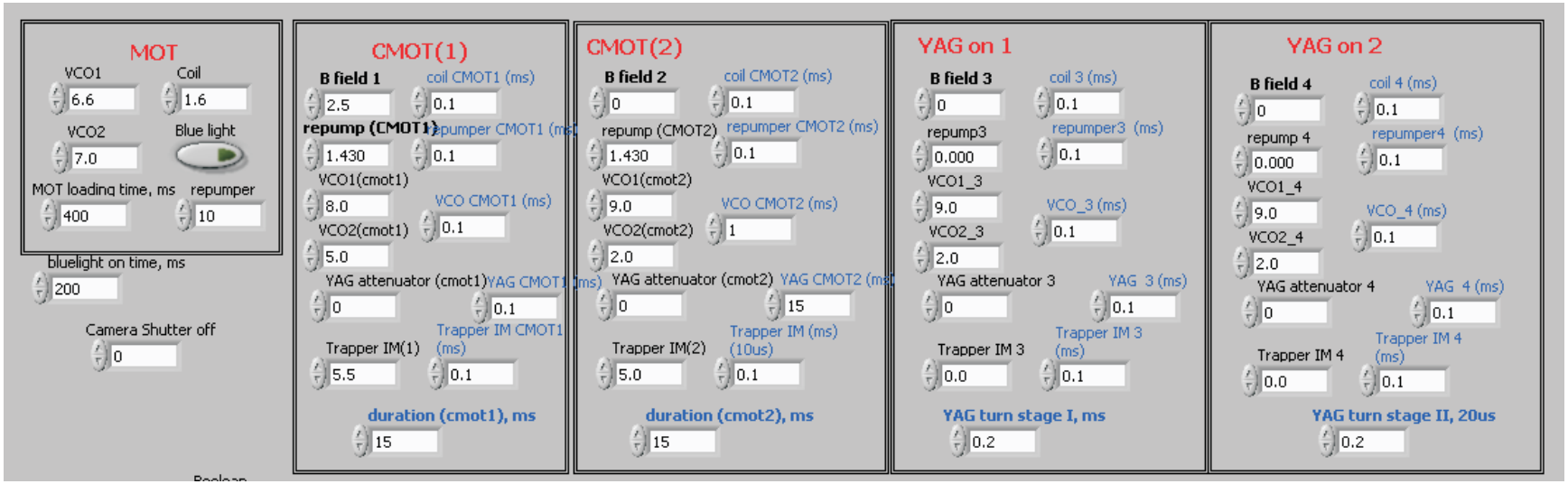

Figure 6: Upper part of the LabVIEW program controlling FORT loading sequence. It controls the FORT loading efficiency. All times are in milliseconds. After the MOT loading stage, each stage begins with the previous setting and ends with the setting shown on itself (black labels). The transition speed is decided by the setting in blue labels.

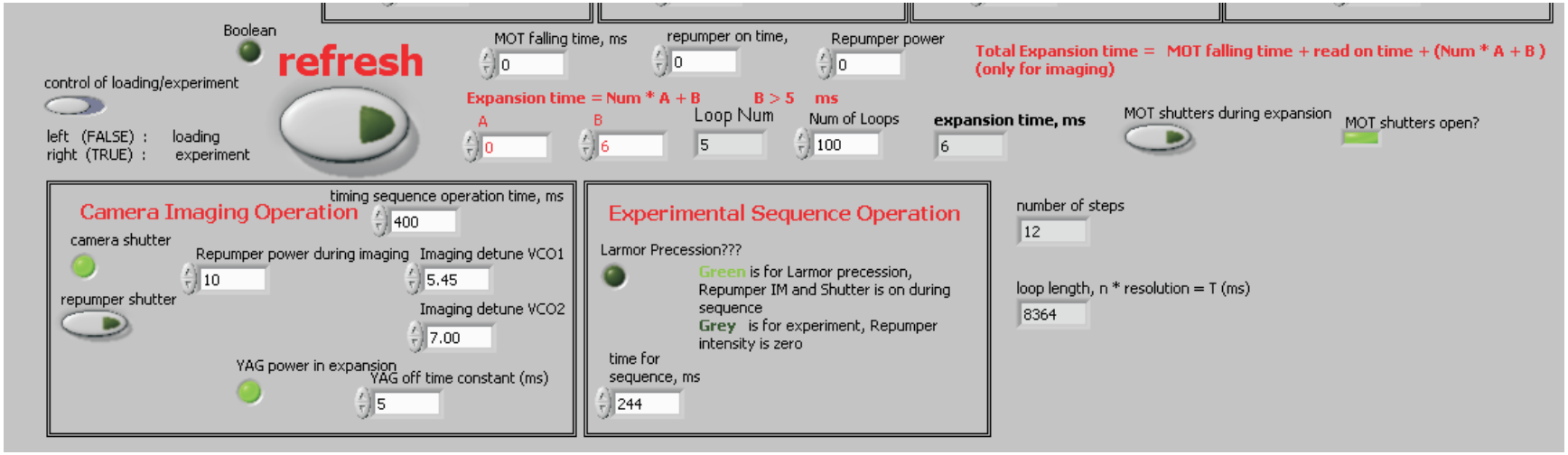

Figure 7: Lower part of the LabVIEW program controlling FORT loading sequence. It descibes the setting for relevant parameters after the FORT is loaded. The top left button decides whether the sequence is for monitoring loading efficiency by imaging from the camera or for experimental use.

2.4 Trap frequency calculation

For a single focus optical dipole trap with a Gaussian trapping beam propogating along the z-axis, the maximum oscillation frequencies are (Ref.[35]):

$$\omega_x = \omega_y = \frac{2}{w_{f0}}(\frac{|U_m|}{m})^{1/2},$$

$$\omega_z = \frac{\sqrt{2}}{L_f}(\frac{|U_m|}{m})^{1/2},$$

where w_{f0} is the trapping beam waist, U_m is the maximum trap depth, m is the atomic mass, $L_f = \pi w_{f0}^2/\lambda_f$ is the Rayleigh length, and λ_f is the trapping field wavelength.

Fig. 8 shows the trapping potential for a 1-D optical lattice with two trapping beams with the same waist w_{f0}, intersecting at a small angle θ. The lattice period is $d_f = \lambda_f/(2sin(\theta/2))$. Clearly in this case, the maximum trap oscillation frequencies are different from those given by the expressions above.

When the the waist of the trap along the z-axis $w_z = w_{f0}/sin(\theta/2)$ is smaller than the Rayleigh length of the trapping beam, the maximum oscillation frequency along the z-axis is determined by the waist instead of the Rayleigh range,

$$\omega_z = \frac{2}{w_z}(\frac{|U_m|}{m})^{1/2}.$$

The maximum oscillation frequency along the y-axis is determined by the waist of the trap along the y-axis: $w_y = w_{f0}$.

$$\omega_y = \frac{2}{w_y}(\frac{|U_m|}{m})^{1/2}.$$

To calculate the maximum oscillation frequency along the x axis, we assume that atoms perform simple harmonic oscillations in the trap. We can write an equation of atomic motion as follows:

$$m\ddot{x} = -\omega_x^2 x.$$

Here

$$\omega_x^2 = \frac{1}{m}\frac{d^2U}{dx^2}$$

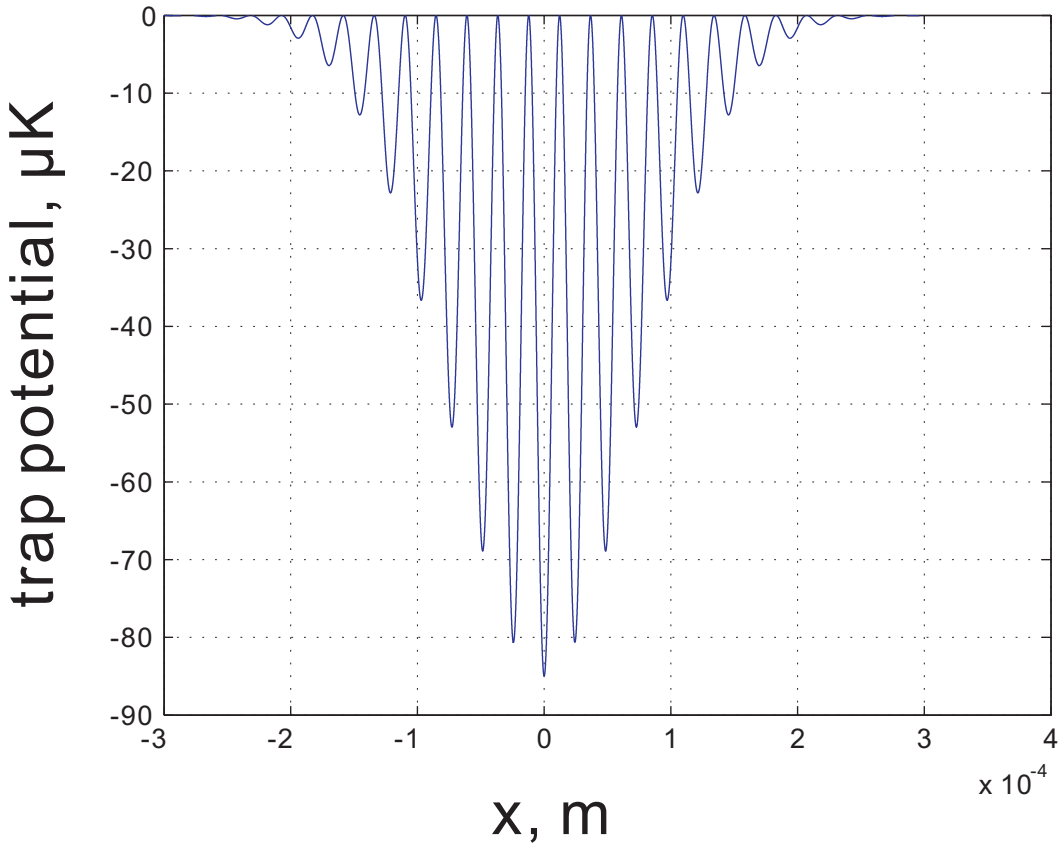

Figure 8: Trapping potential of a 1-D optical lattice. Two trapping beams with wavelength 1064 nm intersect at an angle $\theta = 2.5$ degrees. Each beam has a waist of 150 μm and power of 7.5 W.

and

$$U = \frac{U_m}{2} + \frac{U_m}{2} sin \frac{2\pi x}{d_f}.$$

Therefore,

$$\omega_x = \frac{\sqrt{2}}{d_f} (\frac{|U_m|}{m})^{1/2}.$$

The results of calculations for our experimental parameters are given in Chapter 3 and Chapter 4.

2.5 Imaging system of the far-off-resonance optical dipole trap

We use a front illuminated EMCCD camera DV887 from Andor Technology to image atoms in the optical dipole trap. The pixel readout rate is set at 5 MHz. The quantum efficiency of this camera at 795nm is about $Q_e = 44\%$. The pixel size is 16×16 μm. The active pixel range on the CCD is 512×512, giving an array size of 8.2×8.2 mm. $n_e = 13.5$ electrons corresponds to one A/D count.

The camera is mounted on a 3-axis translation stage to finely adjust position, and, due to the limited optical access, the whole system is mounted at an angle of $\theta_{cam} = 30$ degree to the horizontal. A mechanical shutter is attached to the camera to prevent camera CCD exposure to intense light scattering during the MOT loading stage.

The procedure for taking images of atoms in the FORT is described below: atoms are first loaded into the optical dipole trap from the MOT. After a delay of 30 to 50 ms to let untrapped atoms fall away, the imaging process starts. The camera shutter opens 5 ms before imaging. The imaging process is described below (See Fig. 9 and Fig. 10 for details): the camera exposure time is set to 5 ms and the camera electronic gain is set to unity. In the middle of the 5 ms exposure time, the MOT trapping beams and repumping beam are switched on for imaging for duration T_{img} = 1 ms. The MOT trapping light detuning δ is set to 20 MHz below resonance. To

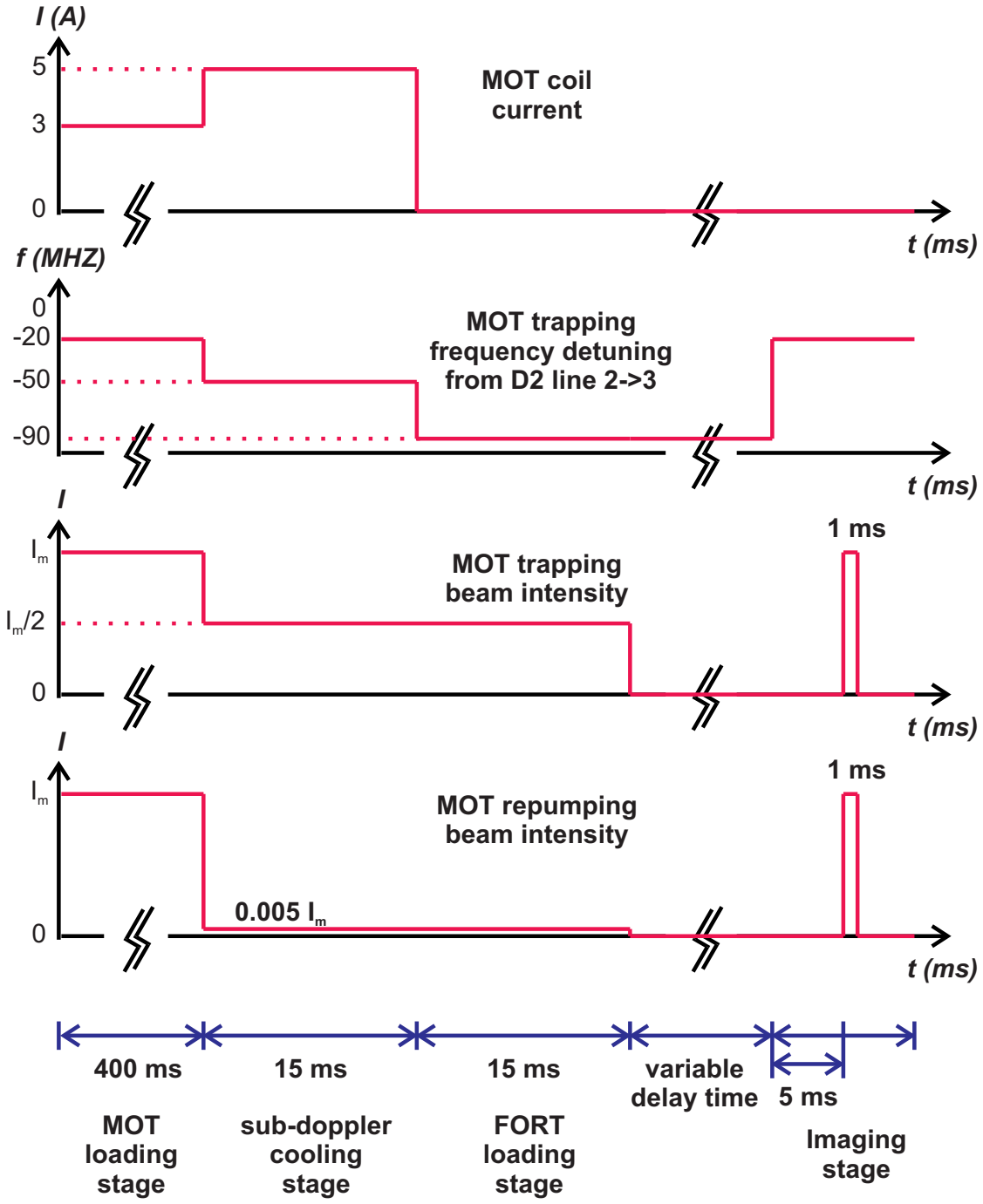

Figure 9: Dipole trap imaging sequence (part 1).

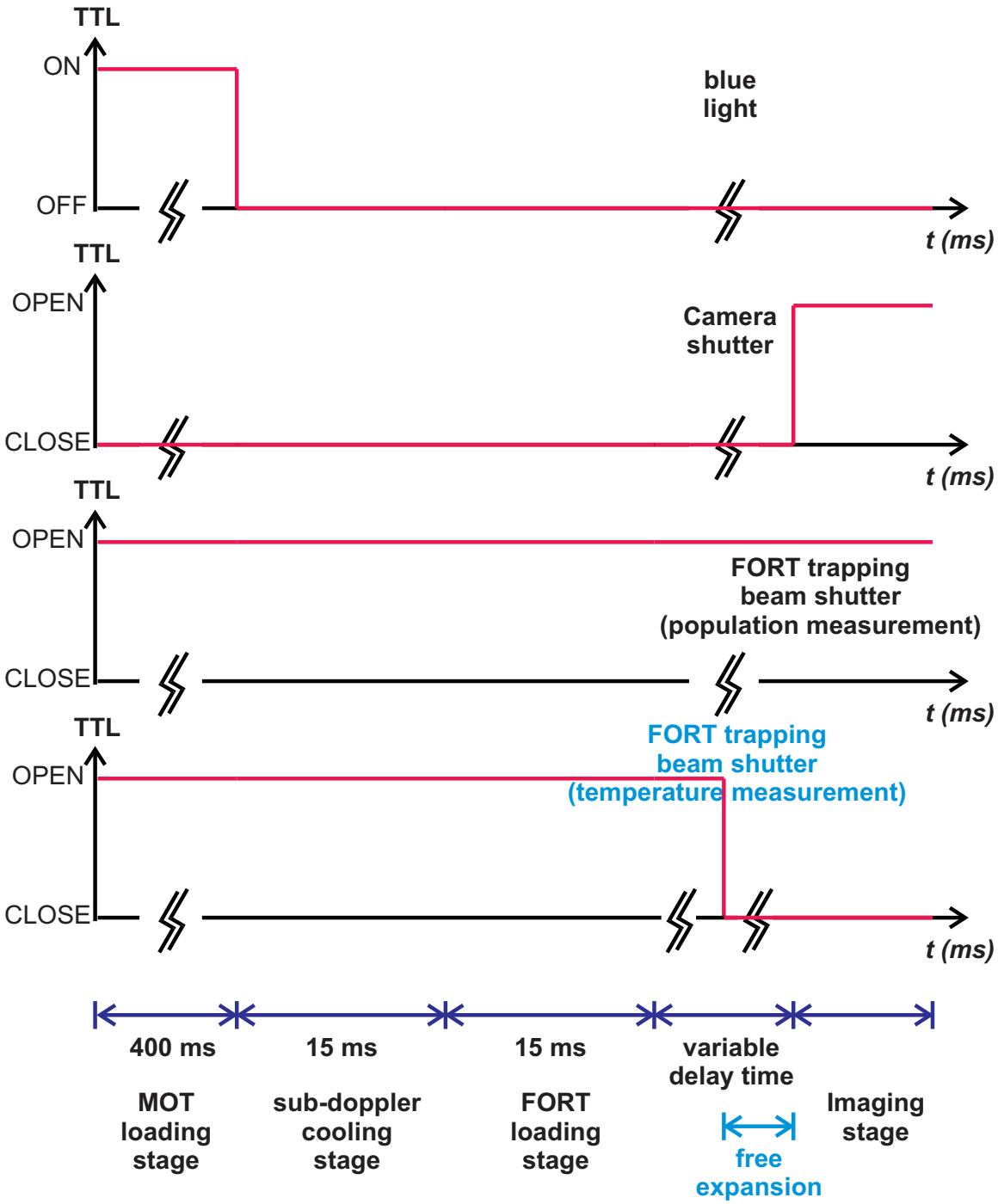

Figure 10: Dipole trap imaging sequence (part 2).

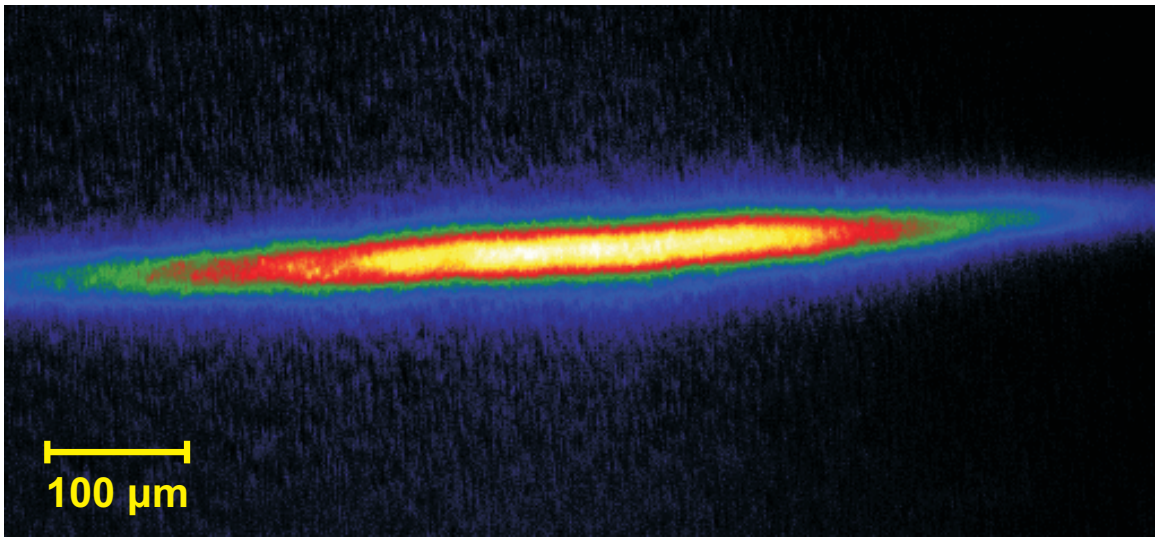

Figure 11: Image of atoms in an optical dipole trap, picture taken in Jan. 2009. $\sim 10^7$ atoms are loaded in the FORT.

exclude the influence of the background, we take two images, with and without FORT trapping light, and subtract one from the other. Fig. 11 shows one of the images from the FORT, for trap depth of 150 μK.

To calibrate the imaging system and determine the number of atoms per count, $\eta_{a/c}$, on the EMCCD camera, we first consider the interaction between the laser field and atoms. This can be described with the Optical Bloch Equations and density matrix including spontaneous emission. For a simple two-level atom with ground state $|e\rangle$ and excited state $|g\rangle$, the Rabi oscillation frequency is defined as

$$\Omega \equiv \frac{-eE_0}{\hbar}\langle e|r|g\rangle.$$

The on-resonance saturation parameter is

$$s_0 \equiv 2|\Omega|^2/\gamma^2 = I/I_s,$$

where

$$I_s \equiv \frac{\pi hc}{3\lambda^3\tau}.$$

Here, I is the laser intensity at the atom position, and I_s corresponds to the saturation

intensity of a particular transition with wavelength λ and lifetime $\tau = 1/\gamma$, here γ is the excited state natural linewidth.

The rate of absorption and emission of photons by an atom can be described as the scattering rate γ_p,

$$\gamma_p = \frac{s_0\gamma/2}{1 + s_0 + (2\delta/\gamma)^2} \tag{14}$$

where δ is the light frequency detuning from resonance.

Now we assume that the camera is monitoring an ensemble of N atoms. The sample is illuminated by a light field with intensity I and detuning δ for an imaging acquisition time T_{img}. The scattering rate from the atomic sample is $\gamma_p(I, \delta)$. During the acquisition time, the ratio of number of scattered photons impinging upon the CCD sensor of the camera to number of atoms is given by

$$\frac{N_p}{N} = T_{img}\gamma_p(I, \delta)\frac{\Omega_{solid}}{4\pi}$$

where Ω_{solid} is the solid angle of the atomic fluorescence from the trap collected through the imaging system and directed onto the CCD sensor.

With N_c counts detected by the camera, the coefficient of counts per photon $\eta_{c/p} \equiv N_c/N_p$ is

$$\eta_{c/p} = \frac{Q_e}{n_e}$$

where Q_e is the quantum efficiency of the camera at the wavelength of the light field and n_e is the number of electrons corresponding to one A/D count. We therefore have

$$\eta_{a/c} \equiv \frac{N}{N_c} = \frac{4\pi n_e}{Q_e T_{img}\gamma_p(I, \delta)\Omega_{solid}}$$

2.6 Trap lifetime measurement

Fig. 12 shows decay of lattice fluorescence as a function of time. The $1/e$ lifetime of the dipole trap is $\tau = 1.6$ s. The decay of the number N of atoms in a trap can be

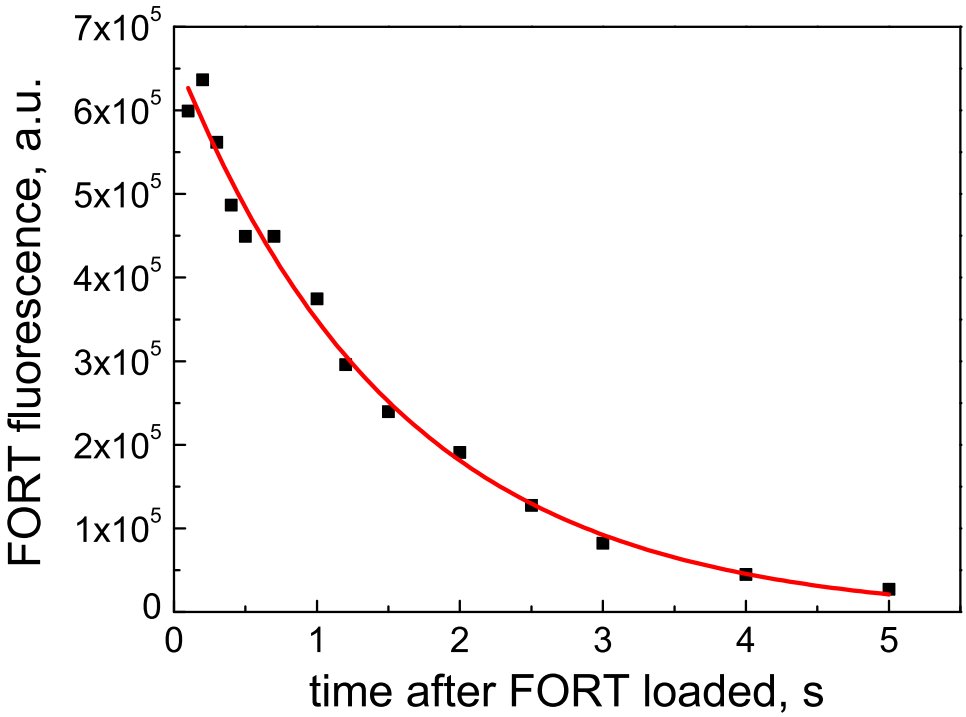

Figure 12: FORT fluorescence signal of the 1-D optical lattice as a function of time. The solid line shows the fit of the data to an exponential decay. The 1/e trap lifetime $\tau = 1.6$ s.

described by the general loss equation [36]

$$\dot{N}(t) = -\alpha N(t) - \beta \int_V n^2(\mathbf{r}, t) d^3r - \gamma \int_V n^3(\mathbf{r}, t) d^3r,$$

where α, β and γ are the single-particle loss, two-body loss and three-body loss coefficients, respectively. Single-particle loss is due to the collisions with background gas in the vaccum apparatus. Two-body loss comes from ultracold binary collisions or light assisted collisions involving atoms in the excited state. Three-body losses are relevant for high density atomic samples. All of the three mechanisms contribute to the observed value of the dipole trap lifetime.

2.7 Temperature measurement of an optically confined sample

We use the time-of-flight method [37] to measure the temperature of the atoms in the FORT. In this method, the atoms confined in the FORT are released and the velocity, v, of the atoms during the free expansion of atomic sample is determined. The temperature, T, of the atomic cloud is determined by

$$T = \frac{M}{k_B} v^2 \tag{15}$$

The measurement procedure is described as follows: first the atoms are loaded into the optical dipole trap from the MOT, then the FORT trapping light is switched off, allowing the atoms to freely expand in vaccum. At a certain delay time t, a background subtracted image is taken by the EMCCD camera. The number of counts, $N(x, y)$, on every pixel of the CCD sensor is recorded, where x and y are the horizontal and vertical directions, respectively. We integrate the counts in the horizontal direction and get $N_{sum}(y, t) = \Sigma N(x, y)$.

The corresponding waist, $\sigma(t)$, and center of the sample along the vertical direction, $C(t)$, are extracted from the image by fitting $N_{sum}(y, t)$ with a Gaussian function

$$N_{sum}(y, t) = A exp(-\frac{(y - C(t))^2}{\sigma(t)^2}),$$

where A, $C(t)$, and $\sigma(t)$ are the adjustable parameters.

A set of waists and sample centers are measured at a set of different delay times. Fig. 13 shows selected reconstructed images in color contour format from one of the sets of measured data points. Atomic velocity, v, is calculated by fitting $\sigma(t)$ as a function of delay time t

$$\sigma(t) = \sqrt{\sigma_0^2 + (vt)^2},$$

where σ_0 is the initial waist of the trap. We treat σ_0 and v as the adjustable parameters. With the extracted velocity, we can calculated the atomic temperature with

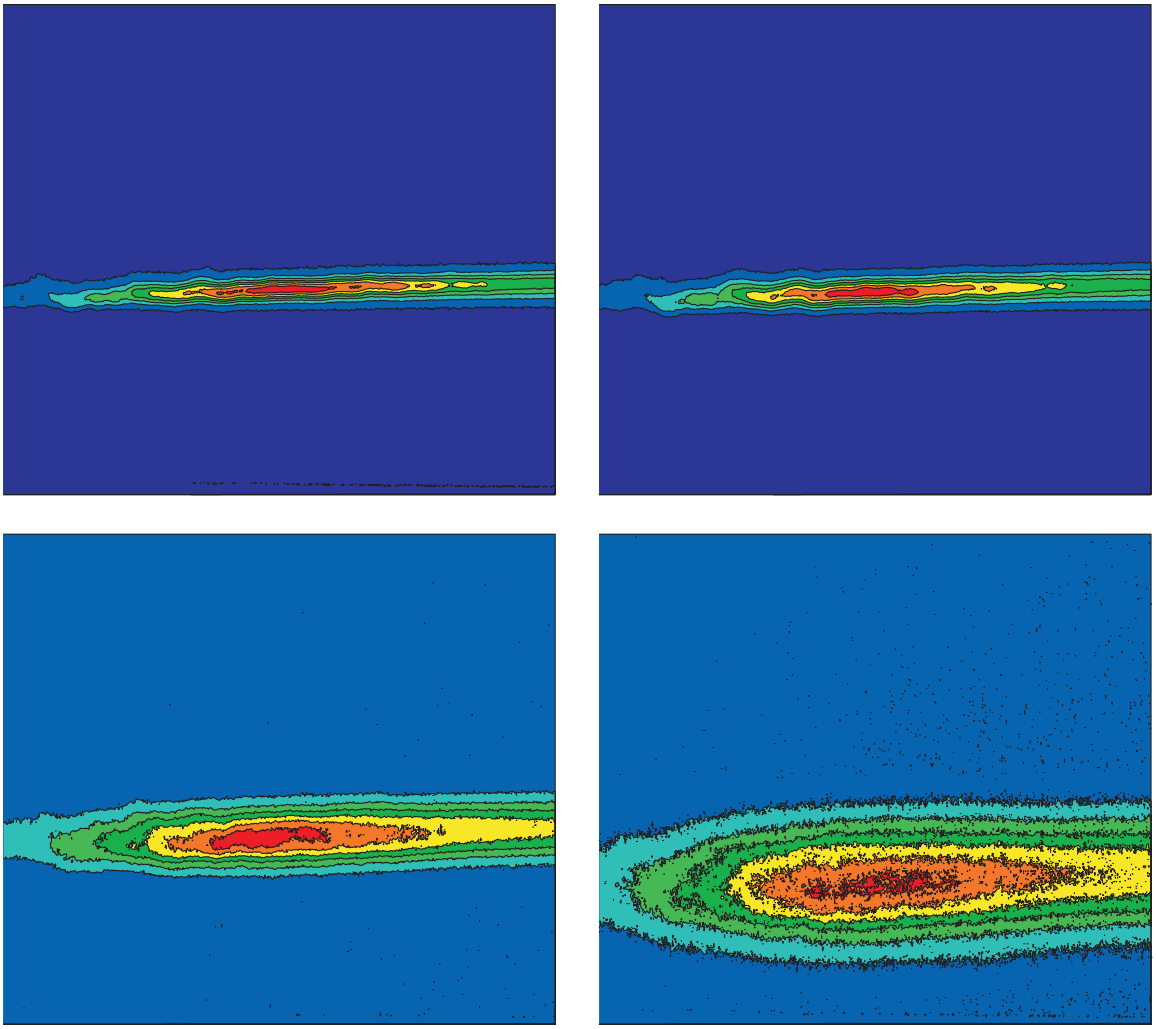

Figure 13: Images of dipole trap at different delay times, t, after atoms are released from the trap confinement. $t = 4$ ms (top left), 8 ms (top right), 12 ms (bottom left), 16 ms (bottom right). Data taken at trap depth U = 80 μK.

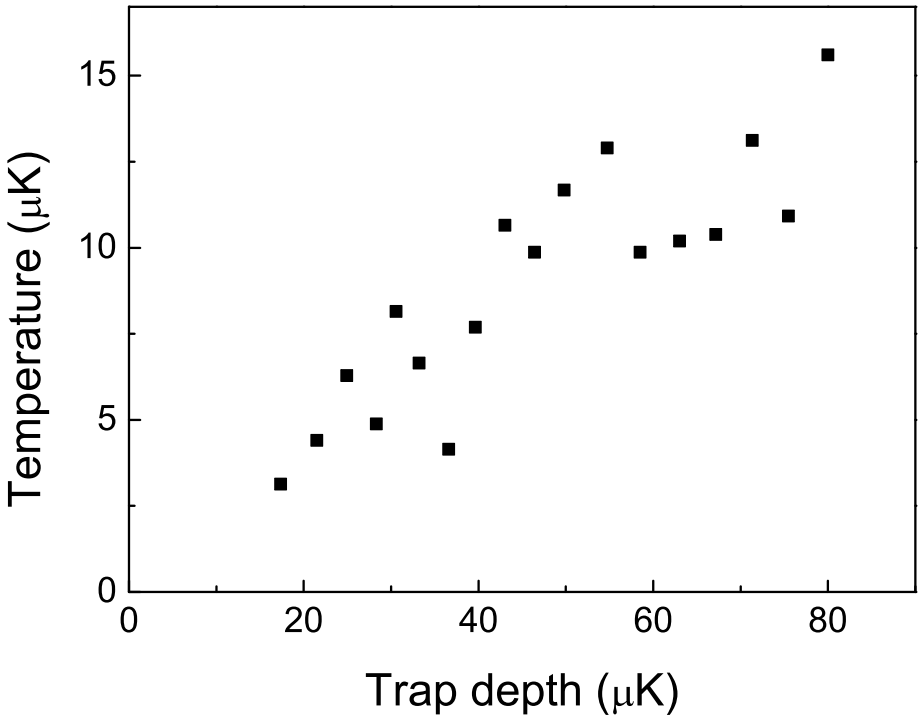

Figure 14: Measured temperature of atoms in the FORT as a function of trap depth.

Eq. 15.

Fig. 14 shows the the temperature of atoms in the FORT measured as a function of dipole trap depth. From the measurements, we determine that the temperature of the atomic sample is about 15% to 20% of the trap depth. The validity of the atomic temperature measurement can be verified by comparing the gravitational constant g and the extracted acceleration g' from the measured atomic sample center position $C(t)$ along the vertical direction. For images taken by a camera mounted at an angle, θ_{cam}, to the horizontal plane, we can extract g' by fitting $C(t)$ with

$$C(t) = C_0 + \frac{1}{2} cos(\theta_{cam}) g' t^2.$$

where C_0 is the initial center position of the FORT. We treat g' and C_0 as adjustable fit parameters.

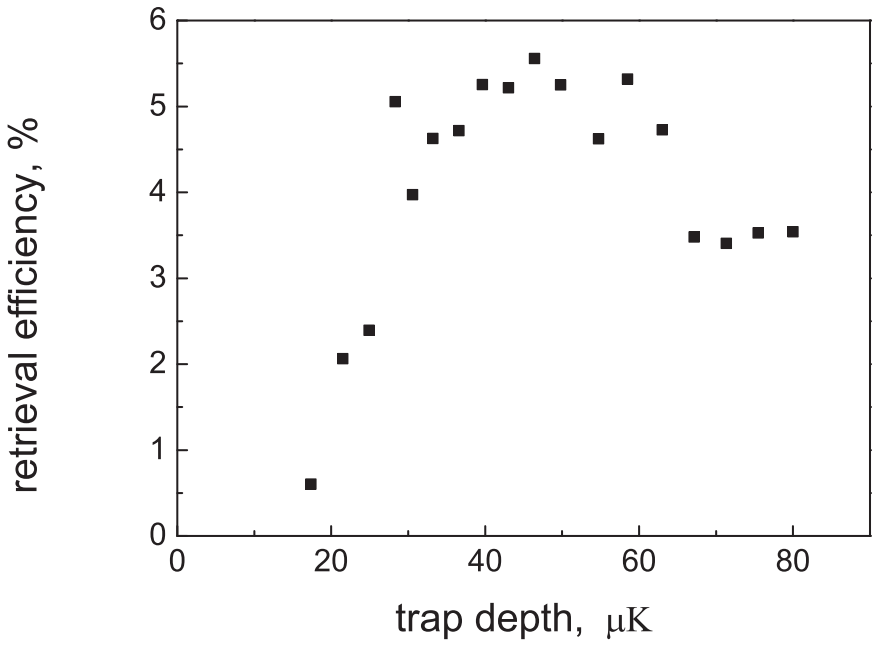

Figure 15: Retrieval efficiency as a function of trap depth.

As a reference, in Fig. 15, I also show the measured retrieval efficiencies (see Chapter 3 for details) as a function of dipole trap depth.

CHAPTER III

LONG-LIVED QUANTUM MEMORY

This chapter is based on Ref. [38].

3.1 Introduction

Protocols for quantum communication are typically based on remote parties sharing and storing an entangled quantum state. The generation of such remote entanglement must necessarily be done locally and distributed by light transmission over optical fiber links or through free space [11]. For the distribution of entanglement over a length L the characteristic timescale for storage is the light travel time L/c, where c is the speed of light in the medium. For $L = 1000$ km, $L/c \approx 5$ ms for an optical fiber.

In practice, direct entanglement distribution over optical fibers is limited by absorption to distances $l \sim 100$ km. In order to distribute entanglement over longer distances, the channel should be divided into links of length $\leq l$. The division circumvents attenuation in the fiber provided the intermediate memory nodes, which terminate the links, have a non-zero quantum memory time. Entanglement distributed over these shorter links is then connected over length L according to a family of protocols generically known as the quantum repeater. The entanglement distribution rate of a network depends critically on the memory time of these storage elements. For $L \sim 1000$ km, required memory times vary from many seconds for simple network topology [22, 33] to milliseconds for more complex (e.g., multiplexed) topologies and architectures [27, 39, 40]. Such long-lived quantum memories could revolutionize deterministic single photon sources [20] and lead to the generation of entangled states

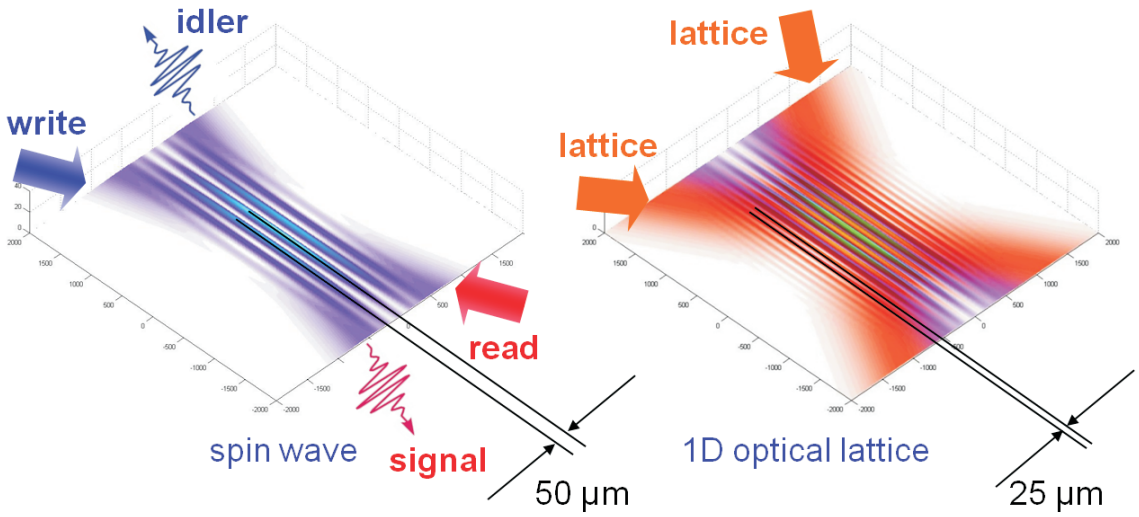

Figure 16: Spatial profiles of atomic spin wave grating (left panel) and optical lattice field intensity (right panel). The write and signal fields (wavelength 795 nm) intersect at a 0.9° angle. The lattice is formed by two 1.06 μm beams intersecting at a 2.5° angle.

over extended systems [41].

Enhancing the matter coupling to a single spatial light mode is an advantage shared by cold optically thick atomic ensembles [15] and single atoms in high-finesse cavities [42]. The longest quantum memory time previously reported, 32 μs in a cold rubidium ensemble [20], is insufficient to carry out quantum repeater protocols over the distances where direct transmission fails. The rubidium sample, prepared in state of zero average magnetization, was allowed to freely fall during the protocol and the quantum memory time was limited by the effects of small uncompensated magnetic fields. In short, equally populated atomic states of opposite magnetization, $\pm m\mu_B$, where m is the angular momentum projection and μ_B is the Bohr magneton, respond asymmetrically to ambient fields [18, 43, 44, 17, 45, 46, 47, 48]. Ballistic expansion of the freely falling gas provides a longer memory time limitation which can be estimated from the time $\tau = \Lambda/(2\pi v) \sim 100$ μs it takes an atomic spin grating to dephase by atomic motion (we use some representative parameters typical of the MOT

environment: grating wavelength $\Lambda = 50$ μm, atomic velocity $v = \sqrt{k_B T/M} \simeq 8$ cm/s for $T = 70$ μK). Millisecond storage of classical, coherent light has been reported in atomic gases [29, 30, 31], while coherence times in excess of 1 s have been achieved in the solid state [32].

In order to extend memory times into the millisecond range, both the magnetic decoherence and the effects of atomic motions are to be eliminated. We achieve this by confining Rubidium-87 atoms in an optical lattice of 25 μm period (See Fig. 16) employing the $m = 0 \leftrightarrow 0$ ground-state atomic hyperfine transition for storage. We thereby take advantage of the magnetic insensitivity of the so-called clock transition, whose energy depends only quadratically on external magnetic fields. The ground hyperfine levels a and b of ^{87}Rb have angular momenta $F_a = 1$ and $F_b = 2$, and the upper and lower clock states are written as $|+\rangle \equiv |b, m = 0\rangle$ and $|-\rangle \equiv |a, m = 0\rangle$, respectively. If the atoms are prepared in the upper clock state by optical pumping, the $|+\rangle$ and $|-\rangle$ states can be coupled by Raman scattering of a weak linearly polarized *write* laser field into an orthogonally polarized signal field detected in the near-forward direction.

3.2 Write/Read protocol

Collective spin-wave excitations are created via the write/read protocol [33]. The *write* field is 20 MHz below resonance of the $b \leftrightarrow c$ transition. The *read* field is on resonance with the $a \leftrightarrow c$ transition. Here $\{|a, b\rangle\}$ corresponds to $\{5S_{1/2}, F = 2, 1\}$ and $\{|c\rangle\}$ represents $\{5P_{1/2}, F = 2\}$ of the ^{87}Rb atoms.

The detection of the signal photon implies a momentum change $\hbar(\mathbf{k_w} - \mathbf{k_s})$ of the atoms, where $\mathbf{k_w}$ and $\mathbf{k_s}$ are the *write* and signal field wavevectors, respectively. The excitation amplitude for an atom at position $\mathbf{r}_\mu$ is proportional to $e^{-i(\mathbf{k_w}-\mathbf{k_s})\cdot\mathbf{r}_\mu}$. The collective atomic excitation, imprinted with this phase grating, is the *write* spin wave. The spin wave coherence is essential in providing efficient coupling to a single spatial

electromagnetic field mode in the retrieval stage, or *read* process, performed after a controllable storage period. Optical confinement preserves the spin wave coherence by suppressing atomic motion along the $\mathbf{k_w} - \mathbf{k_s}$ direction.

The physics of the *read* process can be described using the concept of the clock polariton [49], a bosonic light-matter excitation with creation operator

$$\hat{\Psi}_0^\dagger(z,t) = \frac{\Omega\hat{\varphi}^\dagger(z,t) + i\kappa\sqrt{n}\hat{s}^\dagger(z,t)}{\sqrt{|\Omega|^2 + n|\kappa|^2}}. \tag{16}$$

This is a linear combination of the *read* spin wave associated with the clock transition and the idler field propagating along the quantization axis z, and linearly polarized in the x-direction; these are described by creation operators $\hat{s}^\dagger$ and $\hat{\varphi}^\dagger$, respectively. The form of the polariton operator shows that adiabatic variation of the y-polarized *read* field Rabi frequency Ω causes reversible conversion between the propagating idler field and the *read* spin wave. The collective Rabi frequency associated with the idler transition $c \rightarrow b$ is given by $\kappa\sqrt{n}$, where κ is the dipole coupling strength and n the atomic number density.

Our goal is to convert the *write* spin wave, heralded by signal photodetection, into the idler field, with high efficiency. It is therefore essential to have a large overlap between the *write* and *read* spin waves. In order to maximize this overlap, the signal and idler spatial mode functions should be matched and the condition $\mathbf{k_i} = \mathbf{k_w} - \mathbf{k_s} + \mathbf{k_r}$ satisfied [50], where $\mathbf{k_i}$ and $\mathbf{k_r}$ are wavevectors for the idler and *read* fields, respectively. The overlap is also influenced by the atomic state preparation, angular momentum quantum numbers and transition strengths of the atomic levels a, b and c. For $F_a = 1, F_b = F_c = 2$ with atoms prepared in the $|+\rangle$ (upper clock) state, the *write* and *read* spin wave operators are equal, implying maximum efficiency.

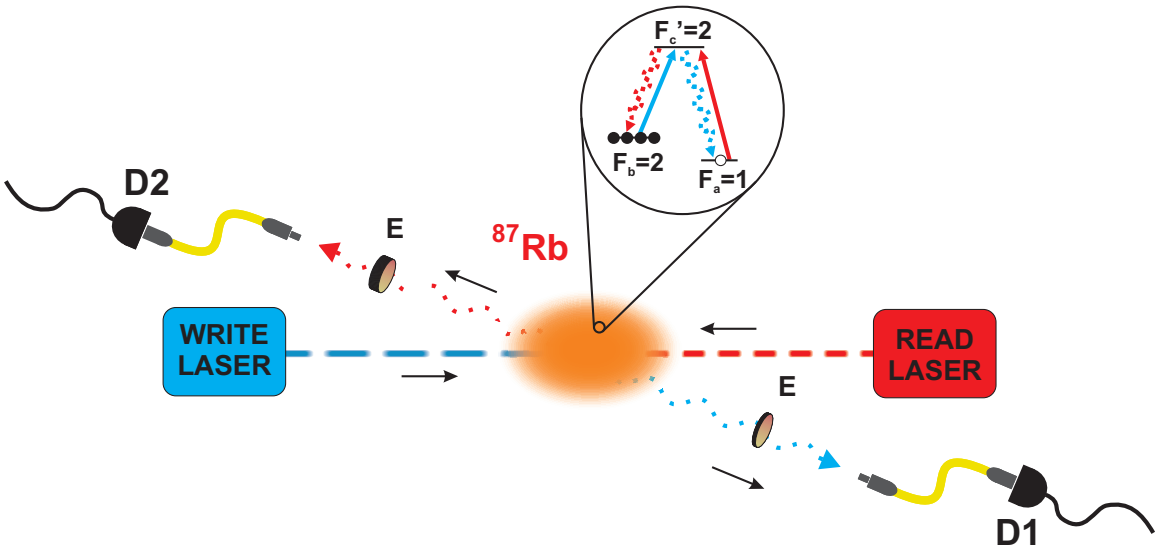

Figure 17: Essential elements of the experimental set-up for measuring coherence time of unpolarized atoms in a magneto-optical trap. The inset shows the atomic level scheme. Here, E is a Fabry-Perot interferometer (etalon) and D1 and D2 are single photon detectors.

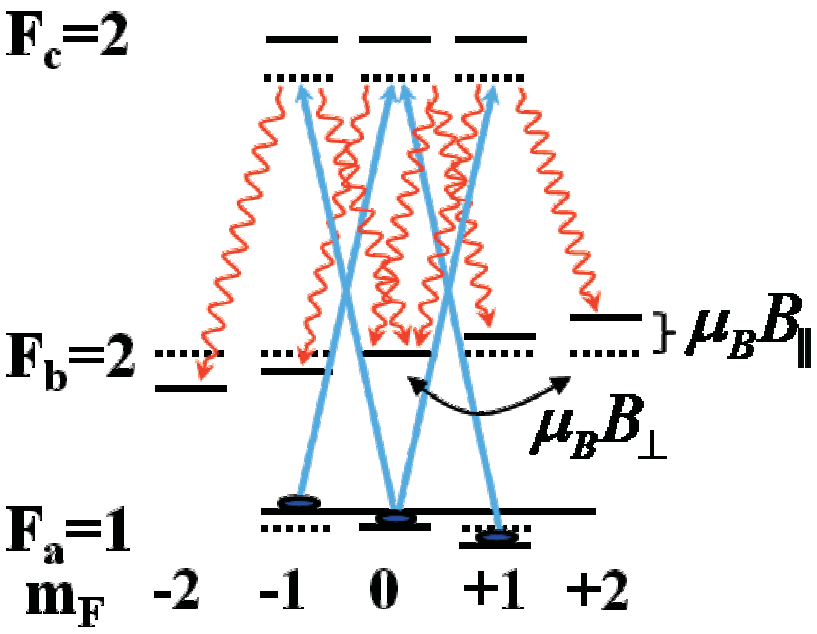

Figure 18: Energy diagram of ^{87}Rb atoms in a magnetic field. Hyperfine levels in the magnetic field split into 2F+1 Zeeman sublevels. This splitting causes time evolution of hyperfine coherences established by the write process and time variation of the retrival efficiency.

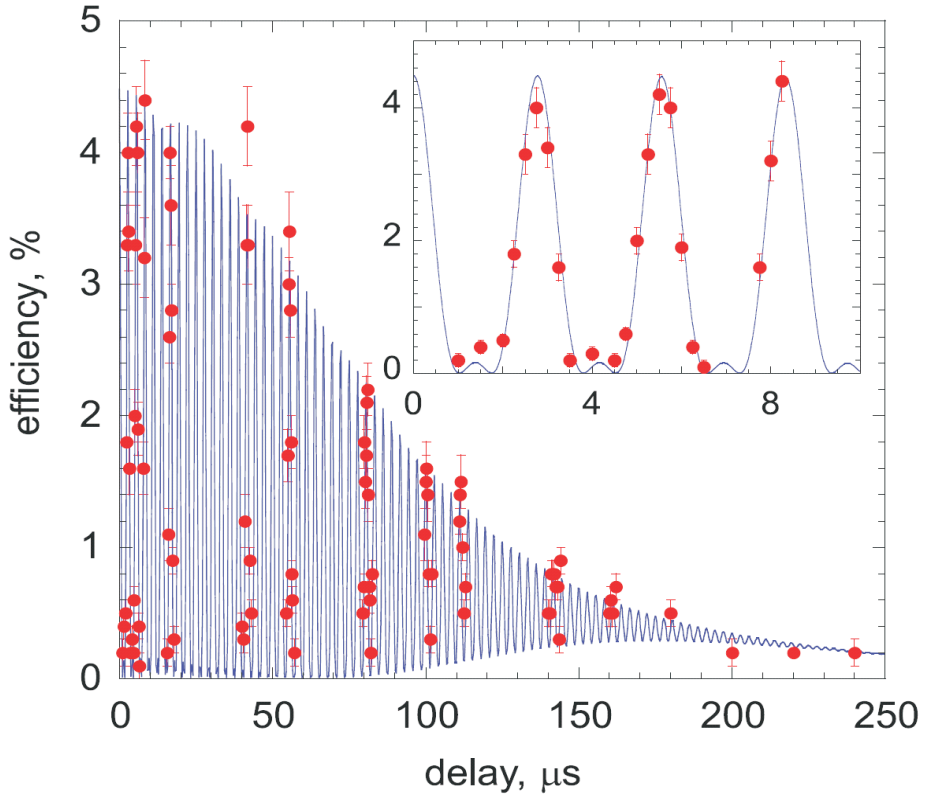

Figure 19: Retrieval efficiency as a function of storage time for unpolarized atoms in a magneto-optical trap. Experimental data, circles, show rapid damped oscillations due to Larmor precession at short times, followed by slow decay associated with the clock transition dephasing. The inset shows details of the short-time damped oscillations. The solid curves are fits based on theory. $B_0 \approx 0.25$ G.

3.3 Unpolarized, freely diffusing atomic gas

We first performed quantum memory lifetime measurements in an unpolarized, freely diffusing atomic gas in a bias magnetic field. A schematic of our experiment is shown in Fig. 17. A cold atomic cloud of ^{87}Rb is provided by a MOT. The atoms are collected in the MOT for 40 ms, after which the experimental sequence begins with an unpolarized sample of atoms prepared in level $|b\rangle$. During the 2 ms experimental sequence, a bias magnetic field of $B_0 \approx 0.25$ G is applied along the signal field.

The sequence begins with a 50 ns long vertically polarized incident write pulse. The Raman scattered signal field, on the $a \leftrightarrow c$ transition, is collected and then filtered by a Fabry-Perot interferometer with free spectral range of 75 MHz. The interferometer is tuned to the $a \leftrightarrow c$ transition and has transmission efficiency of 70%, after which it is directed to a single-photon detector (D1). In the absence of a photoelectric detection event registered by D1, the write pulse is followed by an orthogonally polarized clean pulse of duration 200 ns, which transfers the atomic population back from $|a\rangle$ to $|b\rangle$. The sequence is repeated at a frequency of 1 MHz. A detection event at D1 heralds the excitation of an atomic spin wave with the desired wave vector, and the write or signal measurement sequence is stopped.

The prepared spin wave is stored in the sample and left undisturbed. A horizontally polarized read laser pulse (identical to the clean pulse), counterpropagating with the write pulse, induces Raman scattering, converting the stored spin-wave excitation into an idler field emitted on the $c \leftrightarrow b$ transition. In order to reduce background in the idler channel, the idler field is filtered by a Fabry-Perot interferometer with free spectral range of 250 MHz. The interferometer is tuned to the $b \leftrightarrow c$ transition and has transmission efficiency of 70%. The idlers are then collected by a fiber coupler and directed into photodetector (D2). The probability of detecting photoelectric events at D2 determines the measured retrieval efficiency.

Within each hyperfine level, there exist $2F + 1$ Zeeman sublevels. In the absence

of a magnetic field, these energy sublevels are degenerate, though in a weak magnetic field, the levels experience a shift proportional to their magnetic quantum number m_F, as shown in Fig. 18. Also illustrated is the write process in such a sample. If the atoms are unpolarized, the write process generates several atomic coherences that precess with different Larmor frequencies. The interference between atomic coherences results in the fast oscillations of retrieval efficiency shown in Fig. 19. Slower decay on the 200 μs time scale is due to ballistic expansion of the atomic sample during the write/read delay.

3.4 Lattice-confined atomic gas

To increase the coherence time of the spin wave, atomic motion needs to be confined and the magnetically insensitive atomic coherence needs to be utilized. We achieve these goals by loading of the atoms into a 1-D optical lattice and optical pumping of the atoms into the m = 0 Zeeman sublevel of the F = 2 hyperfine level. We also choose polarizations of write/read and signal/idler fields to utilize the long-lived hyperfine coherence between the F=2 m=0 and F=1 m=0 states.

3.4.1 Experimental setup

The main elements of our experiment are shown in Fig. 20. A sample of ^{87}Rb atoms is collected and cooled in a magneto-optical trap for 0.2 to 0.5 s. Next, the trap laser is detuned to 90 MHz below atomic resonance and the repump laser intensity is lowered, for 20 ms, in order to optimize sub-Doppler cooling and lattice loading. The quadrupole coils of the MOT are switched off, and the bias field of $0.2 - 2$ Gauss, directed along the z-axis, is switched on (the ambient magnetic field compensated by three pairs of Helmholtz coils). MOT trapping and repumping beams are switched off by mechanical shutters.

The optical lattice is made by interfering two beams of light at 1.06 μm, with power varying between 3.5 and 7 W per beam, and intersecting at an angle $\theta \approx 2.5°$. The

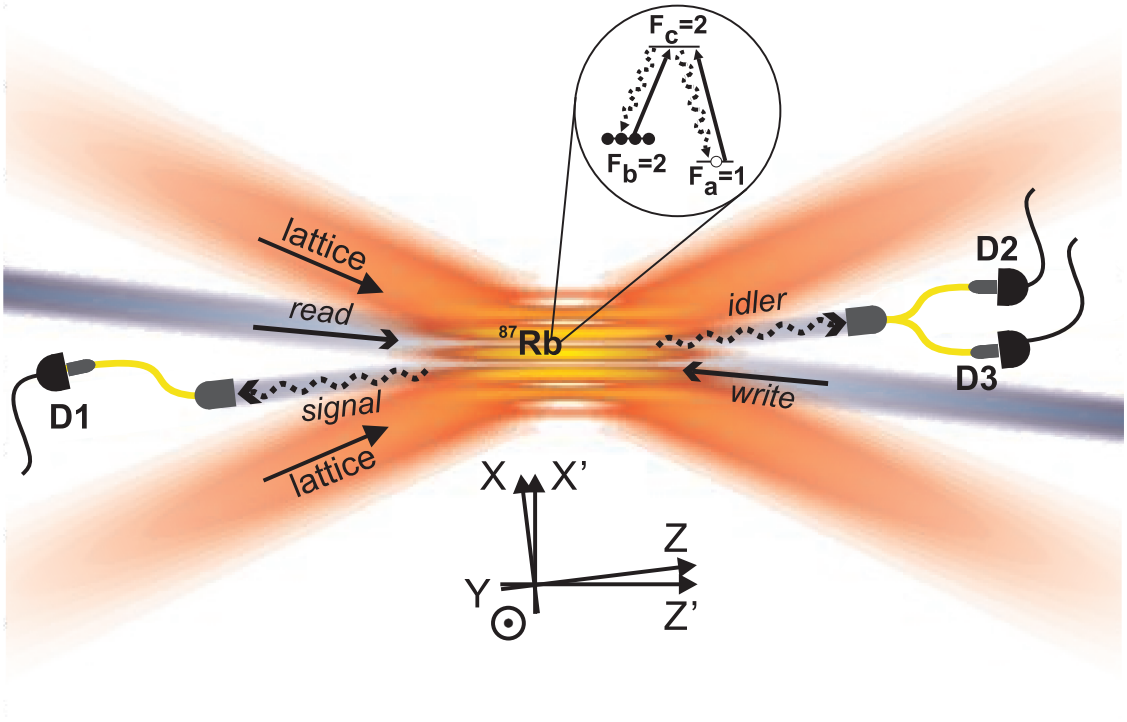

Figure 20: Essential elements of the experimental set-up. Between 10^5 and 10^6 sub-Doppler cooled ^{87}Rb atoms are loaded into an optical lattice, and detection of the signal field, generated by Raman scattering of the write laser pulse (red-detuned by 20 MHz), heralds the presence of a *write* spin wave excitation. A resonant *read*/control field converts the surviving atomic excitation into an idler field after a storage period, T_s. The inset shows the atomic level scheme of ^{87}Rb with levels a and b, the hyperfine components of the ground $5S_{1/2}$ level, and level c, a hyperfine component of the excited $5P_{1/2}$ level. The *write* laser excites the $b \leftrightarrow c$ transition, with Raman emission of the signal field on the $c \rightarrow a$ transition. The *read* laser excites the $a \leftrightarrow c$ transition, with Raman emission of the idler field on the $c \rightarrow b$ transition.

waists of the two beams are ~ 130 and ~ 260 μm, respectively. The maximum lattice depth U_0 is varied between ~ 40 (3.5 W per beam) and ~ 80 (7 W per beam) μK. For the latter case, the corresponding (maximum) trap frequencies are $\approx 2.5 \cdot 10^3$, 110 and 2 Hz along the x'-, y-, and z'-axis, respectively. We employ optical pumping with light propagating along the x-axis and linearly polarized along the z-axis, resonant to the $b \leftrightarrow c$ transition. A repump laser resonant on the $a \leftrightarrow c$ transitions, assists in the transfer of the atoms into the upper clock state $|+\rangle$.

The atoms in the FORT are pumped into the $F_a = 1$ hyperfine level. After a 50 ms delay to allow untrapped atoms to fall away from the FORT, the trapped atoms are pumped into the $F_b = 2$, m=0 state by illuminating the sample with the optical pumping beam for 4 μs and the MOT repumping beam for 10 μs.

The heart of the experimental protocol is performed when the MOT trapping and repumping beams are shut off completely. The *write/read* sequency is similar to that described in Section 3.3, with the following exceptions: (a) a 4 μs optical pumping pulse is executed every 40 experimental trials to avoid substantial depolarization of the atomic sample by the *write* pulses; (b) the *idler* field is collected into one port of a fiber-based beamsplitter followed by photodetectors D2 and D3, where the probability of detecting a photoelectric events and D2(3) is $p_2(3)$. p_2+p_3 determines the measured retrieval efficiency.

In addition, when the sequence is halted after detection of a *signal* photon, the *write*, clean/*read*, and optical pumping fields are further attenuated from their "off" states by no less than 40 dB, 80 dB, and 80 dB, respectively, using additional AOMs. The zeroth-orders of these AOMs are also blocked by mechanical shutters. At these levels of field attenuation, the atomic excitation rate in the sample is a fraction of 1 Hz. This is crucial when quantum memory coherence times approach several milliseconds.

The length of the experimental sequence is 36 ms, determined by optimizing the balance between retrieval efficiency and *idler* detection rate.

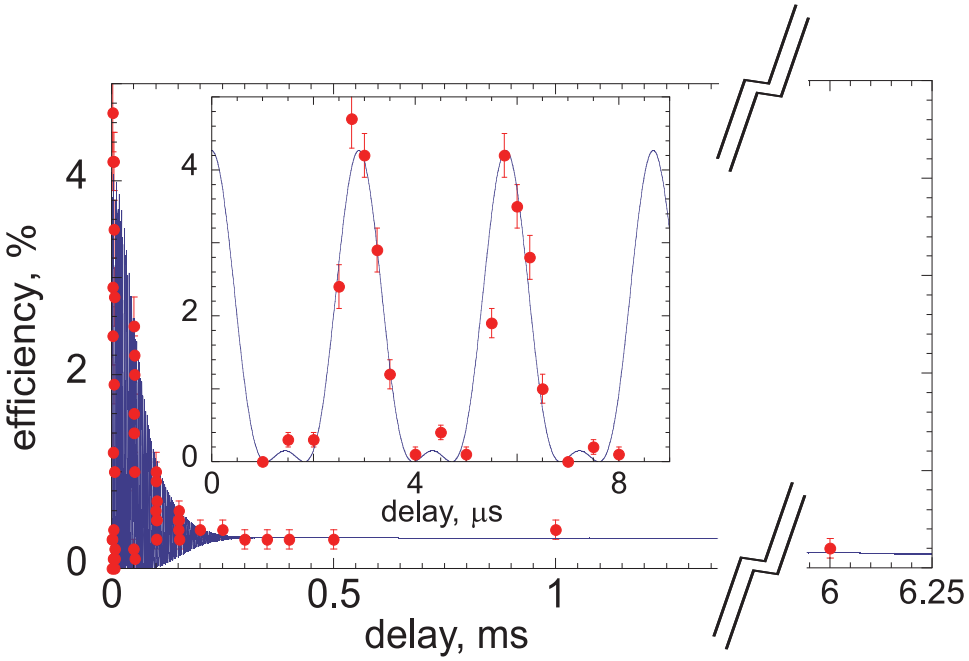

Figure 21: Retrieval efficiency as a function of storage time: unpolarized atoms in an optical lattice. Experimental data, circles, show rapid damped oscillations due to Larmor precession at short times, followed by slow decay on the millisecond timescale associated with the clock transition dephasing. The inset shows details of the short-time damped oscillations. The solid curves are fits based on the theory. The observed 350 kHz oscillation frequency corresponds to $B_0 \approx 0.25$ G.

3.4.2 Unpolarized, lattice-confined atomic gas

To study the different mechanisms of decoherence, we start with the unpolarized sample loaded in the optical lattice. In Fig. 21, we show the retrieval efficiency as a function of storage time. We observe fast oscillations in the first two hundred microseconds followed by a slow decay on the time scale of several milliseconds.

The oscillations are caused by Larmor precession of magnetic hyperfine coherences of the *write* spin wave. A superposition of the states $|b, \pm m\rangle$ and $|a, \pm m'\rangle$ (hereafter referred to as $m \leftrightarrow m'$-coherence) precesses at a frequency

$$\omega_{m,m'} = (\mu_B B_0/\hbar)[g_a\,(m' + m) - \delta g m],$$

where B_0 is the magnetic field, and the Landé factors can be calculated by [51]

$$g_F = g_J \frac{F(F+1) - I(I+1) + J(J+1)}{2F(F+1)} + g_I \frac{F(F+1) + I(I+1) - J(J+1)}{2F(F+1)}. \quad (17)$$

For ^{87}Rb atoms, $g_a \approx -0.5018$, $g_b \approx 0.4998$, and $\delta g \equiv g_a + g_b = -0.002$.

We note that since $\omega_{1,-1} \propto \delta g$, it is about 500 times smaller than $\omega_{1,1} \approx \omega_{2,0}$. The inset to Fig. 21 shows that the fast oscillations, associated with the $2 \leftrightarrow 0$ and $1 \leftrightarrow 1$ coherences, have a period of 2.8 μs corresponding to $B_0 \approx 0.25$ G. The expected 1.4 ms period oscillation of the slow $1 \leftrightarrow -1$ magnetic coherence, which has a small transition weight for this configuration is not visible for this field. We have, however, observed this modulation by increasing the magnetic field to 2 G.

The $0 \leftrightarrow 0$ coherence of the clock transition survives the decay of the magnetic coherences up to a storage time of 6 ms (with a small contribution from the $1 \leftrightarrow -1$ coherence). The solid lines are fits to the data using the theory discussed in Ref.[38], where the frequencies and decay times are treated as adjustable parameters. The ratio of maximum efficiency at short times to the efficiency at times longer than 200 μs is predicted, in the absence of atomic motion, to be $(32/13)^2 \approx 6.1$, whereas the observed value is approximately 13. As we discuss further below, the effects of atomic motion result in an additional dephasing of the spin wave which may account for this observation. The asymptotic retrieval efficiency is clearly limited by the initial population $p_0 = 1/5$ of the clock state $|+\rangle$ in the unpolarized sample.

3.4.3 Optical pumping into m=0 state

To circumvent the limit set by the influence of residual magnetic fields and further increase the efficiency at long times, one can use the ground state hyperfine coherence of the m = 0 Zeeman levels as the basis of quantum storage. Ideally, the atomic ensemble can be prepared in the clock state by optical pumping.

We employ optical pumping with light propagating along the x-axis and linearly polarized along the z-axis, resonant to the $b \leftrightarrow c$ transition. A repump beam resonant

on the $a \leftrightarrow c$ transition assists in the transfer of the atoms into the upper clock state, $|+\rangle$ (Fig. 22). A bias magnetic field along the z-axis defines the quantization axis.

The optical pumping beam has a beam waist of 1 mm, slightly larger than the sample size. The beam is retro-reflected after the chamber to avoid momentum transfer to the atoms and minimize atomic loss. Three independent parameters can be adjusted to optimize the efficiency of optical pumping: power, detuning of the light, and number of trials per optical pumping pulse.

The time evolution of the retrieval efficiency is sensitive to the distribution of atoms among the Zeeman sublevels. This dependence can be used to optimize the optical pumping. The retrieval efficiency in a partially polarized sample placed in the magnetic field is given in [38] as

$$\eta_i(T_s) = \eta_0 \Bigg| p_0 e^{-\frac{T_s^2}{4\tau^2}} + \frac{p_1}{12} e^{-\frac{T_s^2}{2\tau_{1,-1}^2}} \cos(\omega_{1,-1} T_s) + \frac{5p_1}{4} e^{-\frac{T_s^2}{2\tau_{1,1}^2}} \cos(\omega_{1,1} T_s) + \frac{p_2}{3} e^{-\frac{T_s^2}{2\tau_{2,0}^2}} \cos(\omega_{2,0} T_s) \Bigg|^2, \tag{18}$$

where η_0 is the retrieval efficiency of an optically pumped sample at storage time $T_s = 0$, $p_{0,1,2}$ corresponds to populations of $|b,0\rangle$, $|b,\pm1\rangle$, $|b,\pm2\rangle$ sublevels respectively, and the numerical coefficients depend on $3j$-symbols. Here, we assume that both $m = 1$ and $m = -1$ sublevels and $m = 2$ and $m = -2$ sublevels have equal populations. Furthermore, $\tau_{1,\pm1}$ and $\tau_{2,\pm0}$ are decay times associated with the magnetic hyperfine coherences $|b,1\rangle \leftrightarrow |a,\pm1\rangle$, and $|b,2\rangle \leftrightarrow |a,0\rangle$. These are due to the linear Zeeman effect and are given by $\tau_{m,m'} = \hbar/(|g_a m' - g_b m|\mu_B \Delta B)$, where $\Delta B = B'l + \delta B$ and δB is a phenomenological width due to fast temporal variations of the magnetic field.

In Fig. 23(a), we show short-time dynamics for the optically pumped sample in a magnetic field of $B = 0.43$ G and, as expected, observe much lower visibility oscillations than those in Fig. 21. The data suggests the clock state $|+\rangle$ population $p_0 \approx 0.85$ and $p_{\pm1} \approx 0.07$, assuming that $p_{\pm2} \approx 0$.

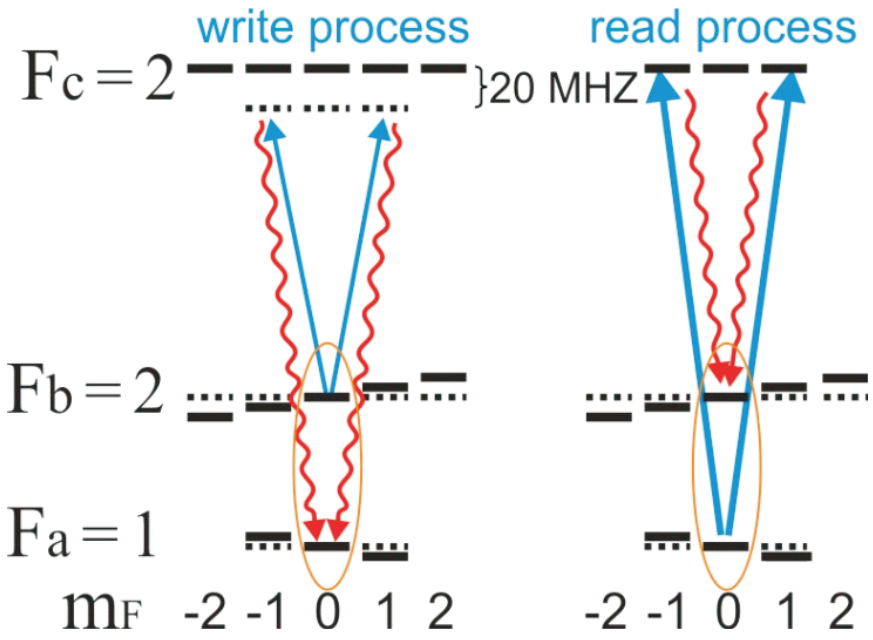

Figure 22: The structure of the atomic levels of the ^{87}Rb atom and the relevant optical transitions in the write/read process for the clock coherence.

We improved optical pumping results by using an optical pumping beam with an elliptical cross-section, which covers the dipole trap more effectively (Fig. 23(b)). This data, measured with a magnetic field of $B = 0.7$ G, suggests the clock state $|+\rangle$ population $p_0 \approx 0.90$ and $p_{\pm 1} \approx 0.05$, assuming that $p_{\pm 2} \approx 0$.

The latest measurement of optical pumping (Fig. 23(c)) suggests that we successfully achieved a completely optically pumped atomic sample with clock state population $p_0 = 1.00 \pm 0.05$.

3.4.4 Single focused beam dipole trap

Another decoherence mechanism of spin wave dephasing is the motion of atoms across the atomic sample. To measure the decoherence time associated with atomic motion, we confine atoms in a single focused beam optical dipole trap, where atoms can freely move along the x' direction. To achieve this with the same optical set up, we send all the power from our 1.06 μm laser into a single trapping beam, and measure the decay of the retrieval efficiency as a function of storage time using the same procedure as

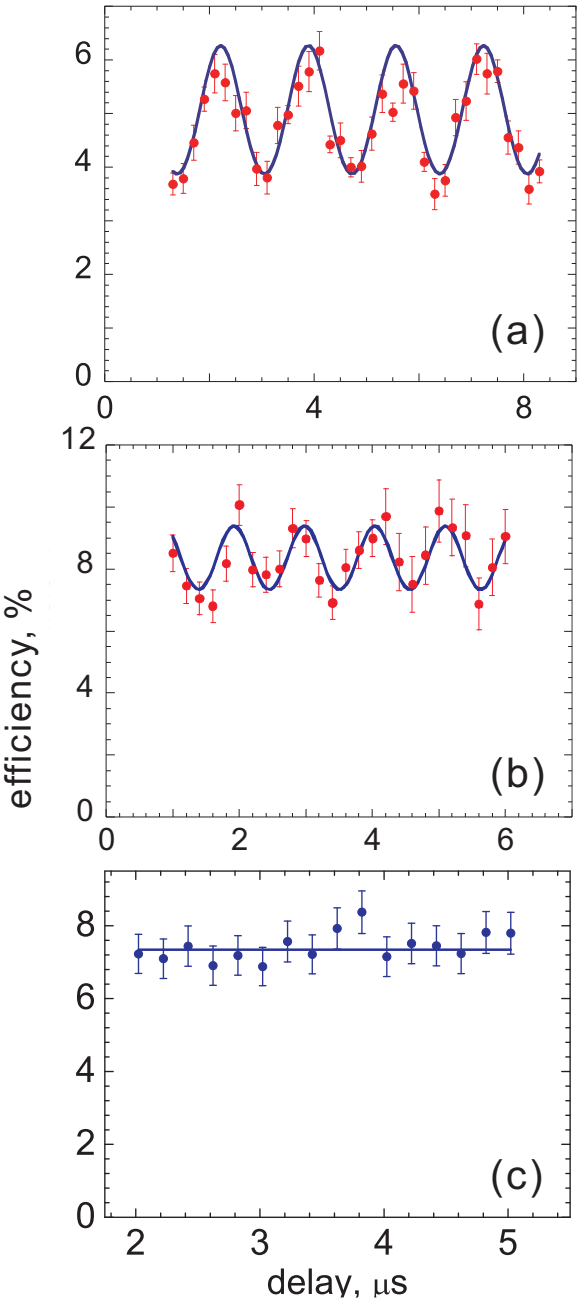

Figure 23: Retrieval efficiency as a function of storage time on a microsecond time scale for optically pumped atoms in an optical lattice. Short time oscillations are due to imperfect optical pumping. Solid lines show the fit to experimental data using the model described in the text.

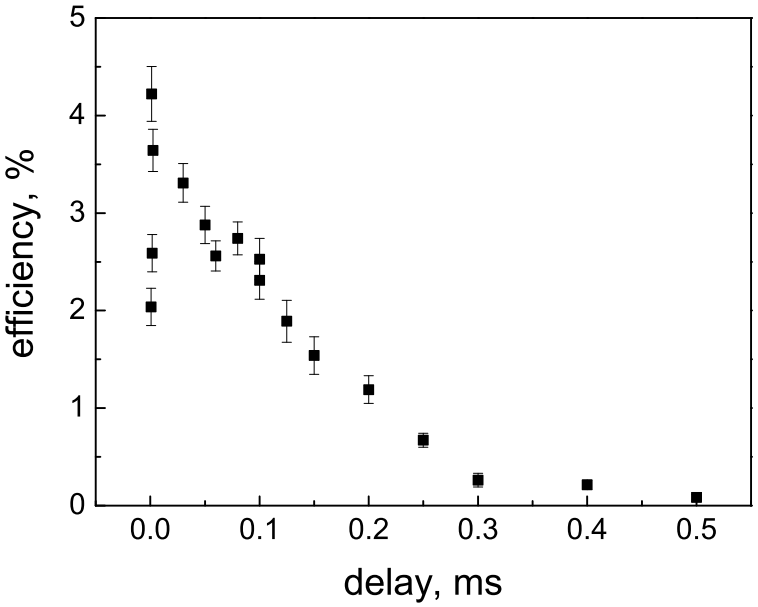

Figure 24: Retrieval efficiency as a function of storage time for a single beam optical dipole trap. Data taken at trap depth $U_0 = 40$ μK.

before.

For a average atomic velocity of 6 cm/s, we expect a coherence time of about $\tau =$ 130 μs. Fig. 24 shows the measured retrieval efficiency in this case. The measured coherence time is $\sim$150 μs, consistent with our theoretical predictions.

3.4.5 Misaligned trap

To optimize coherence time and retrieval efficiencies of the quantum memory based on atoms confined in the optical lattice, the vector $\mathbf{k_w} - \mathbf{k_s}$ should be perpendicular to the lattice pancake planes. To be more specific, *write*, *signal*, and the two lattice beams must be aligned in the same plane. Also, the intersection angle of the *write* beam and one of the lattice beams must be equal that of the *signal* beam and the other lattice beam.

We observed oscillating retrieval efficiency behavior when the lattice beams and experimental beams are slightly misaligned along the y-axis and the *write* beam is

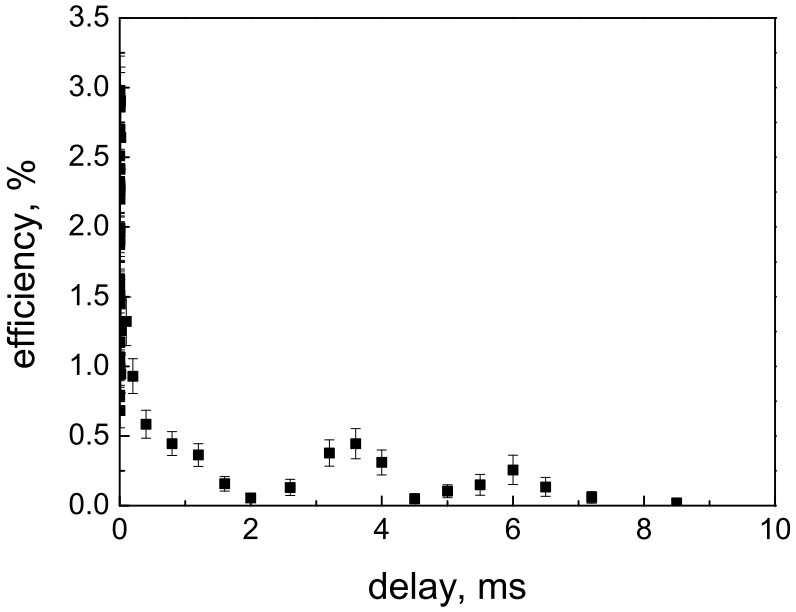

Figure 25: Retrieval efficiency as a function of storage time. *write* and *read* beams are misaligned with respect to the atomic sample confined in the optical lattice. Data taken at $U_0 = 80$ μK.

addressing the atoms on the edge of the dipole trap. As shown in Fig. 25, on a millisecond time scale, the measured retrieval efficiency osillates at a period of $\sim$3 ms. Because, atoms oscillate in the trap with a frequency of hundreds of Hertz along the y-axis, the retrieval efficiency has the same oscillatory behavior.

3.4.6 Polarized, lattice-confined atomic gas

In the situation where the atomic sample is polarized and confined in a lattice much higher retrieval efficiencies at long storage times are observed. We note, however, that optical pumping results in a reduction of overall atomic number by a factor of 2 to 3, which must be accounted for when comparing the relative efficiencies.

Millisecond scale oscillations discussed in the previous subsection disappear in a well-aligned setup. In Fig. 26, two sets of data are shown, corresponding to maximum trap depths $U_0 = 40$ μK and $U_0 = 80$ μK, respectively, with a longer coherence time in

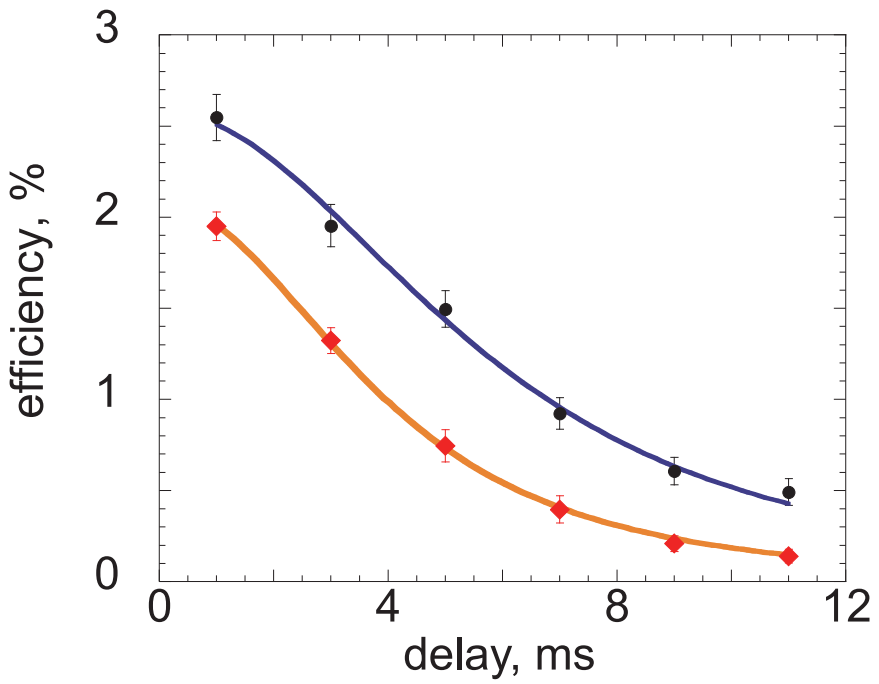

Figure 26: Retrieval efficiency as a function of storage time on a millisecond scale: optically pumped atoms in an optical lattice. Diamonds correspond to a trap depth of $U_0 = 80$ μK, circles correspond to $U_0 = 40$ μK. The solid lines are fits of the form $(1 + (t/T_c)^2)^{-3/2}$, with $T_c = 7.2 \pm 0.25$ ms (blue) and $T_c = 5.0 \pm 0.1$ ms (red).

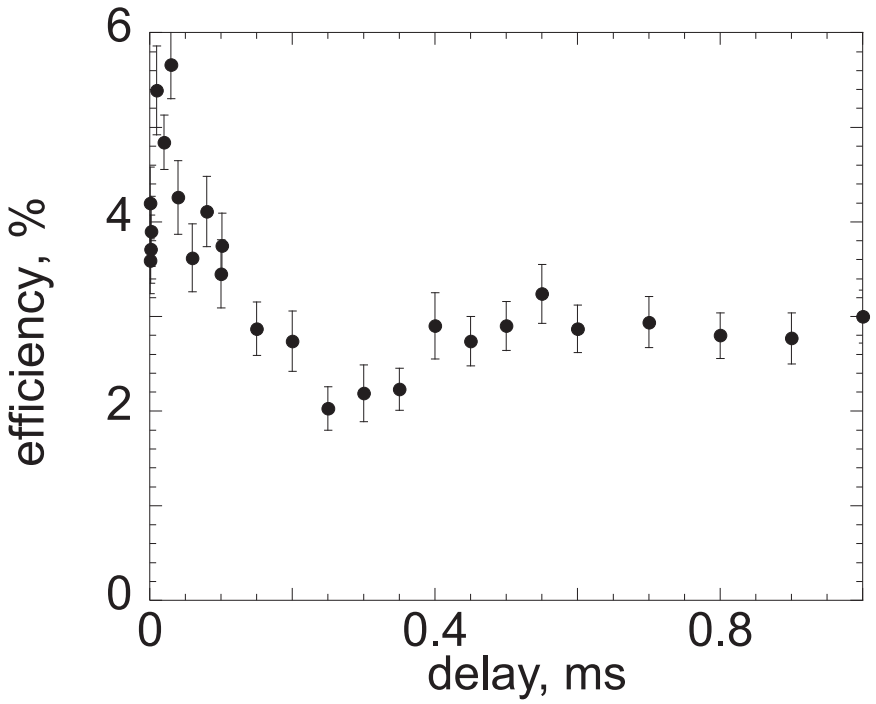

Figure 27: Retrieval efficiency as a function of storage time between 0 and 1 ms for optically pumped atoms in an optical lattice. As described in the text, the initial decrease of retrival efficiency and damped oscillations are due to dephasing of a spin wave associated with motion of atoms confined in optical lattice sites. Data taken at $U_0 = 60$ μK.

the former case. All magnetic coherences are strongly suppressed by optical pumping, and, on the timescale shown, the fast magnetic coherences are completely dissipated, leaving primarily the clock hyperfine coherence.

Atoms in the $|+\rangle$ and $|-\rangle$ clock states experience different, spatially varying light shifts in the lattice. The observed millisecond-scale decoherence of the clock spin wave may be attributed to the atomic motion in the lattice potential, accompanied by the phase broadening resulting from the differential light shifts [52]. Assuming a single harmonic trap, a formula for the decay of the clock transition coherence of the form $(1+(t/T_c)^2)^{-3/2}$ was derived [52]. Our lattice, instead, has a distribution of trap depths and the atoms do not necessarily perform simple harmonic motion. Within each well of the lattice, atoms are expected to be thermally distributed. However, they are not necessarily thermalized with respect to the global potential.

Nevertheless, our data fits the formula well, and from this we extract the decay times $T_c \simeq (7, 5)$ ms for $U_0 \simeq (40, 80)$ μK, respectively. According to the model of Ref.[52], the decay time T_c corresponds to the (homogeneous lattice) equilibrium temperature $T = 2\hbar/(\xi k_B T_c)$, where ξ is the ratio of the ground-state hyperfine splitting to the effective detuning of the lattice light - here $\xi = 6.8 \cdot 10^{-5}$ - resulting in values of $(30, 42)$ μK.

The temperature of the cloud, which is strongly confined in the $x' - y$ plane, was measured by ballistic expansion at an angle of 30° to the horizontal, and found to be $(8, 17)$ μK for $U_0 \simeq (40, 80)$ μK, respectively (See Chapter II). As might be expected, these differ significantly from the homogeneous lattice model discussed above. There are a number of additional mechanisms, such as misalignment of the lattice with respect to the spin wave, quadratic Zeeman (clock) shift, collisional broadening, laser pointing instability, and spontaneous scattering of the lattice light, that we believe produce much smaller decoherence than differential light shifts.

Shown in Fig. 27, optical pumping enables us to observe motional dephasing on

the scale of a few hundred microseconds, followed by a damped evolution towards the 1 ms timescale with the efficiency dropping by about 50% (this typical behavior is also to be expected in the data of Fig. 27, but is not shown here). In common with Fig. 21, we attribute this fast dephasing to atomic oscillations along the lattice axis x'. A simple one dimensional model of harmonic motion yields the characteristic behavior shown in Fig. 27 if one averages over a distribution of oscillator frequencies corresponding to a distribution of trap depths. We have also observed this qualitative behavior in $3+1$ dimensional Monte-Carlo simulations, which include the full atomic orbits.

To assess the effects of an inhomogeneous magnetic field on the retrieval efficiency, we assume a magnetic field $\mathbf{B} = B_0\hat{z} + B'(z\hat{z} - \rho\hat{\rho}/2)$ and a Gaussian cloud density distribution of the form $f(z) = \exp\left(-z^2/2l^2\right)/\sqrt{2\pi l^2}$. We find

$$\eta_i(T_s) = \left| \int dz f(z) e^{-i\Delta\omega_0(z)T_s} \right|^2 = e^{-T_s^2/\tau^2},$$

where $1/\tau = 4\pi \cdot 575$ [Hz/G^2] $B_0 B' l$ follows from the quadratic Zeeman shift $\Delta\omega_0(z)$ of the clock transition. Under the conditions of our experiment $B_0 = 0.5$ G, $B' \ll 100$ mG/cm, we find $\tau \gg 100$ ms, which is much larger than the achieved quantum memory lifetime.

3.4.7 Measurement of quantum statistics of the signal/idler fields

All the measured retrieval efficiencies shown in the figures in this chapter are taken for the signal photodetection probability at detector D1, $p_1 \approx 5 - 7 \cdot 10^{-4}$, while for the data in Table 1 and Table 2, $p_1 \approx 1.6 - 4 \cdot 10^{-4}$.

The retrieval efficiencies discussed in this chapter are *measured* efficiencies, referring to photoelectric detection probabilities per *read* pulse. The uncertainties given are based on the statistics of photoelectron counting events. The measured passive losses from the atomic sample to the detector in the idler channel produce an efficiency factor of $0.25 \pm 10\%$. *Intrinsic* efficiencies are, therefore, greater than the

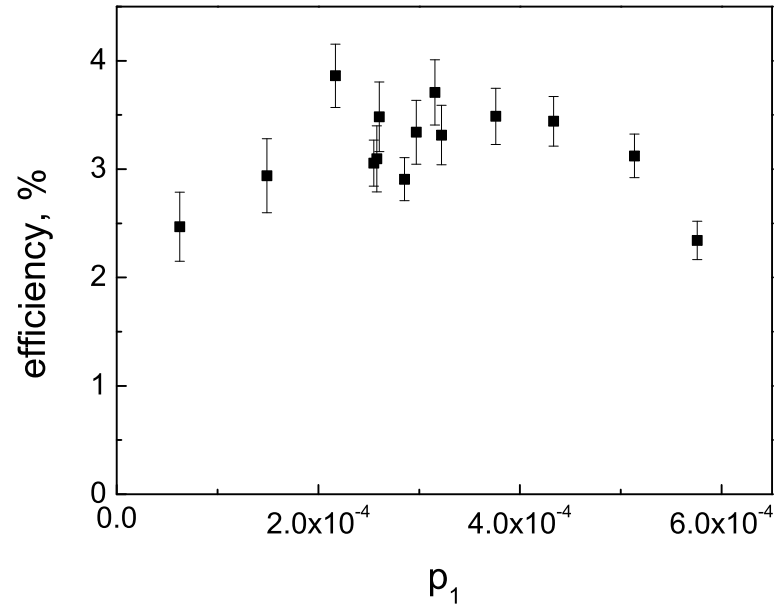

Figure 28: Measured retrieval efficiency as a function of p_1. Data taken at $U_0 = 60$ μK.

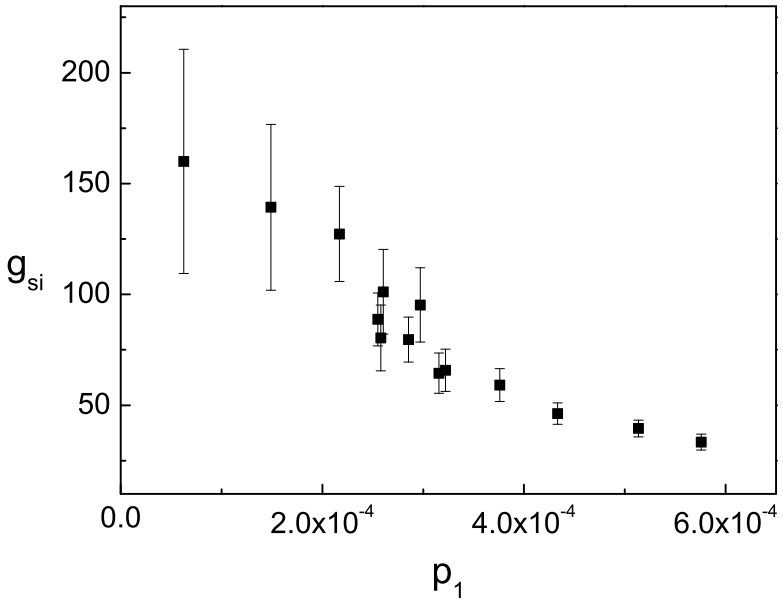

Figure 29: Normalized intensity cross correlation functions, g_{si}, as a function of p_1. Data taken at $U_0 = 60$ μK.

measured retrieval efficiencies by a factor of 4.

Fig. 28 shows one measurement set of the retrieval efficiencies as a function of *signal* photon detection probabilities p_1. We also evaluate the normalized intensity cross-correlation function

$$g_{si} \equiv (p_{12} + p_{13})/[p_1(p_2 + p_3)]$$

as a function of the *signal* photon detection probabilities p_1 (Fig. 29).

As p_1 increases, the correlation function g_{si} decreases, however, the *idler* retrieval efficiency stays the same. The typical background in the *signal* channel is less than $1 \cdot 10^{-5}$, which is much smaller than the detection probability. The typical background in the *idler* channel is $\sim 1 \cdot 10^{-4}$, much smaller than the retrieved idler efficiencies ($\geq 1\%$).

We have verified that all the measured idler efficiencies are independent of p_1, so that they have negligible background contributions up to times longer than 7 ms.

3.5 Quantum nature of the memory

Having measured high retrieval efficiencies, we now demonstrate the quantum nature of the memory on the 5 ms timescale. Specifically, we characterize how well the retrieved idler field compares to a single photon state by measuring the α-parameter of Grangier et al. [53]. The value $\alpha = 0$ corresponds to an ideal, heralded single-photon state, whereas for classical fields $\alpha \geq 1$.

A field in a single-photon state, incident on a beamsplitter, is either transmitted or reflected, and the joint photoelectric detection probability vanishes (Fig. 30). We determine α with the following protocol: We perform a sequence of trials, each trial begining with a *write* pulse and terminating with a clean pulse which resets the atomic state, until the signal detector, D1, registers a photoelectric detection event. At this point, the sequence is halted, and the prepared spin wave is stored for the time,

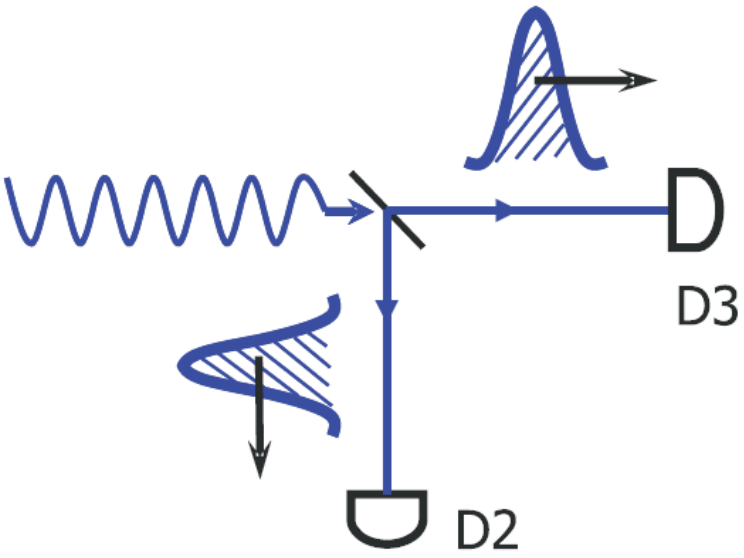

Figure 30: A single photon incident on a beamsplitter takes one of two paths leading to anti-correlated photoelectron counting events at D2 and D3.

T_s, after which time a *read* pulse converts the excitation into an idler field, which is directed onto a beamsplitter followed by photodetectors D2 and D3.

The anticorrelation parameter, α, is given by the ratio of various one-, two- and three-fold photoelectric detection probabilities measured by the set of detectors D1,D2, and D3 [53]:

$$\alpha = \frac{p_1 p_{123}}{p_{12} p_{13}}.$$

It is important to appreciate that α is weakly dependent on the retrieval efficiency until the idler field background becomes significant [18], and for this reason we do not expect α to significantly increase with storage time under the conditions of our experiment. Accounting for the measured signal field detection probability and efficiency and the idler channel background contribution, we theoretically estimate $\alpha \approx 0.02$ for 1.2 μs delay and $\alpha \sim 0.05 - 0.1$ for longer delays.

In Table 1, we give the measured values of α, demonstrating quantum memory for storage times up to 6 ms. We have verified that detection of classical light with

Table 1: Measured values of α, measured efficiency η, and intrinsic efficiency η_{int}, for different storage times.

T, ms	α	η	η_{int}
0.0012	0.02 ± 0.01	6.3%	25%
1	0.12 ± 0.04	2.8%	11%
4	0.17 ± 0.07	1.3%	5%
6	0.10 ± 0.10	1.1%	4.5%

our protocol gives $\alpha = 0.97 \pm 0.08$, consistent with unity. Also shown in Table 1 are the corresponding values of the measured and intrinsic retrieval efficiencies obtained from the same data runs as the α-parameter.

We note that the short time measured (6.3%) and intrinsic (25%) retrieval efficiencies are smaller than our previous values of 7.5% and 34%, respectively [20], due to the difficulty of spatially matching the lattice-loaded atomic sample and the signal-idler modes.

3.6 Deterministic single photon source

An important, immediate application of this long-lived quantum memory is the realization of a deterministic single photon source based on quantum measurement and feedback, as proposed in Ref. [20]. There, the source was implemented using a freely expanding atomic cloud, with a quantum memory time of 32 μs, and two-photon events were reduced to 40% of the coherent state value [20]. As the protocol's success is based on long memory times, we are now able to significantly improve the quality of the single-photon source.

The quality of a deterministic single photon source is demonstrated by measuring sub-Poissonian photoelectron statistics of the second-order coherence function $0 \leq g_D^{(2)}(0) < 1$. The second-order coherence function

$$g_D^{(2)}(0) = p_{23}/(p_2 p_3)$$

quantifies the quality of single photons produced by the following quantum feedback protocol: each trial begins with a *write* pulse. If D1 registers a signal photoelectric event, the protocol is halted. The memory is now armed with a spin wave excitation and is left undisturbed until time t_p when a *read* pulse converts it into the idler field. If D1 does not register an event, the atomic memory is reset to its initial state with a cleaning pulse, and the trial is repeated. The duration of a single trial is 1 μs. If D1 does not register a signal detection event by $t_p - 49$ μs, the protocol is halted and any background counts in the idler channel are detected and included in the measurement record. The procedure closely resembles that used to measure retrieval efficiencies and α, with the following important distinction: instead of waiting for a period T_s after the signal detection event, we decide to read out the idler at time t_p. Hence, we begin the quantum feedback protocol at time $t_p - T_s$.

The source efficiency, defined as the probability ϵ to detect a photoelectric event per trial, is the second important figure of merit. It is given by

$$\epsilon = (p_2 + p_3)/p_1$$

Ideally, $g_D^{(2)}(0) = 0$ and $\epsilon = 1$. The measured values of $g_D^{(2)}(0)$ and ϵ are given in Table 2. We have verified that for classical light our experimental protocol resulted in $g_D^{(2)}(0) = 0.99 \pm 0.05$. The results of the measured second-order coherence function $g_D^{(2)}(0)$ are comparable to those recently achieved using a single trapped atom in a high finesse cavity, while our measured efficiencies are about a factor of two greater [42].

Table 2: Measured values of second order coherence function $g_D^{(2)}(0)$, measured deterministic single photon source efficiency ϵ, and intrinsic source efficiency ϵ_{int}, for different values of read out delay, t_p.

t_p, ms	$g_D^{(2)}(0)$	ϵ	ϵ_{int}
4	0.06 ± 0.04	1.9%	8%
5	0 ± 0.06	1.6%	6%

CHAPTER IV

IN-SITU DETERMINATION OF ZEEMAN CONTENT OF COLLECTIVE ATOMIC MEMORIES

4.1 Introduction

Precise control and accurate measurement of atomic states have become necessities in most experiments. In precise spectroscopic measurements, state preparation is directly linked to the measurement accuracy. In quantum computing, it limits the performance of quantum gates. For atomic ensemble based quantum memories state initialization determines the storage efficiencies and coherence times.

In the past qubits were typically encoded without preparation and diagnostics of population distributions across Zeeman sublevels. Qubit states were represented by distinct pairs of ensembles [15, 54], distinct spin waves within a single sample [16, 17, 55, 56, 57, 46, 45, 58, 59], or isotopic mixtures [21]. As a result, the memory lifetimes were limited to tens of microseconds. In contrast, long-lived quantum memories implemented by our group in the past two years [38, 60] require precise control of atomic Zeeman populations in optically dense atomic samples, as one must encode spin-wave ground-state coherences that are both magnetically- and lattice-insensitive. Once ground state polarization becomes important, special care must be taken to prepare and diagnose Zeeman state distribution.

The DLCZ protocol [33] for the generation of single quantum collective states is intensive in the amount of light involved, while the light fields are typically spatially inhomogeneous. This leads to a variation of both the Zeeman distribution across

atomic samples and of atomic participation in the memory.

In order to extract a meaningful and unambiguous Zeeman distribution, a technique to measure populations in-situ contemporaneously with the spin-wave generation and storage is required. In this chapter, we propose and demonstrate such an in-situ method for high-precision measurement of Zeeman populations of spinwave memories that addresses these problems and could be easily implemented on any setup with only minimal changes. There are two classes of hyperfine spin waves, with fast and slow dephasing rates in an inhomogeneous magnetic field, $1/\tau_{fast}$ and $1/\tau_{slow}$ [38, 60]. Our technique exploits the fact that, for $T_s \ll \tau_{fast}$, the dynamics depend sensitively on the atomic state at the instant the spin waves are written.

4.2 Dynamics of population distribution

To illustrate the importance of in-situ determination of Zeeman content, Fig. 31(a) shows the dynamics of the population as a function of the number of *write-read* trials. Evidently, a few hundred *write/read* trials are sufficient to noticeably alter the distribution, whereas typically $10^2 - 10^4$ trials are required to generate a high-quality spin-wave excitation.

In Fig.1(b), the fast dynamics of η_{VH} are shown to illustrate the sensitive dependence of the read-out efficiency on the population p_0. When an H-polarized *signal* photon is detected, spin waves $\hat{w}_{0,V}$ and $\hat{w}_{1,V}$ are imprinted on the ensemble. At $T_s = 0$ and $\omega_{0,2}T_s = 2\pi$, only atoms originating in the $m = 0$ state contribute to η_{VH}. This can be traced to destructive interference between the V-polarized fast and slow spin waves originating from the $m = \pm 1$ states. At intermediate times, the fast spin wave rotation modulates the interference and the read-out contributions of the $w_{1,V}$ and $w_{0,V}$ are determined by the populations of the $m = \pm 1$ and $m = 0$ states.

In a spatially or temporally varying magnetic field, the Larmor frequency varies across the sample causing each spatially averaged Zeeman coherence to dephase at

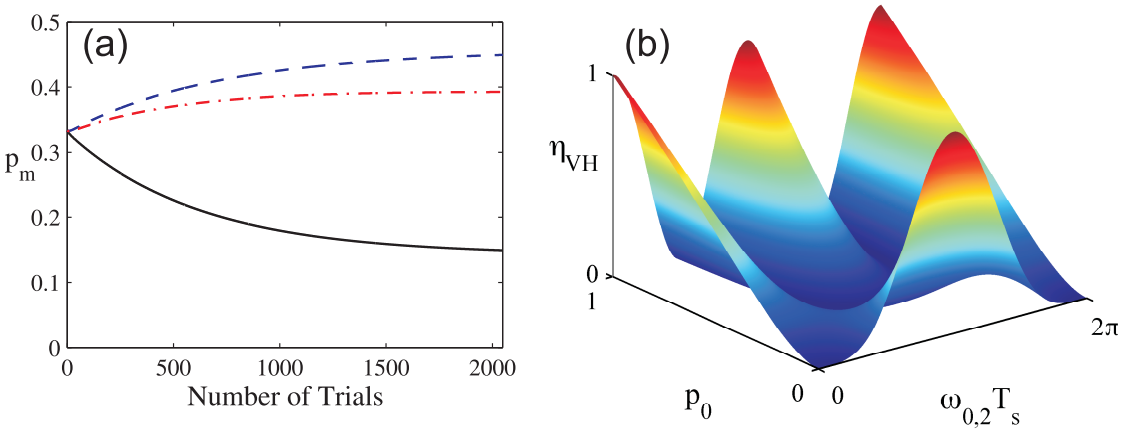

Figure 31: (a) The populations of the Zeeman states $|b,0\rangle$ (solid line), $|b,1\rangle$ (dashed line) and $|b,-1\rangle$ as a function of the number of *write/read* trials in a 1.0 G bias magnetic field. *Write/read* durations, intensities, etc. are taken to be the same as in the experiment (see text). (b) The efficiency, $\eta_{Vi|Hs}(T_s)$, with which an H-polarized *idler* photon is retrieved from the ensemble given the detection of a V-polarized *signal* for storage times, T_s, much less than the fast spin waves' decoherence time. This conditional efficiency is calculated over one oscillation period of the fast spin waves ($0 \leq \omega_{0,2}T_s/(2\pi) \leq 1$) for the range of populations $0 \leq p_0 \leq 1$.

a rate $\Gamma_{m_b,m_a} = |\omega_{m_b,m_a}\Delta B/B_0|$ proportional to the respective Larmor frequency, leading to separated fast and slow time scales $\tau_{fast} = 1/\Gamma_{02}$ and $\tau_{slow} = 1/\Gamma_{1,-1}$, making $\tau_{slow} \simeq 500\tau_{fast}$. If $T_s \gg \tau_{fast}$, only the slowly evolving qubit spin waves $\hat{q}_\lambda$ and the clock spin wave $\hat{s}_{0,0}$ can participate in the retrieval process, as discussed in *Section 4.4.3*.

4.3 Experimental Procedure

We consider a collection of $N \gg 1$ ^{87}Rb atoms (Fig. 32). The atoms are prepared in the lowest energy hyperfine ground level $|b\rangle$ with angular momentum $F_b = 1$ (inset of Fig. 32). A magnetic field produced by a pair of coils in a Helmholtz configuration is applied in the z-direction.

We consider the Raman configuration with ground levels $|b\rangle$ and $|a\rangle$ ($F_a = 2$) and excited level $|c\rangle$ with energies $\hbar\omega_b$, $\hbar\omega_a$ and $\hbar\omega_c$ respectively. Level $|c\rangle$ is the $5P_{1/2}$

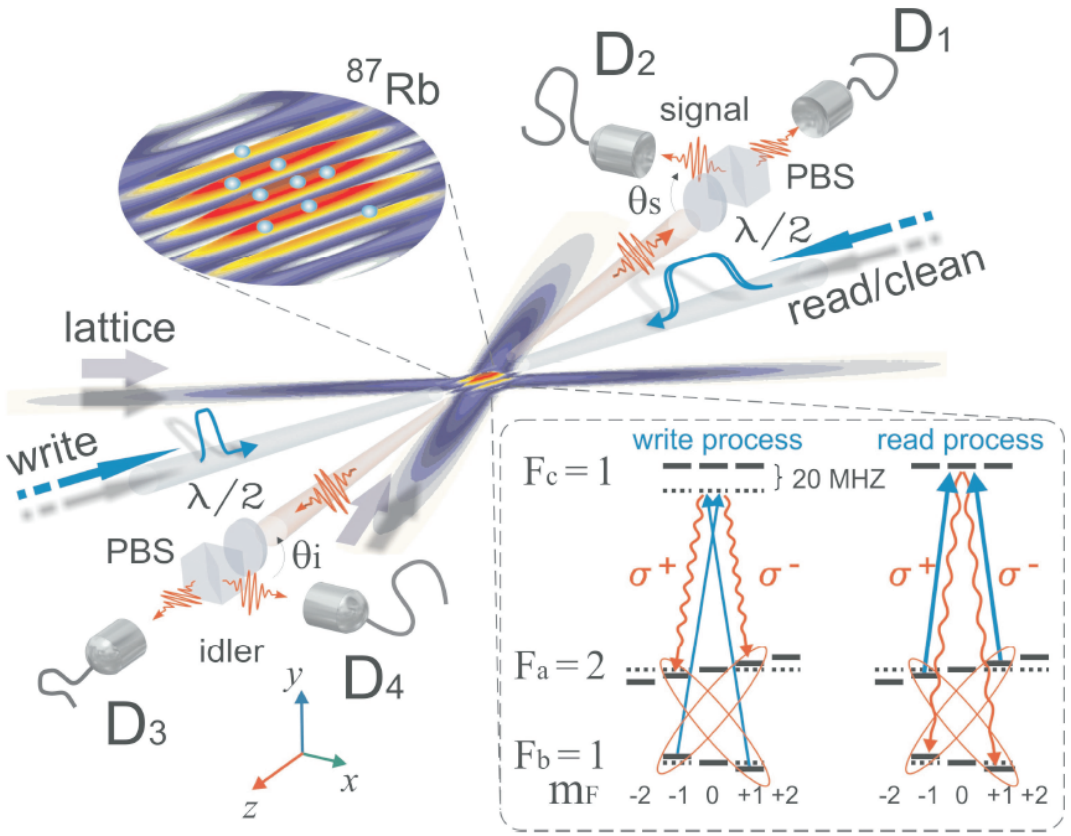

Figure 32: Essential elements of the experimental setup. ^{87}Rb atoms are loaded into a 1-D optical lattice with a 6 μm period, formed by interfering two 1064 nm beams with an angular separation of 10^o; the $(1/e^2)$ beam waists are 90 μm and 120 μm respectively, giving a maximum trap depth of 150 μK. The *write* and *read* fields share a single spatial mode of waist 230 μm, while the *signal* and *idler* mode waists are 110 μm. The *write/read* and *signal/idler* modes intersect at the position of the atomic sample at an angle $\theta_{wi} = 3^o$. PBS is a polarizing beam splitter; D_1-D_4 are detectors. The inset shows the atomic level scheme and *write/read* protocol (see text)

.

hyperfine level with angular momentum $F_c = 1$. A linearly polarized *write* laser pulse with wave vector $\mathbf{k}_w$ and nearly resonant on the D_1 ($|b\rangle \leftrightarrow |c\rangle$) transition is Raman scattered to produce a *signal* field on the $|a\rangle \leftrightarrow |c\rangle$ transition.

The *write* pulse travels at a small angle to the negative z-direction with polarization similarly displaced from the x-direction. A single transverse *signal* mode $u^*(\mathbf{r})$, centered around the wave-vector $\mathbf{k}_s = -k_s\hat{z}$ is collected with horizontal (H) and vertical (V) components in the directions $-\hat{x}$ and $\hat{y}$, respectively. Detection of a *signal* photoelectric event heralds the creation of an atomic spin wave excitation, which is stored for duration T_s. A vertically polarized *read* laser pulse counter-propagating to the *write* pulse retrieves the excitation by generating an *idler* field which is detected in the spatial mode $u(\mathbf{r})$ in the positive z-direction.

Atoms are collected and cooled in a magneto-optical trap for a period of 0.4 s. The trap laser is then detuned by up to 95 MHz below atomic resonance, the quadrupole magnetic field is turned off, and the repump laser intensity is lowered for 40 ms, all in order to optimize the sub-Doppler cooling and loading of the optical lattice. As a result, the lattice contains about 10^7 atoms in the $5S_{1/2}, F = 1$ hyperfine level (level $|b\rangle$), with a magnetic field $B_0 = 1.1$ G applied along the z-direction. The temperature of the cloud was measured to be 20 μK. The lattice parameters (see caption of Fig. 32) result in oscillation frequencies of $1.4 \cdot 10^4$, 400 and 30 Hz. The lattice pancakes coincide with the constant phase planes of atomic spin waves, thereby reducing motional decoherence. The *write/read* process is phase-matched according to the conditions: $\mathbf{k}_w + \mathbf{k}_r = \mathbf{k}_s + \mathbf{k}_i$ ($\mathbf{k}_r = -k_r\hat{k}_w$).

The spin waves are written by a 72 ms long sequence utilizing a measurement-based feedback protocol [20]. This begins with a 50 ns long *write* pulse of power $\simeq 1$ μW, detuned by -20 MHz from the free-space $|b\rangle \leftrightarrow |c\rangle$ transition frequency. If a *signal* photoelectric event is not detected, the *write* pulse is followed by a strong clean pulse to transfer the population back from $|a\rangle$ to $|b\rangle$; the sequence is repeated

at a rate of 0.66 MHz. The clean pulse has duration 200 ns, power 270 μW, and is linearly polarized orthogonal to the *write* field. Detection of a *signal* event by D_1 or D_2 heralds excitation of the desired atomic spin-wave, and halts the *write/clean* sequence. Under our experimental conditions the fast coherence decay time $\tau_{fast} \sim 100$ μs was consistent with milli-Gauss variations in the magnetic field [38].

4.4 Zeeman content distribution

4.4.1 Linear basis, $T_s \ll \tau_{fast}$

For $T_s \ll \tau_{fast}$ with the assumption that $\omega_{0,2} = \omega_{1,1}$ and $\omega_{1,-1} \to 0$, the retrieval efficiencies are given by

$$\eta = \begin{bmatrix} \frac{(1+2p_0)^2 \sin^2(\omega_{0,2}T_s)}{2(p_0+2)(p_0+1)} & \frac{3(1+(1+2p_0)\cos(\omega_{0,2}T_s))^2}{2(5p_0+3)(p_0+2)} \\ \frac{(1-p_0-(1-5p_0)\cos(\omega_{0,2}T_s))^2}{4(p_0+1)^2} & \frac{3(1-5p_0)^2 \sin^2(\omega_{0,2}T_s)}{4(5p_0+3)(p_0+1)} \end{bmatrix},$$

where η is the matrix with elements $\eta_{\lambda\lambda'}$, λ, $\lambda' \in \{H,\ V\}$.

Numerical calculations of the *write/clean* sequence suggest that p_0 falls from its initial value of 1/3 to a steady state value of 0.15 within the first few milliseconds of the 72 ms protocol duration. The alignment symmetry $p_m = p_{-m}$ is broken by the presence of the bias magnetic field, at a level of about 10% under our experimental conditions.

The short-time retrieval efficiencies are shown in Fig. 33, left column. By fitting the matrix η to the four measured efficiencies with a single set of three adjustable parameters (an overall amplitude, $\omega_{0,2}$ and p_0), we obtain $p_0 = 0.183 \pm 0.003$. To account for non-equal detection efficiencies we rotate the *signal* and *idler* polarizations by 90 degrees every 20 min. The total acquisition time is 160 min. A full scan over T_s (2.1 - 3.7 μs) is performed within 48 s to avoid slow systematic drifts.

To confirm the predicted influence of p_0 on the retrieval efficiencies, we optically pump with an additional laser field tuned to the $|b\rangle \leftrightarrow |c\rangle$ transition, propagating in the x-direction and linearly polarized in the z-direction. During optical pumping

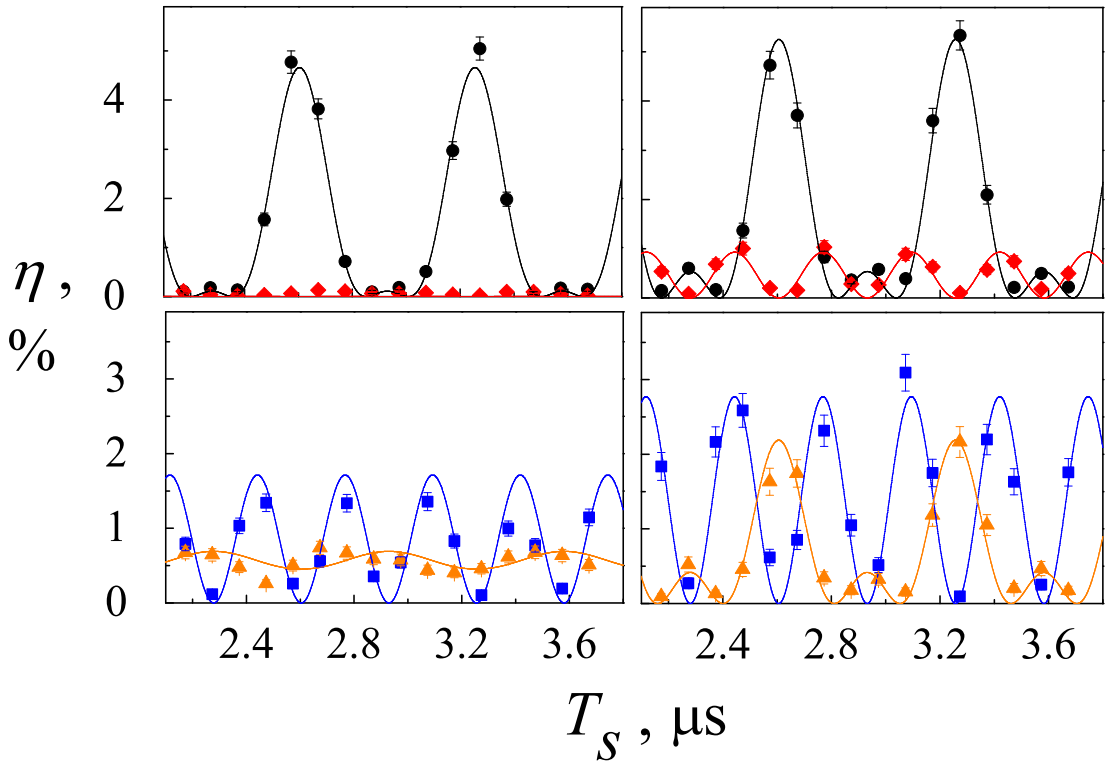

Figure 33: The measured retrieval efficiencies, $\eta_{\lambda\lambda'}$ $(\lambda, \lambda' = H, V)$, for $T_s \ll \tau_{fast}$. Left column: without optical pumping; right column: with optical pumping. Circles, diamonds, squares, and triangles are for HV, VV, HH, and VH *idler-signal* combinations, respectively. Solid curves are theoretical, fit according to the text.

atoms accumulate in the $|b, m = 0\rangle$ state, whereas the *write* sequence reverses this tendency. The optical pumping period, during which a cleaning field empties level a, is 30 μs, followed by 80 *write/clean* cycles before repeating the sequence. The measured efficiencies are shown in the bottom row of Fig. 33. Using the procedure described above, we extract the value $p_0 = 0.47 \pm 0.01$. By varying the optical pumping we have obtained p_0 as high as 0.75 (Fig. 34).

The quoted uncertainty is determined by analysis of distributions of p_0 generated from data sets that are Poisson-distributed around the measured means. A MatLab program generates 10^4 to 10^5 data samples with a Poissonian distribution. Each simulated sample is fit to a set of curves and a set of parameters is calculated, including

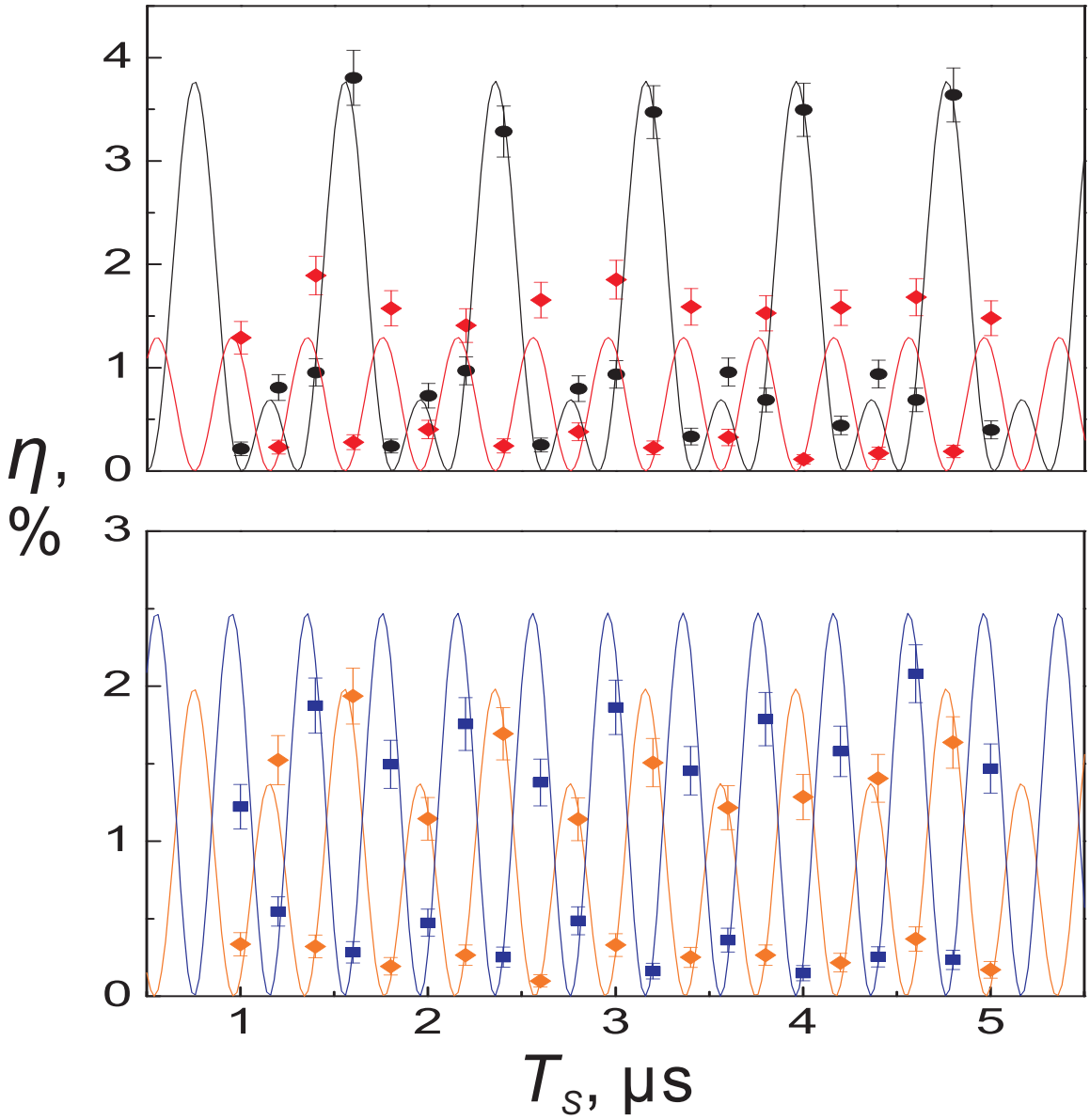

Figure 34: The measured retrieval efficiencies $\eta_{\lambda\lambda'}$, $(\lambda, \lambda' = H, V)$ for $T_s \ll \tau_{fast}$. Circles, diamonds, squares and triangles are for HV, VV, HH, and VH *idler-signal* combinations, respectively. Solid curves are theoretical, fitted according to the text.

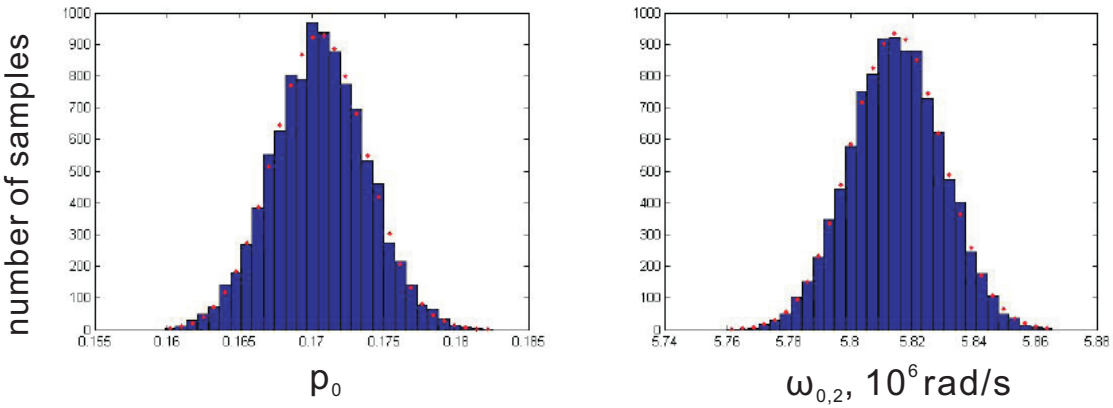

Figure 35: Monte Carlo simulation result of data from non-optical pumping measurements. 10^4 samples were taken in this simulation.

$p_0, \omega_{0,2}$. The whole group of fit parameters is divided into 30 individual regions (Fig. 35). We fit the distribution of parameters with a Gaussian function and thus calculate the uncertainty.

4.4.2 Circular basis, $T_s \ll \tau_{fast}$

The effects of atomic orientation are best observed in the circular basis, as shown in Fig. 36. We perform optical pumping with circularly polarized fields to create non-zero average atomic orientations. By adding quarter-wave plates to the *signal* and *idler* paths, the measurement basis involves circularly polarized quantum states. Allowing for orientation as well as alignment modifies the weights of the Zeeman coherences that appear in Eq. (2) and additionally complicates the expressions for the dark-state polaritons. The curves are obtained by generalization of the theory to include all the relevant coherences [61]. The fits of these to the data are plotted in Fig. 36, resulting in inferred values of the Zeeman level populations.

4.4.3 Linear basis, $\tau_{fast} \ll T_s \ll \tau_{slow}$

We have not employed a completely independent method to verify the correctness of the inferred Zeeman distributions. However, as an additional check we look at the

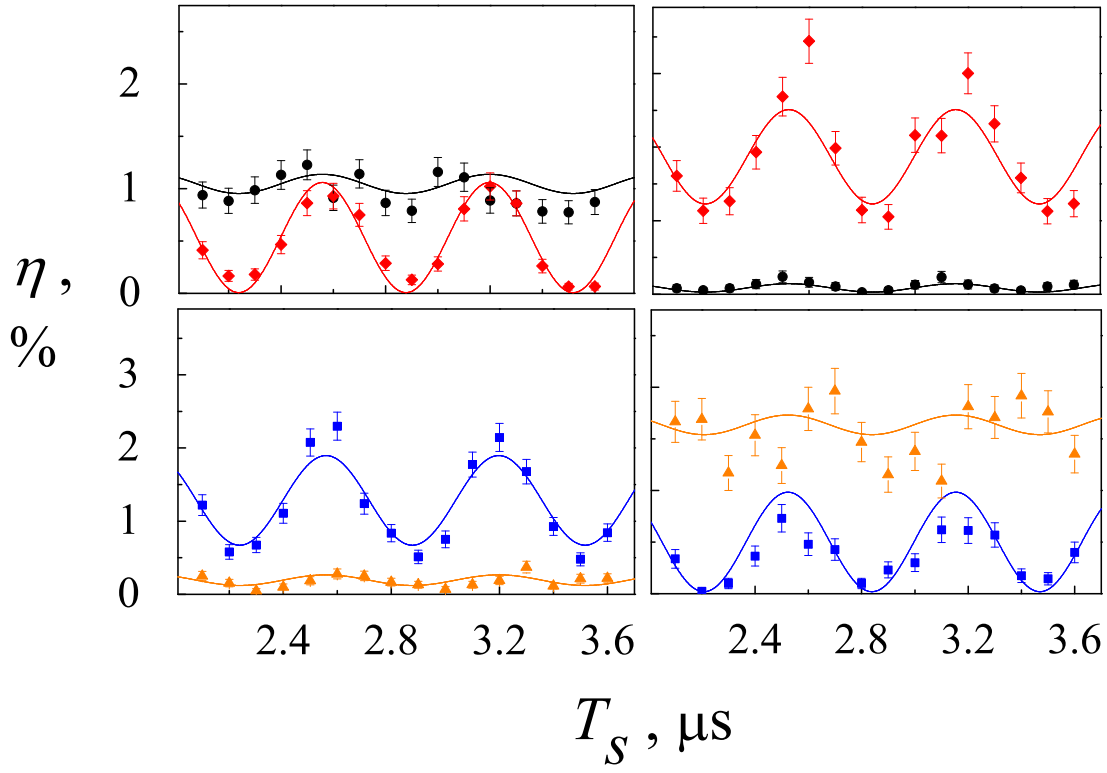

Figure 36: (color online) The measured retrieval efficiencies, $\eta_{\lambda\lambda'}$ $(\lambda, \lambda' = +, -)$, for $T_s \ll \tau_{fast}$. Left column: right-hand polarized optical pumping; right column: left-hand polarized optical pumping. Circles, diamonds, squares, and triangles are for $--$, $+-$, $-+$, and $++$ *idler-signal* combinations, respectively. Solid curves are theoretical, fit according to the text. (left column) $p_1 = 0.68, p_0 = 0.11, p_{-1} = 0.21$; (right column) $p_1 = 0.10, p_0 = 0.08, p_{-1} = 0.82$.

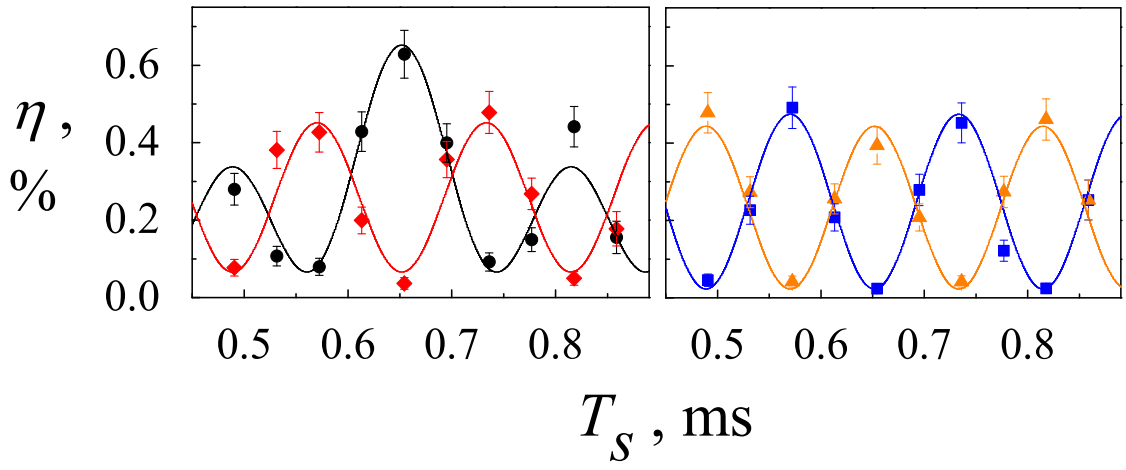

Figure 37: The measured retrieval efficiencies for $\tau_{fast} \ll T_s \ll \tau_{slow}$, labeling as in Fig. 33. Solid curves are theory, each with an additional independent background contribution.

dynamics of the slow hyperfine coherences.

For $\tau_{fast} \ll T_s \ll \tau_{slow}$, the retrieval efficiencies can be written in the general form $\eta_{\lambda\lambda'}(T_s) = |p_0\chi_c\delta_{\lambda H}\delta_{\lambda' V} + p_1\chi_{\lambda\lambda'}(T_s)|^2$, where χ_c is a constant contribution from the clock spin wave and $\chi_{\lambda\lambda'}(T_s)$ is the qubit amplitude. We note that the clock spin wave contributes only to η_{HV}. The probability amplitudes for Raman excitation of the clock transition interfere constructively and destructively for V- and H-polarized *signal* emission, respectively. Explicitly, the retrieval efficiency matrix is

$$\eta = \begin{bmatrix} \frac{(1-p_0)^2\sin^2(\omega_{1,-1}T_s)}{2(p_0+2)(p_0+1)} & \frac{3(p_0+(1-p_0)\cos(\omega_{1,-1}T_s))^2}{2(5p_0+3)(p_0+2)} \\ \frac{(1-p_0)^2\cos^2(\omega_{1,-1}T_s)}{4(1+p_0)^2} & \frac{3(1-p_0)^2\sin^2(\omega_{1,-1}T_s)}{4(5p_0+3)(p_0+1)} \end{bmatrix},$$

We note in a limit of $p_0 = 0$ for storage times $\tau_{fast} \ll T_s \ll \tau_{slow}$, the Larmor spin-wave evolution approximates qubit rotation about a fixed axis. For $p_0 = 0$, there is no clock spin-wave, therefore, pure qubit rotation is read out. Moreover, conditioned on an H-polarized *signal* detection, the *idler* read-out dynamics closely approximate pure qubit rotation for $p_0 \ll 1$ (first column of η).

In Fig. 37, we show efficiencies measured in the millisecond storage time regime

in the absence of optical pumping. By fitting the data with the above theoretical expressions, we extract data $p_0 = 0.16 \pm 0.02$, in agreement with the value inferred from the dynamics of the fast coherences. This value is sufficiently small that η_{VH} and η_{HH} show sinusoidal qubit rotation, whereas η_{VV} and η_{HV} are additionally modulated, as expected. The relative efficiencies at short and long times, shown in Figs. 33, 36, and 37, are consistent with our theory when adjusted at long times by an additional factor of 3/5. This factor is in agreement with our measurements of the effects of atomic motion on the clock spin wave dynamics, cf. Ref.[38].

CHAPTER V

CONTINUOUS QUANTUM MEASUREMENT OF A LIGHT-MATTER SYSTEM

This chapter is based on Ref. [62].

5.1 Introduction

Continuous measurements provide information on the conditional evolution of the state of a quantum system (see e.g, Refs. [63, 64]), but examples of such measurements are rare in literature. It has been observed that photoelectric detection of a field emitted from an optical cavity causes abrupt changes in the state of the intracavity field [65, 66, 67]. The quantum theory of continuous measurements also predicts dissipative conditional evolution during periods in which no detection events are registered.

However, for such a conditioned evolution to take place, the detection apparatus must be of high-efficiency. Otherwise, a lack of detection cannot be interpreted as the absence of a field excitation, and hence one obtains little information about the underlying state. Therefore, observation of the *complete* conditional dynamics is extremely difficult, and there is only one example of such investigation, which was performed on superconducting qubits [68].

The challenge is to continuously monitor, with high efficiency, systems with significant quantum correlations/entanglement for time-scales longer than the temporal resolution of the measurement apparatus. Unfortunately, one cannot meet this challenge with most systems that are currently accessible experimentally. For example,

parametric down conversion has been a very successful paradigm for a variety of investigations involving correlated quantum states, and is a promising workhorse for future quantum information processing systems. It does not, however, readily lend itself to continuous quantum measurement.

To understand this, consider a laser pulse incident on a nonlinear crystal. The nonlinear interaction yields a state for the down-converted fields of the form

$$|\psi\rangle \sim |vac\rangle + \chi \int dt dt' f(t,t') \hat{\psi}_s^\dagger(t) \hat{\psi}_i^\dagger(t') |vac\rangle + O(\chi^2),$$

where the interaction strength $\chi \ll 1$, $\hat{\psi}_s^\dagger(t)$ and $\hat{\psi}_i^\dagger(t')$ are continuous boson operators for the signal and idler fields, respectively, and the two-photon amplitude $f(t,t')$ is, in general, a non-separable function of t and t'.

This non-separability is often referred to as *time-frequency entanglement*. Continuous photodetection of one of the fields, say the signal, would result in a state-reduction of the joint signal-idler quantum state. In turn, this could be monitored by photodetection of the idler. The conditions necessary to observe non-trivial features of the continuous measurement are as follows:

(a) Temporal resolution of the photodetectors much shorter than the characteristic temporal widths associated with f;

(b) The two-photon amplitude should ideally be factorizable $f(t,t') = \varphi_s(t)\varphi_i(t')$ avoiding *time-frequency entanglement* [69, 70];

(c) Sufficiently high *total* detection efficiency.

Although there have been impressive advances in sources of down-conversion, especially improvements in total efficiency, to our knowledge, the three conditions have not been satisfied simultaneously. The principal difficulty comes from the large bandwidth of the down-converted fields, leading to prohibitively short resolution times for the photodetectors. The degree of spectral filtering required for compatibility with available detector resolution would result in unacceptably low total efficiency, which as we note below, makes conditional evolution unobservable.

5.2 Quantum-mechanically correlated atom-light system

A cold atomic ensemble can provide a system analogous to parametric amplification while ensuring that the joint signal-idler amplitude remains separable. In this chapter, we consider an ensemble of $N \gg 1$ atoms in a Λ configuration with ground levels $|b\rangle$ and $|a\rangle$ and excited level $|c\rangle$ and initially prepared in level $|b\rangle$.

A weak *write* pulse nearly resonant on the $|b\rangle \leftrightarrow |c\rangle$ transition impinges on the ensemble. This *write* field induces Raman scattering of signal photons nearly resonant on the $|a\rangle \leftrightarrow |c\rangle$ transition with a temporal envelope identical to that of the *write* pulse [50].

Independently of the time at which a signal photon might be emitted, the Raman scattering imprints an idler excitation onto a unique spatial spin-wave mode [50]. After the *write* process is complete, the state of the idler spin wave can then be mapped to an idler field mode through application of a *read* field resonant on the $|a\rangle \leftrightarrow |c\rangle$ transition. The scattering dynamics are thus equivalent to those of a two-mode parametric amplifier, *i.e.* the signal-idler amplitude remains separable.

Furthermore, by extending the *write* process over a long period (0.8 μs), we are able to ensure that the photodetectors employed have a temporal resolution much shorter than the emitted signal field.

A remaining challenge here is to achieve the required high detection efficiency. By optimizing the *write/read* and signal/idler spatial modes, we obtain a measured signal detection efficiency of 0.17, which may be compared with 0.08 in Ref. [20]. Additionally, in order for the signal-idler amplitude to remain separable, the efficiency with which idler spin wave excitations are read into the detected idler field must not depend on the time at which a signal photon was emitted, *i.e.* the retrieval efficiency must be independent of storage time over the duration of an experimental trial.

To ensure this, one must counteract the ambient magnetic fields which could

induce a deleterious dephasing of the spin waves over the time scales in question. Lifetimes of idler spin waves over millisecond time scales have been demonstrated by employing magnetically insensitive spin-wave coherences and optical pumping into particular Zeeman levels [38, 60]. This technique cannot be used here, however, since it would involve the application of a bias field. This results in oscillations of the retrieval efficiency on μs time scales due to imperfect optical pumping [38].

We therefore obtain sufficiently long memory lifetimes by minimizing the ambient magnetic fields. In addition, careful characterization of the temporal signal wavepacket profile and influence of optical pumping processes on it are performed to exclude other effects distorting the measurement induced dynamics.

5.3 Theory of conditional quantum evolution

We consider a source of correlated signal and idler fields with the assumption that the two-photon amplitude is separable: $f(t,t') = \varphi_s(t)\varphi_i(t')$. The signal field undergoes a continuous photon-counting measurement as it impinges on a single photon detector with efficiency ϵ_s. The probability for no photoelectric event registered on the single photon detector before t_c is [62]

$$\pi_0(t_c) = \frac{1}{1+\epsilon_s\mu(t_c)\sinh^2\chi} + O(\chi^3), \tag{19}$$

where the increasing function $\mu(t_c) \equiv \int_{-\infty}^{t_c} dt\,|\varphi_s(t)|^2$, with $\mu(\infty) = 1$.

Conditioned on the absence of a signal event in the interval $(-\infty, t_c)$, we can calculate the probability of registering at least one photoelectric detection event (PEDE) in the idler channel by taking the Expectation value of the projection operator

$$\hat{P}_i \equiv: 1 - \exp(-\hat{d}_i^\dagger \hat{d}_i) :$$

with respect to the conditioned state, where $\hat{d}_i = \sqrt{\epsilon}_i\hat{a}_i + \sqrt{1-\epsilon}_i\hat{\xi}_i$, ϵ_i is the efficiency of the idler detector, and $\hat{\xi}_i$ is an idler noise operator. The second term of the operator $\hat{P}_i$ projects onto the subspace in which no idler photons are detected.

Similarly, one finds the probability of detecting a signal between times t_1 and t_2, $p_{s|0}(t_1, t_2; t_c)$ corresponds to the expectation value of

$$\hat{P}_s(t_1, t_2) =: 1 - \exp(-\int_{t_1}^{t_2} dt\, \hat{\psi}^\dagger_{D1}(t)\hat{\psi}_{D1}(t)) : .$$

Finally, the joint conditioned probability that a photoelectric event is registered at both the idler detector (at any time during the trial) and the signal detector between times t_1 and t_2 corresponds to the expectation value of $\hat{P}_i\hat{P}_s(t_1, t_2)$.

Dark counts on the signal and idler channels can be modelled by taking the noise fields associated with $\hat{\xi}_s(t)$ and $\hat{\xi}_i$ to be in coherent states; the dark count rates would be given by $B_i = \left\langle \hat{\xi}_i^\dagger \hat{\xi}_i \right\rangle$ and $B_s(t_1, t_2) = \int_{t_1}^{t_2} dt \left\langle \hat{\xi}_s^\dagger(t)\hat{\xi}_s(t) \right\rangle$. In the weak excitation limit, where $B_i \sim B_s(t_1, t_2) \sim \sinh^2\chi \ll 1$, these conditioned detection probabilities are, to first order in $\sinh^2\chi$,

$$p_{s|0}(t_1, t_2; t_c) \approx \epsilon_s\left(\mu(t_2) - \mu(t_1)\right)\sinh^2\chi + B_s(t_1, t_2) \tag{20a}$$

$$p_{i|0}(t_c) \approx \epsilon_i\left(1 - \epsilon_s\mu(t_c)\right)\sinh^2\chi + B_i \tag{20b}$$

$$p_{si|0}(t_1, t_2; t_c) \approx \epsilon_s\epsilon_i\left(\mu(t_2) - \mu(t_1)\right)\sinh^2\chi. \tag{20c}$$

As intuitively expected, the conditioned idler probability $p_{i|0}(t_c)$ becomes progressively smaller as the conditioning interval increases. By contrast, the probabilities $p_{s|0}(t_1, t_2; t_c)$ and $p_{si|0}(t_1, t_2; t_c)$ are proportional to the detection window $\mu(t_2) - \mu(t_1)$, and are identical to the corresponding unconditioned probabilities. The conditioning only manifests itself in $p_{s|0}(t_1, t_2; t_c)$ and $p_{si|0}(t_1, t_2; t_c)$ through the requirement that the detection window occurs after t_c, and $\mu(t_2) - \mu(t_1) \leq 1 - \mu(t_c)$. From Eqs. (20), we can also determine the unconditioned, integrated probabilities $(t_c, t_1 \to -\infty)$, $(t_2 \to \infty)$ [20]:

$$p_s \approx \epsilon_s \sinh^2 \chi + B_s \tag{21a}$$

$$p_i \approx \epsilon_i \sinh^2 \chi + B_i \tag{21b}$$

$$p_{si} \approx \epsilon_s \epsilon_i \sinh^2 \chi, \tag{21c}$$

From these detection probabilities, one can define an experimentally measurable effective signal efficiency

$$\epsilon_s' \equiv p_{si}/p_i = \epsilon_s \left(1 - \frac{B_i}{\epsilon_i \sinh^2 \chi + B_i}\right), \tag{22}$$

which is reduced by background idler counts B_i. Inspection of Eqs. (20) and (22) reveals that this efficiency can also be obtained through the conditioned idler detection probability as

$$\epsilon_s' = -\frac{1}{p_i}\frac{dp_{i|0}(t_c)}{d\mu}. \tag{23}$$

This correspondence between the predictions of conditioned and unconditioned quantum dynamics provides a quantitative measure to experimentally test the dynamics of conditional quantum measurement.

5.4 Experimental setup

To implement such a test, we prepare an optically thick atomic cloud of ^{85}Rb by switching on a magneto-optical trap (MOT) for a period of 14 ms (Fig. 38). The atomic ground levels $\{|a\rangle\,;|b\rangle\}$ correspond to the $5S_{1/2}, F_{a,b} = \{2, 3\}$ hyperfine levels, while the excited level $|c\rangle$ represents the $5P_{1/2}, F_c = 3$ level of the D_1 line at 795 nm.

After switching off the MOT fields, the experimental sequence begins with all of the atoms pumped into level $|b\rangle$ by sequentially switching off first the trapping light, followed 10 μs later by the repumping light. The quadrupole magnetic field of the MOT is extinguished for the 2.5 ms duration of the measurement sequence.

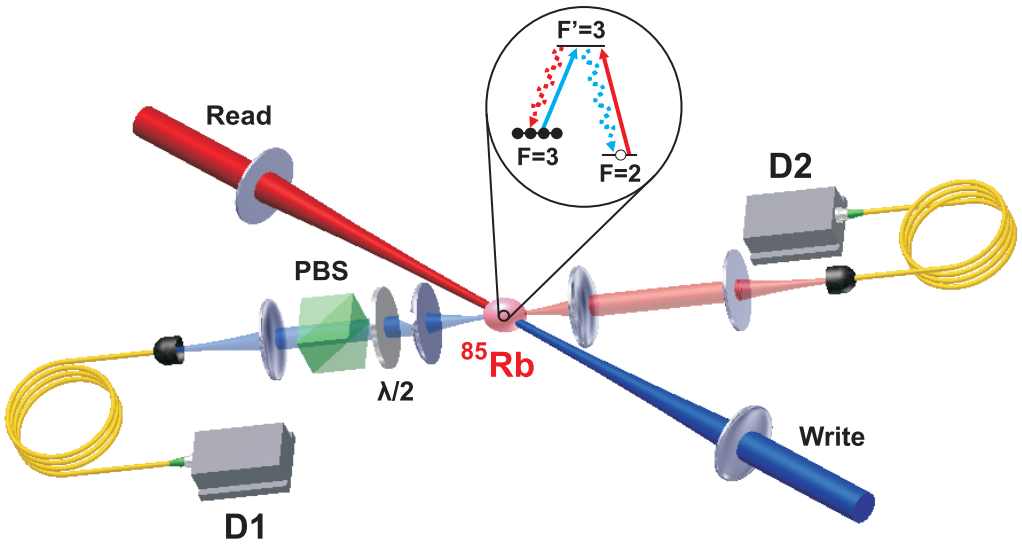

Figure 38: Schematic of experimental setup, with the inset showing the atomic level scheme. Here, $\lambda/2$ and PBS are a half-wave plate and polarizing beam-splitter for the signal field, respectively, and D1 and D2 are single-photon detectors. See text for a discussion.

The whole experimental sequence is sychronized to and triggered by 60Hz AC power line signal to minimize the effect of a time-varing ambient magnetic field across the atomic sample introduced by AC currents. Three pairs of Helmholtz coils are used to compensate the ambient DC magnetic field during the measurement sequence. The measurement sequence consists of 1666 cycles of duration 1.5 μs. The cycle begins when a weak, approximately square, linearly polarized *write* laser pulse, tuned to the $|b\rangle \leftrightarrow |c\rangle$ transition, illuminates the ensemble for $T = 0.8$ μs; that is, in each cycle $\mu(t_c = 0) = 0$ and $\mu(T) = 1$.

The light pulse generates an orthogonally polarized signal field by spontaneous Raman scattering on the $|c\rangle \leftrightarrow |a\rangle$ transition, together with spin wave excitation of the atomic medium associated with the $|b\rangle \leftrightarrow |a\rangle$ hyperfine coherence [33]. After a 200 ns delay, a 200 ns long *read* pulse, tuned to the $|a\rangle \leftrightarrow |c\rangle$ transition, illuminates the atoms. This *read* field, with power 170 μW and linear polarization orthogonal to that of the *write* pulse, converts the atomic spin excitation into an orthogonally

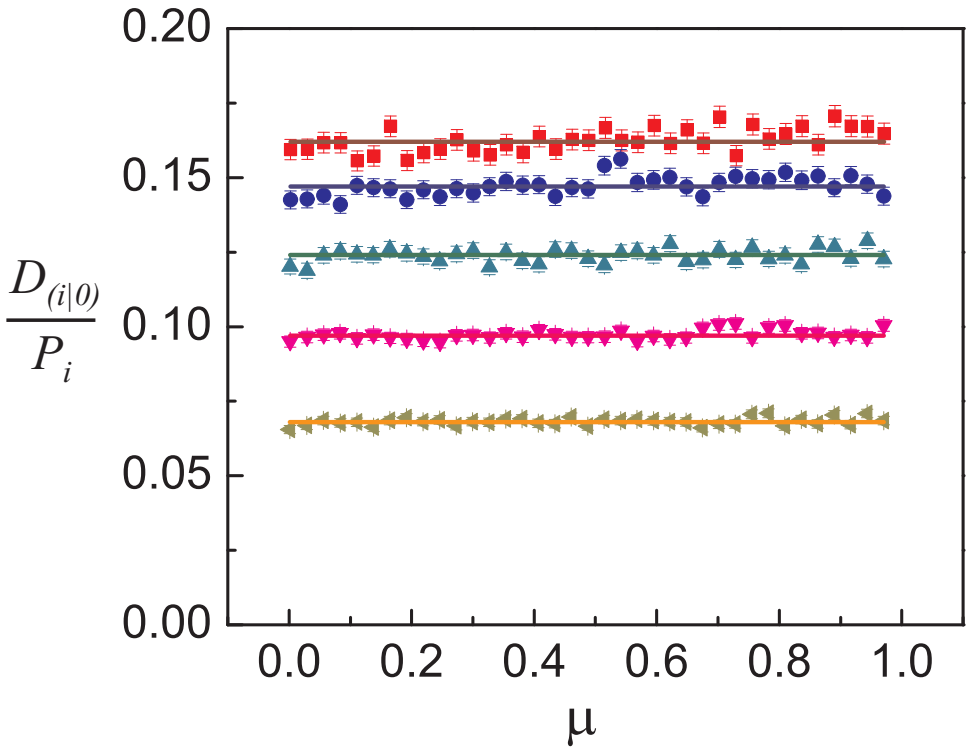

Figure 39: Experimental data for $D_{i|0}(t_c)/P_i$ (discrete data) and P_{si}/P_i (solid lines) vs signal field gate function, $\mu(t_c)$, for five different settings of the half-wave plate (Fig. 38). According to conditional quantum theory, these should be equal, Eqs. (22),(23). Data from top to bottom correspond to decreasing measured signal efficiencies.

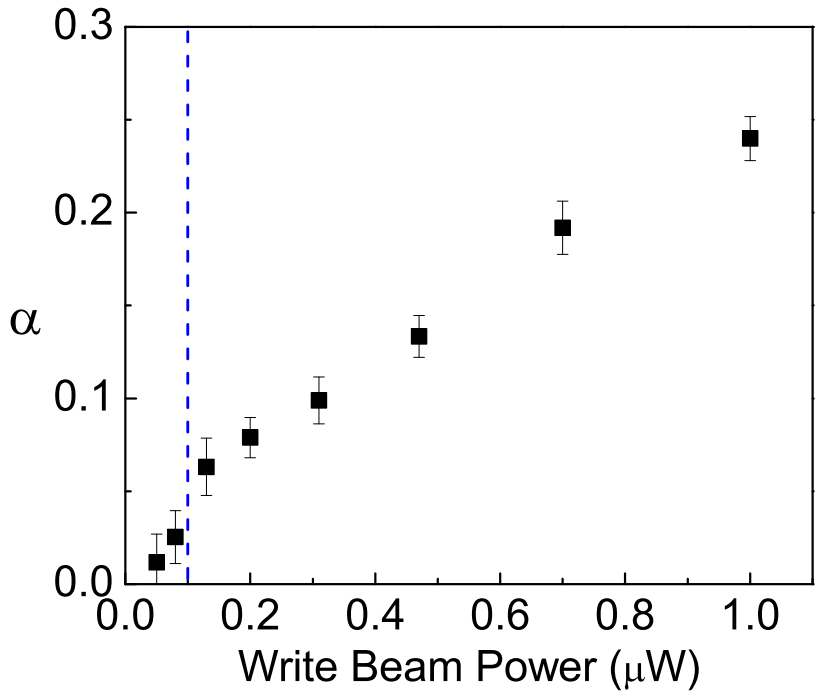

Figure 40: Coefficient α as a function of write beam power (see text). The vertical dashed line shows the value of write beam power at which the data in Fig. 39 were taken.

polarized *idler* field, which is emitted on the $|c\rangle \leftrightarrow |b\rangle$ transition.

Both the *write-read* and *signal-idler* pairs of mode-matched fields are counter-propagating, with Gaussian waists of 400 μm for the former and 130 μm for the latter. The *signal* and *idler* fields are measured by single photon detectors D1 and D2, respectively.

5.5 Observation of quantum evolution

The photoelectric detection events for the signal and idler fields are measured and recorded with a 2 ns time resolution, allowing conditioned and unconditioned detection probabilities to be determined. The unconditioned detection probability for the idler field is defined by the ratio of the number of cycles, N_i, with at least one photoelectric detection event recorded to the total number of cycles: $P_i \equiv N_i/N_T$. The conditioned probability is determined similarly, except that all cycles in which a *signal* photoelectric event has been recorded prior to time t_c are omitted, hence $P_{i|0}(t_c) \equiv N_{i|0}(t_c)/N_T$.

In order to test the predictions of the conditional quantum theory, we measure both the unconditioned signal-idler coincidence probability $P_{si} \equiv N_{si}/N_T$ and the gradient of the conditional idler detection probability $D_{i|0}(t_c) \equiv -dP_{i|0}/d\mu(t_c)$, as a function of $\mu(t_c)$. According to Eq. (23), this must be equal to $\epsilon_s' P_i$. By varying ϵ_s using the half-wave plate placed in the *signal* beam path before the polarizer (Fig. 38), we measure a set of values for P_{si}.

For each plate setting, we construct $D_{i|0}(t_c)$

$$D_{i|0}(t_c) \simeq \frac{P_{i|0}(t_c) - P_{i|0}(t_c + \Delta t)}{\mu(t_c + \Delta t) - \mu(t_c)},$$

where Δt is a sufficiently small time interval that the determined $D_{i|0}(t_c)$ does not depend on its value. The results are presented in Fig. 39 and show very good agreement between the conditional measurement data, $D_{i|0}(t_c)/P_i$, and the unconditional data, P_{si}/P_i, which Eqs. (22) and (23) predict should be equal. The error bars on

conditional data are based on the statistics of the photoelectric counting events, while statistical errors on the unconditioned data are negligible.

At high measured efficiencies there is a small systematic discrepancy in excess of the statistical errors. It requires a careful examination in order to exclude spurious effects which could potentially mimic the predictions of conditional quantum theory. The two most relevant processes are (1) the residual effects of Raman scattering of the *write* pulse, and (2) the Larmor precession of the hyperfine coherences in the uncompensated magnetic field.

Although Raman scattering is responsible for the creation of the signal photon and the accompanying spin excitation, excessive scattering into undetected field modes can slightly deplete the population of level $|b\rangle$ during the *write* process, and therefore reduces the efficiency with which spin waves generated early in the *write* process are retrieved. We can model this effect using the time dependent retrieval efficiency $\eta(1-\mu) = \epsilon_i \exp(-\alpha(1-\mu))$, where $1-\mu$ is proportional to the time a spin wave is exposed to the deleterious effects of the *write* beam.

This would manifest itself in an increasing time dependent correction to ϵ'_s in Eq. (23) and as a reduced joint signal-idler coincidence detection probability at small values of μ. Based on this picture, we can model $p_{si}(\mu, \mu+\Delta\mu)/\Delta\mu \sim p_s \exp(-\alpha(1-\mu))$, where α is proportional to the *write* pulse energy, as shown by the data in Fig. 40. As can be seen from Fig. 40, for the 0.1 μW power at which data in Fig. 39 were taken, these effects are not significant. Similarly, the Larmor precession reduces p_{si} for small values of $\mu(t_c)$, according to $p_{si} \sim \exp(-\gamma(1-\mu)^2)$ [18, 44]. For the measured coherence time $\tau_c \approx 25\,\mu$s and maximum write-read delay $T_t \sim 1\,\mu$s duration of the experimental cycle, the expected decoherence effects $\gamma = (T_t/\tau_c)^2 \approx 0.004$ are negligible.

CHAPTER VI

CONCLUSION

In the thesis I have presented an implementation of a quantum memory with lifetimes up to 7 ms. The memory is realized using cold rubidium atoms confined in a one-dimensional optical lattice, which suppresses motional dephasing on a sub-ms time scale. The magnetically-insensitive clock coherence is employed to remove memory sensitivity (and hence, dephasing) to ambient magnetic fields. The 7 ms value of the memory lifetime is limited by the differential AC Stark shifts due to the optical lattice. The work described set the stage for further advances in memory lifetimes, potentially in excess of many seconds.

Some of these steps have already being taken in our group. In particular, we have achieved compensation of the differential AC Stark shift, using two different approaches. First, we proposed and implemented a two-photon laser compensation scheme [71]. In it, one leg of the transition is driven by the trapping 1064 nm laser field and the other involves a compensating (931 nm) laser field with a spatially uniform profile. The two photon transition is detuned by Δ_2 from the $|5S_{1/2}, F = 1\rangle \rightarrow |6S_{1/2}, F = 1\rangle$. In this scheme the spatially varing light shifts of the clock states can be made identical with a suitable choice of the compensating field frequency and intensity. The compensation condition is approximately $\Omega_c = -4\Delta_2\Delta_{hfs}$, where Ω_c is the compensation field Rabi frequency and Δ_{hfs}= 6.8 GHz the ground state hyperfine splitting of ^{87}Rb. We have observed quantum memory lifetimes in excess 0.1 s using this scheme [71].

Subsequently, we observed differential Stark shift compensation employing the so-called "magic" magnetic field technique [72]. The "magic" field technique utilizes an

energy level shift that is linear in both the bias magnetic field and the intensity of the circularly polarized lattice field. We have observed coherent light storage with lifetimes in excess of 0.3 s when the magnetic field was tuned to the vicinity of 4.2 G [73].

REFERENCES

[1] R. P. Feynman, "Simulating physics with computers," *Int. J. Th. Phys.* **21**, 467 (1981).

[2] R. P. Feynman, "There is plenty of room at the bottom,", accessed 16 June 2010, http://www.zyvex.com/nanotech/feynman.html.

[3] R. Rivest, A. Shamir, and L. Adleman, "A Method for Obtaining Digital Signatures and Public-Key Cryptosystems," *Communications of the ACM* **21(2)**, 120 (1978).

[4] I. Niven, H. S. Zuckerman, and H. L. Montgomery, *An Introduction to the Theory of Numbers*, 5th edition ed. (John Wiley & Sons, Inc., 1991).

[5] C. H. Bennett and G. Brassard, in *Proceedings of the international conference on computers, systems and signal processing* Indian Institute of Science, Bangalore, India 1984.

[6] W. K. Wootters and W. H. Zurek, "A single quantum cannot be cloned," *Phys. Rev. Lett.* **299**, 802 (1982).

[7] A. K. Ekert, "Quantum cryptography based on Bell theorem," *Phys. Rev. Lett.* **67**, 661 (1991).

[8] C. H. Bennett, G. Brassard, C. Crèpeau, R. Jozsa, A. Peres, and W. K. Wootters, "an Unknown Quantum State via Dual Classical and Einstein- Podolsky-Rosen Channels," *Phys. Rev. Lett.* **70**, 1895 (1993).

[9] D. Bouwmeester, J. W. Pan, M. Mattle, K.and Eibl, H. Weinfurter, and A. Zeilinger, "Experimental quantum teleportation," *Nature* **390**, 575 (1997).

[10] D. Boschi, S. Branca, F. D. Martini, L. Hardy, and S. Popescu, "Experimental realization of teleporting an unknown pure quantum state via dual classical and einstein-podolsky-rosen channels," *Phys. Rev. Lett.* **80**, 1121 (1998).

[11] M. Aspelmeyer, H. R. Bohm, T. Gyatso, T. Jennewein, R. Kaltenbaek, M. Lindenthal, G. Molina-Terriza, A. Poppe, K. Resch, M. Taraba, R. Ursin, P. Walther, and A. Zeilinger, "Long-distance free-space distribution of quantum entanglement," *Science* **301**, 621 (2003).

[12] M. Riebe, H. Haffner, C. F. Roos, W. Hansel, J. Benhelm, G. P. T. Lancaster, T. W. Korber, C. Becher, F. Schmidt-Kaler, D. F. V. James, and R. Blatt, "Deterministic quantum teleportation with atoms," *Nature* **429**, 734 (2004).

[13] M. D. Barrett, J. Chiaverini, T. Schaetz, J. Britton, W. M. Itano, J. D. Jost, E. Knill, C. Langer, D. Leibfried, R. Ozeri, and D. J. Wineland, "Deterministic quantum teleportation of atomic qubits," *Nature* **429**, 737 (2004).

[14] S. Olmschenk, D. Hayes, D. N. Matsukevich, P. Maunz, D. L. Moehring, and C. Monroe, "Quantum Logic between Distant Trapped Ions," *Int. J. Quant. Inf.* **8**, 337 (2010).

[15] D. N. Matsukevich and A. Kuzmich, "Quantum state transfer between matter and light," *Science* **306**, 663 (2004).

[16] D. N. Matsukevich, T. Chanelière, M. Bhattacharya, S. Y. Lan, S. D. Jenkins, T. A. B. Kennedy, and A. Kuzmich, "Entanglement of a photon and a collective atomic excitation," *Phys. Rev. Lett.* **95**, 040405 (2005).

[17] D. N. Matsukevich, T. Chanelière, S. D. Jenkins, S. Y. Lan, T. A. B. Kennedy, and A. Kuzmich, "Observation of dark state polariton collapses and revivals," *Phys. Rev. Lett.* **96**, 033601 (2006).

[18] T. Chanelière, D. N. Matsukevich, S. D. Jenkins, S. Y. Lan, T. A. B. Kennedy, and A. Kuzmich, "Storage and retrieval of single photons transmitted between remote quantum memories," *Nature* **438**, 833 (2005).

[19] T. Chanelière, D. N. Matsukevich, S. D. Jenkins, T. A. B. Kennedy, M. S. Chapman, and A. Kuzmich, "Quantum telecommunication based on atomic cascade transitions," *Phys. Rev. Lett.* **96**, 093604 (2006).

[20] D. N. Matsukevich, T. Chanelière, S. D. Jenkins, S.-Y. Lan, T. Kennedy, and A. Kuzmich, "Deterministic single photons via conditional quantum evolution," *Phys. Rev. Lett.* **97**, 013601 (2006).

[21] S.-Y. Lan, S. D. Jenkins, T. Chanelière, D. N. Matsukevich, C. J. Campbell, R. Zhao, T. A. B. Kennedy, and A. Kuzmich, "Dual-Species Matter Qubit Entangled with Light," *Phys. Rev. Lett.* **98**, 123602 (2007).

[22] H.-J. Briegel, W. Dur, J. I. Cirac, and P. Zoller, "Quantum repeaters: The role of imperfect local operations in quantum communication," *Phys. Rev. Lett.* **81**, 5932 (1998).

[23] W. Dur, H.-J. Briegel, J. I. Cirac, and P. Zoller, "Quantum repeaters based on entanglement purification," *Phys. Rev. A* **59**, 169 (1999).

[24] C. H. Bennett, G. Brassard, S. Popescu, B. Schumacher, J. A. Smolin, and W. K. Wootters, "Purification of Noisy Entanglement and Faithful Teleportation via Noisy Channels," *Phys. Rev. Lett.* **76**, 722 (1996).

[25] C. H. Bennett, H. J. Bernstein, S. Popescu, and B. Schumacher, "Concentrating Partial Entanglement by Local Operations," *Phys. Rev. A* **53**, 2046 (1996).

[26] C. H. Bennett, D. P. DiVincenzo, J. A. Smolin, and W. K. Wootters, "Mixed-state entanglement and quantum error correction," *Phys. Rev. A* **54**, 3824 (1996).

[27] O. A. Collins, S. D. Jenkins, A. Kuzmich, and T. A. B. Kennedy, "Multiplexed memory-insensitive quantum repeaters," *Phys. Rev. Lett.* **98**, 060502 (2007).

[28] S.-Y. Lan, A. G. Radnaev, O. A. Collins, D. N. Matsukevich, T. A. B. Kennedy, and A. Kuzmich, "A Multiplexed Quantum Memory," *Optics Express* **17**, 13639 (2009).

[29] C. Liu, Z. Dutton, Behroozi, C. H., and L. V. Hau, "Observation of coherent optical information storage in an atomic medium using halted light pulses," *Nature* **409**, 490 (2001).

[30] D. F. Phillips, A. Fleischhauer, A. Mair, R. L. Walsworth, and M. D. Lukin, "Storage of light in atomic vapor," *Phys. Rev. Lett.* **86**, 783 (2001).

[31] B. Julsgaard, J. Sherson, J. I. Cirac, J. Fiurasek, and E. S. Polzik, "Experimental demonstration of quantum memory for light," *Nature* **432**, 482 (2004).

[32] J. J. Longdell, E. Fraval, M. J. Sellars, and N. B. Manson, "Stopped light with storage times greater than one second using electromagnetically induced transparency in a solid," *Phys. Rev. Lett.* **95**, 063601 (2005).

[33] L.-M. Duan, M. D. Lukin, I. J. Cirac, and P. Zoller, "Long-distance quantum communication with atomic ensembles and linear optics," *Nature* **414**, 413 (2001).

[34] S. Chu, J. Bjorkholm, A. Ashkin, and A. Cable, "Experimental Observation of Optically Trapped Atoms," *Phys. Rev. Lett.* **57**, 314 (1986).

[35] M. Saffman and T. G. Walker, "Analysis of a quantum logic device based on dipole-dipole interactions of optically trapped Rydberg atoms," *Phys. Rev. A* **72**, 022347 (2005).

[36] R. Grimm, M. Weidemuller, and Y. B. Ovchinnikov, "Optical Dipole Traps For Neutral Atoms," *Adv. At. Mol. Opt. Phys.* **42**, 95 (2000).

[37] T. M. Brzozowski, M. Maczynska, M. Zawada, J. Zachorowski, and W. Gawlik, "Time-of-flight measurement of the temperature of cold atoms for short trap-probe beam distances," *J. Opt. B* **4**, 62 (2002).

[38] R. Zhao, Y. O. Dudin, S. D. Jenkins, C. J. Campbell, D. N. Matsukevich, T. A. B. Kennedy, and A. Kuzmich, "Long-lived Quantum Memory," *Nature Physics* **5**, 100 (2009).

[39] L. Jiang, J. M. Taylor, and M. D. Lukin, "Fast and robust approach to long-distance quantum communication with atomic ensembles," *Phys. Rev. A* **76**, 012301 (2007).

[40] N. Sangouard, C. Simon, B. Zhao, Y.-A. Chen, H. de Riedmatten, J.-W. Pan, and N. Gisin, "Robust and efficient quantum repeaters with atomic ensembles and linear optics," *Phys. Rev. A* **77**, 062301 (2008).

[41] L.-M. Duan, "Entangling many atomic ensembles through laser manipulation," *Phys. Rev. Lett.* **88**, 170402 (2002).

[42] M. Hijlkema, B. Weber, H. P. Specht, S. C. Webster, A. Kuhn, and G. Rempe, "A single-photon server with just one atom," *Nature Physics* **3**, 253 (2007).

[43] D. N. Matsukevich, T. Chanelière, S. D. Jenkins, S.-Y. Lan, T. Kennedy, and A. Kuzmich, "Entanglement of remote atomic qubits," *Phys. Rev. Lett.* **96**, 030405 (2006).

[44] S. D. Jenkins, D. N. Matsukevich, T. Chanelière, A. Kuzmich, and T. A. B. Kennedy, "Theory of dark-state polariton collapses and revivals," *Phys. Rev. A* **73**, 021803(R) (2006).

[45] Y.-A. Chen, S. Chen, Z.-S. Yuan, B. Zhao, C.-S. Chuu, J. Schmiedmayer, and J.-W. Pan, "Memory-built-in quantum teleportation with photonic and atomic qubits," *Nature Physics* **4**, 103 (2007).

[46] J. Simon, H. Tanji, S. Ghosh, and V. Vuletic, "Single-photon bus connecting spin-wave quantum memories," *Nature Physics* **3**, 765 (2007).

[47] J. Laurat, K. S. Choi, H. Deng, C. W. Chou, and H. J. Kimble, "Heralded entanglement between atomic ensembles: preparation, decoherence, and scaling," *Phys. Rev. Lett.* **99**, 180504 (2007).

[48] K. Choi, H. Deng, J. Laurat, and H. J. Kimble, "Mapping photonic entanglement into and out of a quantum memory," *Nature* **452**, 67 (2008).

[49] M. Lukin, "Colloquium: Trapping and manipulating photon states in atomic ensembles," *Rev. Mod. Phys.* **75**, 457 (2003).

[50] S. D. Jenkins, "Theory of light-atomic ensemble interactions,", Ph. D. Dissertation, Georgia Institute of Technology, 2006.

[51] D. A. Steck, "Rubidium D Line Data,", accessed 10 May 2010, http://steck.us/alkalidata 2008.

[52] S. Kuhr, W. Alt, D. Schrader, I. Dotsenko, Y. Miroshnychenko, A. Rauschenbeutel, and D. Meschede, "Analysis of dephasing mechanisms in a standing-wave dipole trap," *Phys. Rev. A* **72**, 023406 (2005).

[53] P. Grangier, G. Roger, and A. Aspect, "Experimental evidence for a photon anticorrelation effect on a beam splitter: A new light on single-photon interferences.," *Europhys. Lett.* **1**, 173 (1986).

[54] C. Chou, S. Polyakov, A. Kuzmich, and H. Kimble, "Single-photon generation from stored excitation in an atomic ensemble," *Phys. Rev. Lett.* **92**, 213601 (2004).

[55] R. Inoue, N. Kanai, T. Yonehara, Y. Miyamoto, M. Koashi, and M. Kozuma, "Entanglement of orbital angular momentum states between an ensemble of cold atoms and a photon," *Phys. Rev. A* **74**, 053809 (2006).

[56] H. de Riedmatten, J. Laurat, C. W. Chou, E. W. Schomburg, D. Felinto, and H. J. Kimble, "Direct Measurement of Decoherence for Entanglement between a Photon and Stored Atomic Excitation," *Phys. Rev. Lett.* **97**, 113603 (2006).

[57] S. Chen, Y.-A. Chen, B. Zhao, Z.-S. Yuan, J. Schmiedmayer, and J.-W. Pan, "Demonstration of a Stable Atom-Photon Entanglement Source for Quantum Repeaters," *Phys. Rev. Lett.* **99**, 180505 (2007).

[58] Z.-S. Yuan, Y.-A. Chen, B. Zhao, S. Chen, J. Schmiedmayer, and J.-W. Pan, "Experimental demonstration of a BDCZ quantum repeater node," *Nature* **454**, 1098 (2008).

[59] H. Tanji, S. Ghosh, J. Simon, B. Bloom, and V. Vuletiċ, "Heralded Single-Magnon Quantum Memory for Photon Polarization States," *Phys. Rev. Lett.* **103**, 043601 (2009).

[60] Y. O. Dudin, S. D. Jenkins, R. Zhao, D. N. Matsukevich, A. Kuzmich, and T. A. B. Kennedy, "Entanglement of a Photon and an Optical Lattice Spin Wave," *Phys. Rev. Lett.* **103**, 020505 (2009).

[61] S. D. Jenkins, unpublished.

[62] R. Zhao, S. D. Jenkins, C. J. Campbell, D. N. Matsukevich, T. Chanelière, T. A. B. Kennedy, and A. Kuzmich, "Continuous quantum measurement of a light-matter system," *Phys. Rev. A* **81**, 031802(R) (2010).

[63] H. J. Carmichael, *An Open Systems Approach to Quantum Optics* (Springer, 1999).

[64] C. W. Gardiner and P. Zoller, *Quantum Noise: a Handbook of Markovian and Non-Markovian Quantum Stochastic Methods with Applications to Quantum Optics*, 2nd ed ed. (Springer-Verlag, Berlin, 2000).

[65] G. T. Foster, L. A. Orozco, H. M. Castro-Beltran, and H. J. Carmichael, "Quantum State Reduction and Conditional Time Evolution of Wave-Particle Correlations in Cavity QED," *Phys. Rev. Lett.* **85**, 3149 (2000).

[66] W. P. Smith, J. E. Reiner, L. A. Orozco, S. Kuhr, and H. M. Wiseman, "Capture and Release of a Conditional State of a Cavity QED System by Quantum Feedback," *Phys. Rev. Lett.* **89**, 133601 (2002).

[67] H. Carmichael, G. Foster, L. Orozco, J. Reiner, and P. Rice, in *Intensity-Field Correlations of Non-Classical Light* volume 46 p. 355 2004.

[68] N. Katz, M. Ansmann, R. C. Bialczak, E. Lucero, M. N. R. McDermott, M. Steffen, E. M. Weig, A. N. Cleland, J. M. Martinis, and A. N. Korotkov, "Coherent State Evolution in a Superconducting Qubit from Partial-Collapse Measurement," *Science* **312**, 1498 (2006).

[69] D. Branning, W. P. Grice, R. Erdmann, and I. A. Walmsley, "Engineering the indistinguishability and entanglement of two photons," *Phys. Rev. Lett.* **83**, 955 (1999).

[70] C. K. Law, I. A. Walmsley, and J. H. Eberly, "Continuous frequency entanglement: effective finite hilbert space and entropy control," *Phys. Rev. Lett.* **84**, 5304 (2000).

[71] A. G. Radnaev, Y. O. Dudin, R. Zhao, H. H. Jen, S. D. Jenkins, A. Kuzmich, and T. Kennedy, "A quantum memory with telecom photon conversion," *Nature Physics* , in press (2010).

[72] N. Lundblad, M. Schlosser, and J. V. Porto, "Experimental observation of magic-wavelength behavior of ^{87}Rb atoms in an optical lattice," *Phys. Rev. A* **81**, 031611(R) (2010).

[73] Y. O. Dudin, R. Zhao, T. A. B. Kennedy, and A. Kuzmich, "Light storage in a magnetically dressed optical lattice," *Phys. Rev. A* **81**, 041805(R) (2010).